HARNESSING NONLINEAR DYNAMICS FOR HIGH-SPEED APPLICATIONS IN INFORMATION SCIENCE

A Dissertation
Presented to
The Academic Faculty

By

Michael J. Wishon

In Partial Fulfillment
of the Requirements for the Degree
Doctor of Philosophy in the
School of Electrical and Computer Engineering

Georgia Institute of Technology

August 2018

HARNESSING NONLINEAR DYNAMICS FOR HIGH-SPEED APPLICATIONS IN INFORMATION SCIENCE

Approved by:

Dr. Citrin, Advisor
School of Electrical and Computer Engineering
Georgia Institute of Technology

Dr. Locquet, Co-Advisor
School of Electrical and Computer Engineering
Georgia Institute of Technology

Dr. Hasler
School of Electrical and Computer Engineering
Georgia Institute of Technology

Dr. Butera
School of Electrical and Computer Engineering
Georgia Institute of Technology

Dr. Anderson
School of Electrical and Computer Engineering
Georgia Institute of Technology

Dr. Chapman
School of Physics
Georgia Institute of Technology

Date Approved: July 24, 2018

They misunderestimated me

George W. Bush

To those who love and support me.

ACKNOWLEDGEMENTS

To my advisors, whose patience and wisdom knows no bounds. To my parents, for their support and guidance based in reality and unconditional love. To the love of my life, for giving me reasons other than ego. To God, for giving me many chances.

TABLE OF CONTENTS

LIST OF TABLES

LIST OF FIGURES

SUMMARY

The main objectives in this thesis are to investigate the dynamic transitions on the route to chaos for external cavity lasers, and then to utilize this knowledge for improving, redefining, and optimizing applications in high-speed information science. External-cavity lasers (ECLs), the system utilized in this thesis, are characterized by nonlinear dynamics created by a laser subjected to optical feedback. Further, this system has been studied for nearly 50 years as a testbed for nonlinear dynamical behavior, as well as, many applications. In this thesis, ECLs are studied using comprehensive, state-of-the-art experiments which simultaneously probe all three dynamic system variables (optical intensity, optical phase, and carrier dynamics) in real-time as the system transitions from constant to deterministic chaos which allows for the characterization of different bifurcation mechanisms which occur on the transition to chaos. The applications which are optimized/improved, in this thesis, are neuromorphic computing, random number generation, microwave oscillation generation, and optical imaging/detection. Specifically, new optimal dynamic operating points are identified in which the ECL should be operated for maximum performance, as well as, the characterization of the different regimes to enhance the capabilities of the applications. In other words, faster and more accurate computing, a superior, novel entropy source for random number generation, a simpler, stable, X-band tunable microwave oscillator, and as a detector.

CHAPTER 1
INTRODUCTION

In a world obsessed with instantaneous and secure data transfer there is a broad interest in optical information processing due to its inherent speed. In this thesis, a multi-GHz, nonlinear, dynamical system's transition from steady-state to chaos (route to chaos) is understood for the first time after nearly 50 years by using comprehensive state-of-the-art experiments (Chapter 2). Specifically, the system which is known as an external-cavity laser (ECL) creates sub-nanosecond nonlinear dynamics which allow for incredibly rich environment for high-speed applications. It is well known that these systems display complex nonlinear dynamics and even deterministic chaos. But, what is not fully understood is the bifurcation mechanisms for the routes to chaos. Fully understanding such routes and the nonlinear dynamics behind them allows for the optimization of applications by the designer. Further, utilizing this knowledge about the dynamic transitions, the system is exploited to improve/re-define four applications in high-speed information science. Specifically, the system is utilized to optimize neuromorphic computing (Chapter 3), as a novel entropy source for random number generation (Chapter 4), to stabilize a X-band tunable microwave generator (Chapter 5), and for imaging and detection (Chapter 6).

First, brain inspired, neuromorphic computing is at the forefront of scientific interest due to its ability to find complex nonlinear relationships in data that can be used for separating data types and predicting future outputs. Also, photonic neuromorphic computers are significantly more energy-efficient than their silicon counterparts. One such method based on recurrent neural networks is reservoir computing which utilizes an untrained neural network with sufficient dynamical complexity predicated on the fact that it satisfies two basic properties. We present here a thorough study of the two reservoir properties that must be satisfied for the reservoir to have universal computing power with fading memory. These

are the separability and approximation properties. Separability essentially states that two inputs should lead to two distinct reservoir responses, and approximation is such that the reservoir should not be so sensitive to slight variations in inputs, due to noise, such that a new and unique response is generated. Here we show the extent to which parameters in the physical system affect the properties. We also define a new metric to classify the property of separability. In essence, we study how the dynamics of the reservoir affect the performance, as well as, a way to test the reservoir computers performance in terms of the essential properties, and how to optimize the performance of the reservoir based on the inherent dynamics. Essentially, we give a method which allows for the optimization of reservoir computers by maximizing separability (the nonlinear transformation) while avoiding a sensitive dependence on initial conditions by consistently finding dynamics which give repeatable nonlinear and distinguishable responses which are necessary for optimal performance. Finally, we present a free-space reservoir computer that was optimized with our technique which classifies spoken digits at record speeds, 71 million digits classified per second and an accuracy of 99.9 %.

A second application is high-speed random number generation which is of interest for many applications including encryption and machine learning. In this thesis, for the first time, we characterize the chaotic carrier dynamics generated by ECLs, in the laser's active region and demonstrate that these dynamics which are created with sufficient optical feedback can be utilized as a novel high-speed entropy source for random number generation. The utilization of the chaotic voltage dynamics as a simpler entropy source when compared to the current state-of-the-art is demonstrated. Further, its simplicity is due to the inherent superiority of the voltage as an entropy source which is characterized here, for the first time.

In addition, we utilize and stabilize a specific regime, on the route to chaos, known as limit-cycles (sinusoidal, microwave oscillations) as a tunable, X-band microwave generator. These inherent sinusoidal dynamics are self-generated by these systems and have been

previously demonstrated by us as a simple microwave generator. But, the previous system could not provide the phase/timing stability needed for today's applications. Here, we stabilize this system with optoelectronic feedback and create a competitive generator in terms of stability, tunability, and simplicity when compared to the current state-of-the-art.

Finally, a laser diode is employed as a detector in order to replace a photodiode. It was demonstrated in place of a photodiode in a CD-ROM drive. Specifically, a beam-splitter was removed from a commercial CD reader such that optical feedback is re-injected back onto the laser diode itself instead of onto a separate photodiode. Next, the terminal voltage was monitored to detect variations in reflectivity of a spinning CD-ROM, as well as, to image the chaning reflectivity of a defraction grating. Thus demonstrating that a laser can be utilized to image changing reflectivity of a surface and that a laser can be employed as a photodiode in cases where employing a photodiode is expensive or impossible due to space.

CHAPTER 2
UNDERSTANDING DYNAMIC TRANSITIONS

2.1 A Brief Discussion: Nonlinear Dynamics

Here we do not aim to have a complete set of notes on nonlinear dynamics and chaos theory with rigorous mathematics which can be found in many great textbooks [1, 2], but our goal is to aid the typical engineer/scientist in understanding broad definitions from nonlinear dynamics which are needed to understand this thesis. Dynamical systems can be described by phase space which is a multidimensional space in which each axis describes a system variable needed to know the state of the physical system. Therefore, by utilizing phase space one can map the dynamic behavior of physical systems by analyzing trajectories or the path with which initial conditions take as a function of time. Attractors are points in phase space with which trajectories are drawn, and the set of points in phase space which end up on the attractor are its basin of attraction. Starting points around a stable (unstable) attractor tends to converge (diverge) to (from) the attractor.

Typical dynamics observed in nonlinear dynamical systems experimentally and numerically are steady-state solutions (fixed or equilibrium points), limit-cycles (alternation between two fixed points), quasi-periodic (the dynamic interplay of two incommensurate frequencies), period-doubling (a frequency halving of a limit-cycle), and chaos (sensitive dependence on initial conditions) [2]. Further, chaos is characterized by a set of deterministic trajectories which are bounded and display a sensitive dependence on initial conditions. In other words, a dynamical system in which small variations in initial states can greatly change the output/trajectory observed. More broadly, chaos has been observed experimentally in many different dynamic systems [1], and a typical study in such systems are identifying the route to chaos. In basic terms, the route to chaos describes the transition of

a dynamic system from constant operation to chaos as a system variable is varied. Further, physical systems are often accompanied by numerical models which are developed and explored in order to help explain the routes observed in the experiment.

Routes to chaos are studied with bifurcation diagrams which are a mapping of experimentally/numerically observed solutions of a system as a system parameter is varied, Fig. 2.1. The parameter which is varied in a bifurcation diagram is known as the bifurcation parameter, r. As a bifurcation parameter is changed, a bifurcation diagram allows one to identify bifurcation points or places where the dynamics transition from one to another, an example in Fig. 2.1 at $r = 3$. A typical transition observed numerically/experimentally is a Hopf bifurcation or a critical point where a steady-state solution bifurcates to a periodic solution. Another typical transition is known as a crisis which can be described as a sudden change in the dynamics which can for example be born from the collision of several attractors [2]. Two typical "textbook" routes to chaos are quasi-periodic and period-doubling routes to chaos. For period-doubling, Fig. 2.1, the route is steady-state behavior which bifurcates to a periodic orbit, then to a period doubling orbit, then to a period fourthing orbit, and so on. The quasi-periodic route to chaos is a steady-state behavior which through two subsequent Hopf bifurcations gives way first to a periodic orbit and then to a quasi-periodic which lies on a torus characterized by incommensurate frequencies [2].

Different dynamics can be identified with a Lyapunov exponent analysis. A Lyapunov exponent is a way to describe the divergence/convergence of nearby sets of initial states as a function of time [2]. In other words, if two nearly identical initial conditions, one being only slightly different from the other in value, are observed for as a function of time time and their separation in value is analyzed to observe whether the nearby initial conditions are diverging from each other or not. Specifically, it is a measure of the divergence/convergence rate in different directions of phase space for the trajectories resulting from nearby initial states. An especially important characteristic from the analyis is the sign of the largest exponent (largest Lyapunov exponent). In other words, whether the largest

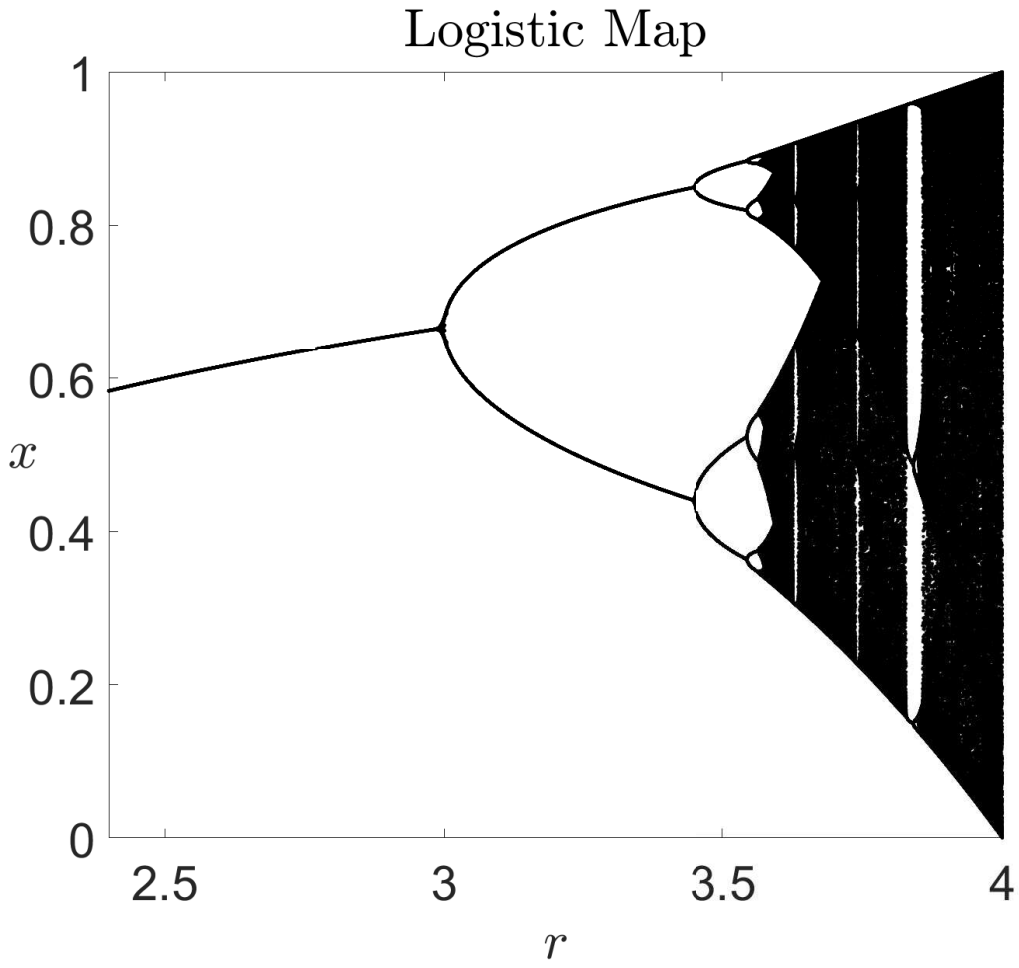

Figure 2.1: A bifurcation diagram of the logistic map showing a period doubling route to chaos.

exponent is negative, zero, or positive which gives an indication whether the dynamics are collapsing, maintaining, or diverging. In a steady-state (fixed point solution) the largest Lyapunov exponent is negative indicating that all dimensions are converging to the steady state. In periodic, limit cycle, dynamics the largest Lyapunov exponent is zero indicating that the system is maintaining in one dimension but collapsing in all others. Finally, in chaos a positive largest Lyapunov exponent is observed indicating overall expansion in one dimension and a sensitive dependence on initial conditions [2].

2.2 External Cavity Lasers

Semiconductor lasers subjected to optical self feedback from a distant reflector (Fig. 2.2) undergo profound modification to the coupled nonlinear dynamics of its three variables which map the system's phase space: the slowly-varying amplitude of the optical field $E(t)$, the optical phase $\phi(t)$, and the carrier density in the gain medium (inversion) $n(t)$. These systems have been studied for nearly 50 years [3, 4, 5], and they provide an important archetype for nonlinear time-delayed systems. Further, these systems are of intense interest for a number of high-speed applications in neuromorphic computing [6], compressive sensing [7], random number generation [8], secure communications [9, 10, 11], and optoelectronic oscillators [12].

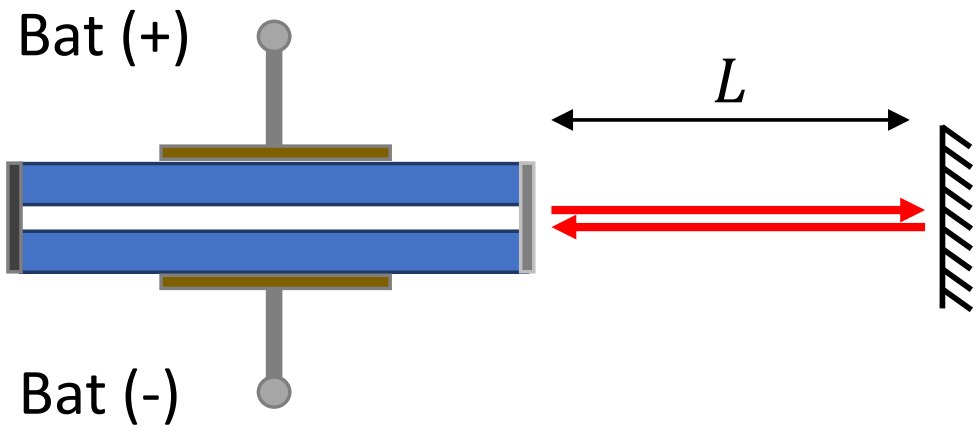

Figure 2.2: A general schematic of an external cavity semiconductor laser setup. An electrically pumped laser diode is subjected to delayed optical feedback from a mirror placed a distance L away.

It has been shown that these systems exhibit five characteristic regimes depending on the feedback level η (bifurcation parameter) [13]. Regime I is characterized by a narrowing or broadening of the laser's wavelength coherence (depending on the feedback phase, sub-wavelength variations of the external cavity). Regime II is observed for slightly larger

levels of feedback where mode-hopping between different optical wavelengths is observed. Regime III gives a narrow linewidth, highly coherent regime with no mode-hopping. In regime IV the dynamics bifurcate from continuous-wave CW emission on the minimum linewidth mode (MLM) to chaos, and finally in regime V or maximum feedback conditions, steady-state operation is observed again. Two distinct chaotic regimes can be observed, *viz.* low-frequency fluctuations (LFF) and coherence collapse (CC). They manifest a loss in optical coherence and a multi-GHz broadening in the spectrums of the optical intensity, voltage, and phase. The fast-pulsing dynamics of LFF were seen experimentally in [14] confirming the theoretical mechanism related to a "Sisyphus" buildup and release associated with a chaotic itinerancy of the trajectory's progression to the maximum gain mode (MGM) [15], and it was recently resolved experimentally for all three dynamic variables in [16]. Therefore, a consensus has been reached on the chaotic trajectories and mechanisms behind the LFF regime, and we focus on CC which also displays a multi-GHz broadening, but is preceded by other dynamics which need to be interpreted in order to understand the route to chaos.

In the route to chaos, there are two main frequencies whose interplay gives which route is observed. First is the relaxation-oscillation (RO) frequency f_{RO}, which results from the exchange between photons and carriers in the gain medium when either the photon or carrier population is perturbed. The other frequency is set by the feedback time delay $\tau = 2L/c$ (with L the external-cavity length and c the speed of light) associated with the round-trip time of light in the external cavity. The frequency difference between the ECMs f_{ECM} is the external-cavity free spectral range, *i.e.*, $f_{ECM} = \tau^{-1}$. f_{ECM} is thus approximately the frequency separation between the ECM fixed-point solutions of the harmonic-oscillator-like optical modes associated with the external cavity [3]. Recently another frequency, the feedback-induced frequency shift of the optical frequency, was shown to determine which type of chaos is observed (strong or weak) [17].

The Lang and Kobayashi (LK) model, a set of coupled delay differential equations for

$E(t)$, $\phi(t)$, and $n(t)$, is commonly used to describe this system [18]. LK has enjoyed considerable apparent success in predicting dynamical trends as parameters are varied. Experimental evidence for several routes to chaos have been found, *viz.*, quasi-periodic (QP) [19], period-doubling (PD) [20], bifurcation cascade (BC) [21, 22, 23], and subharmonic routes [24]. The most commonly observed route at low current is the bifurcation cascade [21, 22, 23]. Which is characterized by an alternation of steady-state and chaotic trajectories observed in sequence. For larger current, it is the quasi-periodic route identified by Dente *et al.* [25] and by Mørk *et al.* [19] that is most common. The PD and subharmonic routes were shown to exist for restricted ranges of operating parameters. For instance, in order to observe the subharmonic route, it is necessary to tilt the mirror [26, 27] while adjusting injection current J [24]. This route to chaos was explained numerically using multiple reflections and was termed *asymmetric* feedback caused by the mirror's tilt [26, 27]. The PD route was shown to exist if the ratio of f_{RO} to f_{ECM} is an integer multiple for low $J \sim 1.6J_{th}$ with J_{th} the threshold current at $\eta = 0$ [20]. Though as explained in [20] careful tuning of the current and cavity length, while varying feedback, is needed to observe the cascade as predicted by the LK model. We have examined this route briefly and see additional dynamics reminiscent of a bifurcation cascade which complements the previously reported dynamics [20, 21, 22, 23].

Here we reëvaluate published experiments for the "quasi-periodic" route, and for the first time, explain the route using comprehensive experiments. In particular, the measurement of the real-time optical phase reveals temporally which discrete optical frequencies external-cavity modes (ECMs) are involved in the dynamics. We reïnterpret the route as being based on the locking between the oscillation frequencies of $I(t)$ and $V(t)$, and the separation in optical frequency between ECMs participating in the dynamics. This locking corresponds to mixed ECM solutions [28], and it does not correspond to the quasi-periodic route seen in the LK model which essentially predicts the development of quasi-periodic attractors from single ECMs [29].

2.3 Phase Space and Experiment

It is utile to comment here on a few basic features underlying the structure of phase space [30, 31, 32, 33, 34, 35, 29]. Fixed-point solutions of the LK model, *i.e.*, steady-type solutions, lie on an ellipse in the n-ϕ and I-ϕ planes. Possible stable solutions of the system are given by the previously mentioned ECMs while the unstable saddle-node solutions are known as antimodes. In practice, many of the ECMs are either unstable or unreachable due to their narrow basins of attraction [33]. The ECMs are numbered positive and negative relative to the MLM on which the laser initially operates. The MLM is labelled mode 0 and ECMs of higher (lower) frequency are successively assigned positive (negative) integer indices. In other words, ECM m occurs at optical frequency $f_m = f_{MLM} + mf_{ECM}$ where f_{MLM} is the frequency of the CW output of the solitary laser with minimal feedback. The MGM occurs for the minimum value of m for which a fixed-point solution to the LK model exists [36].

Phase space is spanned by $I(t)$, $\phi(t)$, and $n(t)$. Experimentally, we measure $I(t) \propto E(t)^2$ with a fast photodiode, $\phi(t)$ by means of heterodyning with a second frequency-stabilized laser [37], and the laser-diode terminal voltage $V(t)$, small changes in which are proportional to changes in $n(t)$ [38, 16, 22, 39, 40]. We thus *simultaneously* monitor $I(t)$, $\phi(t)$, and $V(t)$, and track the full dynamics in phase space, for the first time, while varying η, and fully characterize and redefine the phase-space dynamics of the route to chaos. As has been demonstrated elsewhere [40, 16, 12, 38], the dynamics in $V(t)$ closely follow those of $I(t)$ with a phase shift due to the large role played by ROs. Thus, in this manuscript we focus on $I(t)$ and $\phi(t)$.

In the experiment (Fig. 2.3), two photodiodes are used to measure the dynamics, one for $I(t)$ and one for the beat signal I_{Beat} between L1 and TLS allowing for the extraction of $\phi(t)$ (Fig. 2.4). We use the technique for phase measurement from [37] except we use a windowing technique to isolate the phase dynamics over the requisite timescale (~ 0.1 ns).

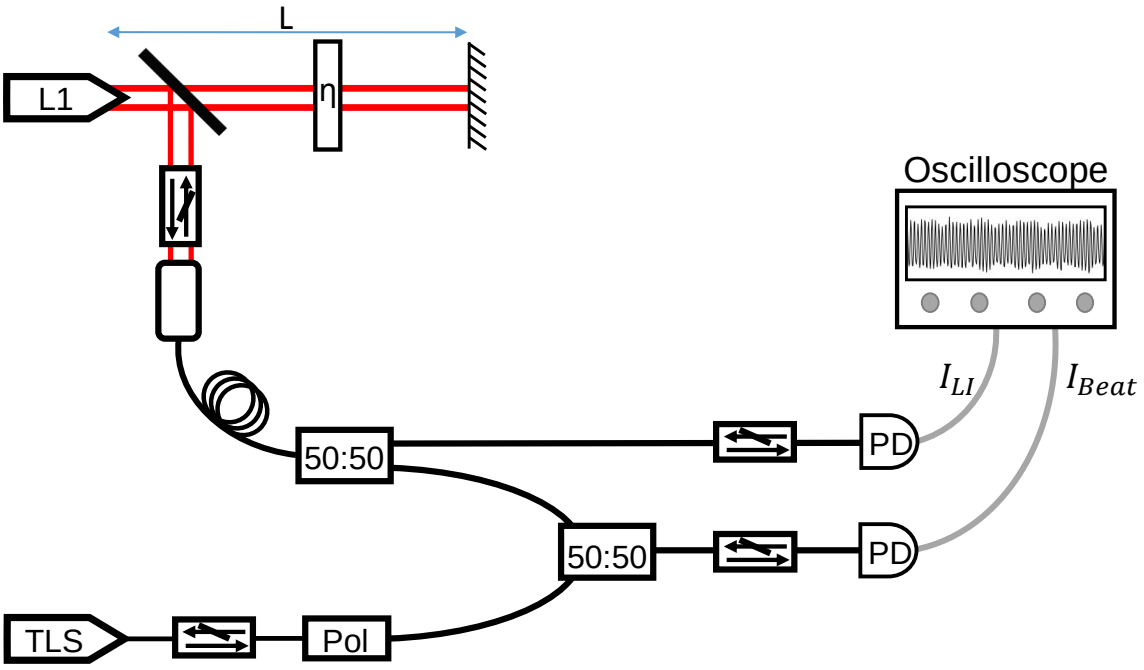

Figure 2.3: Schematic diagram of the laser subjected external optical feedback and heterodyne measurement. The MQW laser under study (L1) is subjected to optical feedback from a mirror with a reflectivity of 99.97%. The feedback (η) is controlled by rotating a quarter-wave plate relative to a fixed linear polarizer. TLS is the tunable laser source for heterodyning. PD, Pol, and 50:50 stand for photodiode, polarization controller, and fiber-optic splitter/combiner, respectively.

For lasers with external optical feedback, the route to chaos as η changes is determined by J and L *via* the interplay between f_{RO} and f_{ECM}. Here we explore the long-cavity case, $f_{ECM} < f_{RO}$, and the cavity lengths utilized were between 15 and 60 cm. Further, we utilized a multitude of packaged [22, 39] and unpackaged [40, 12] DFB lasers manufactured by different labs, to understand the generality of the routes undergone depending on f_{RO} and f_{ECM}. Although several lasers were utilized in the experiment, the experimental data is from the unpackaged MQW laser in Refs. [40, 12]. The Henry factor α of this laser varies from 3-5 depending on the pump current. The length of the laser is 600 μm and the emitting facet has an anti-reflection coating giving a residual facet reflectivity of 0.1%.

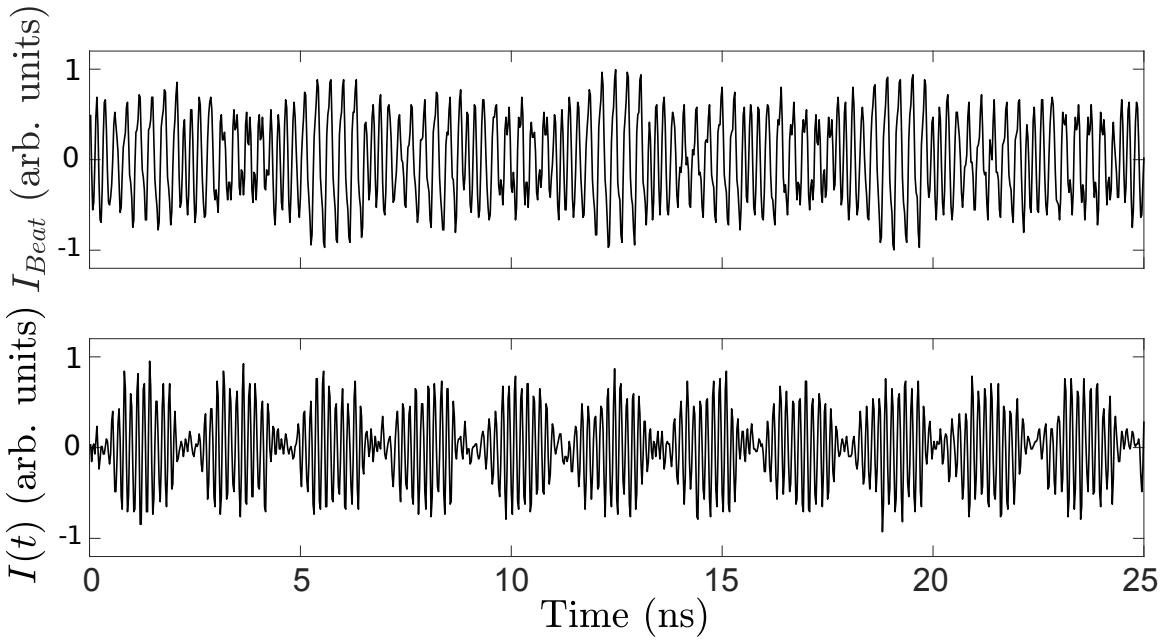

Figure 2.4: Example time traces from the beat signal (I_{Beat}) and optical intensity ($I(t)$) measurements simultaneously acquired from the two photodiodes.

2.4 Crisis Route to Chaos

For $J > 2J_{th}$, a universal route to chaos for multi-quantum-well (MQW) lasers with optical feedback is observed in that it ends up locking on a PD trajectory before undergoing a crisis into chaos. The variation of the dynamics as a function of η has a basic evolution of CW emission leading into closed-loop trajectories and finally CC [41, 39], Fig. 2.5. But, as we have shown with experimental bifurcation diagrams, the initial limit cycle (LC) depends on the initial ECM [41]. In Fig. 2.5, we see the bifurcation diagram starting from ECM 0 which is the most common case. We believe it corresponds to what was observed in [19, 29], and was proposed as a quasi-periodic route to chaos.

What is seen experimentally, in terms of the observed transition of dynamic states can be seen from the time series Fig. 2.6 and spectra Fig. 2.7. The dynamics here are what create the bifurcation diagram from Fig. 2.5. From the time-series and spectra, a steady-state, continuous-wave emission (fixed point) is observed first (a). Followed, by quasi-periodic

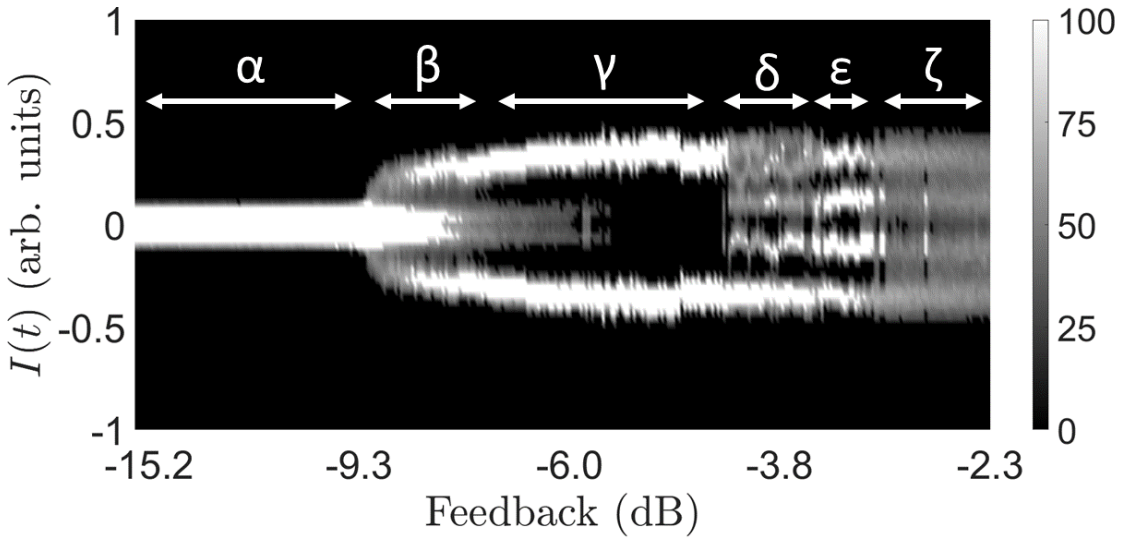

Figure 2.5: A typical bifurcation diagram for high current $J > 2J_{th}$. The following progression of dynamics is observed as the optical feedback is increased, continuous-wave (α) which is followed by a quasi-periodic-like trajectory (β), limit cycles (γ), subharmonic trajectories (δ), period doubling (ϵ), and finally chaos (ζ) [22, 39]. $J = 2.3J_{th}$ and $L = 30cm$. Maximum feedback (0 dB) corresponds to $\sim 16\%$ of the optical power being coupled back onto the collimating lens.

(b) and periodic (c) trajectories. The next transition is to subharmonic trajectories involving a consistent alternation between periodic and double-periodic dynamics (d). Finally, a pure double periodic trajectory is observed in (e) which gives way to chaos in (f). This typical transition is observed unless we force another initial ECM using the procedure of [41], *i.e.*, starting from ECM 0, the fixed-point solution bifurcates into an oscillation of quasi-periodic appearance, β, (around ECM +1) as seen in Fig. 2.8. This is quite different from the prediction of LK, that the first instability gives rise to a LC [19] and from the previous experimental interpretation [19] that this is a "noisy" LC [29]. The LK model, however, does predict the initial movement of the optical frequency toward an ECM with $m > 0$ [33]. From $\phi(t)$, Fig. 2.8, we see that the trajectory is characterized by a large optical frequency range. The transient CW emission portion of the trajectory is around ECM +1, which according to [41, 33] is unstable, but when $I(t)$ is characterized by fast oscillations at $\sim f_{RO}$, the optical frequency is moving between ECM 1 and ECM -3. In addition, we observe that,

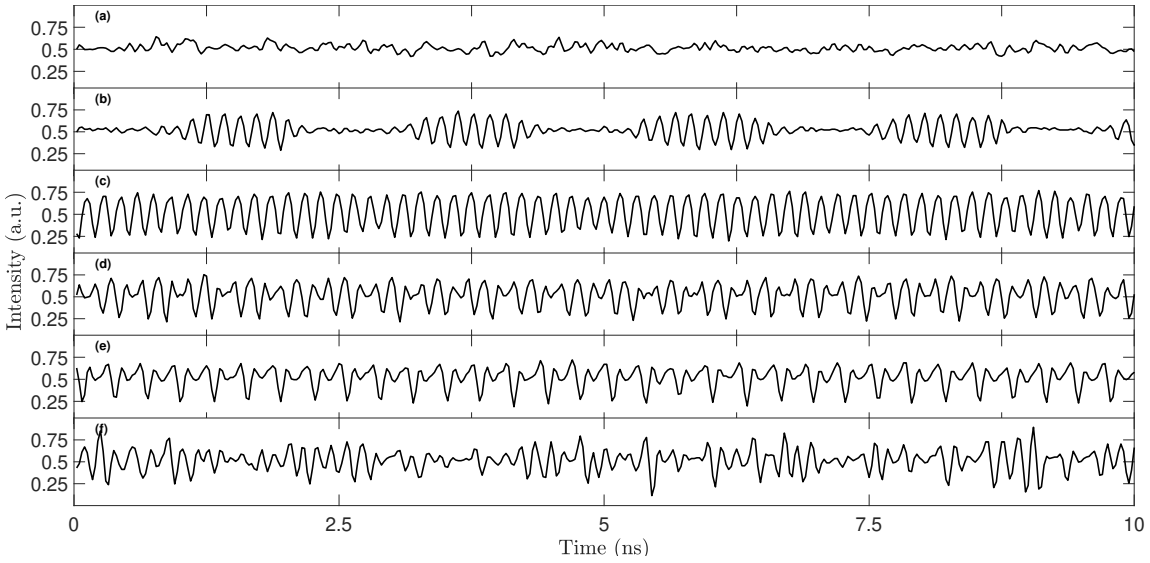

Figure 2.6: Example time-series measured from the optical intensity as a function of increasing feedback. The transistion of dynamic steady-states are as follows continuous-wave (a), quasi-periodic (b), periodic (c), subharmonic (d), period-doubling (e), and chaos (f).

with a period close to τ, the phase space trajectory suddenly moves in the direction of the MGM. It then moves back toward ECM +1, while oscillating at a frequency close to f_{RO} in $I(t)$ and $V(t)$. We suspect the oscillations and rejections are resulting from the interaction of modes and antimodes. As η is increased, the trajectory reaches out further and further from ECM +1 into phase towards negative modes (MGM) as the ellipse becomes larger. The behavior of quasi-periodic appearance is thus not resulting from excursions on a torus that has developed around an equilibrium point, as would be expected in a QP route to chaos. After the quasi-periodic-like trajectory, the optical frequency moves through a crisis to ECM +2, Fig. 2.9. Around this fixed-point solution, several different LCs appear in succession (γ) [41, 39]. Of note, a similar sequence of LCs can be observed with the LK model [42]. The frequency of the first LC is close to f_{RO} and appears to be the multiple of f_{ECM} that is closest to f_{RO}, similar locking phenomena has also been observed in quantum dot lasers [43]. Of note, there are three distinct LCs seen around ECM +2, with each one decreasing in RF frequency by $\sim f_{ECM}$, until the final LC has a frequency of $\sim$7 GHz. An example of one LC is shown in Fig. 2.9.

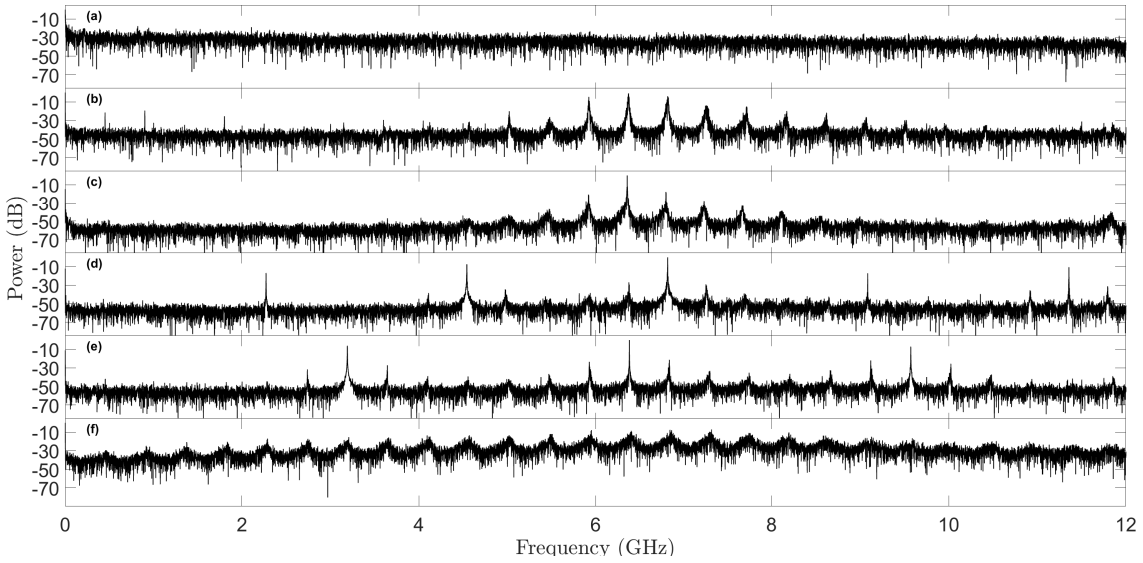

Figure 2.7: Example spectra measured from the optical intensity as a function of increasing feedback. The transistion of dynamic steady-states are as follows continuous-wave (a), quasi-periodic (b), periodic (c), subharmonic (d), period-doubling (e), and chaos (f).

As η is increased further and the ellipse encompasses ECM -7, a bridge in phase space is opened. The bridge connects the right-hand region of $m \geq 0$ ECMs with the most negative ECMs proximate to the MGM. The bridge is characterized in $I(t)$ by a complex trajectory involving both LC oscillations around ECM +3 and PD trajectories between ECM 0 and -7 spanning from across phase space toward the MGM, δ. ECMs +1, and +2 have lost stability and ECMs $m > +3$ are less stable as predicted by LK in [33]. We call this regime subharmonic because the dominant frequencies in the RF spectrum sum to $\sim f_{RO}$. For example, the time series in Fig. 2.10 has peaks in its spectrum at $\frac{1}{4}f_{RO}$ and $\frac{3}{4}f_{RO}$. Interestingly, the system locks for a given η on different complex LCs involving an alternation between a specific number of LC oscillations and PD oscillations. In Fig. 2.10, $I(t)$ demonstrates a case in which there are two LC oscillations for every one PD oscillation. But, overall these trajectories are large LCs reaching from ECM +3 to the MGM. We suspect this regime results from a competition of ECMs because it is possible to have mixed ECM solutions to the LK model [28]. Noticeably, the separation between ECMs 0 and -7 corresponds to 3.5 GHz $= \frac{7 \text{ GHz}}{2}$ indicating a resonance locking between the optical frequencies and half

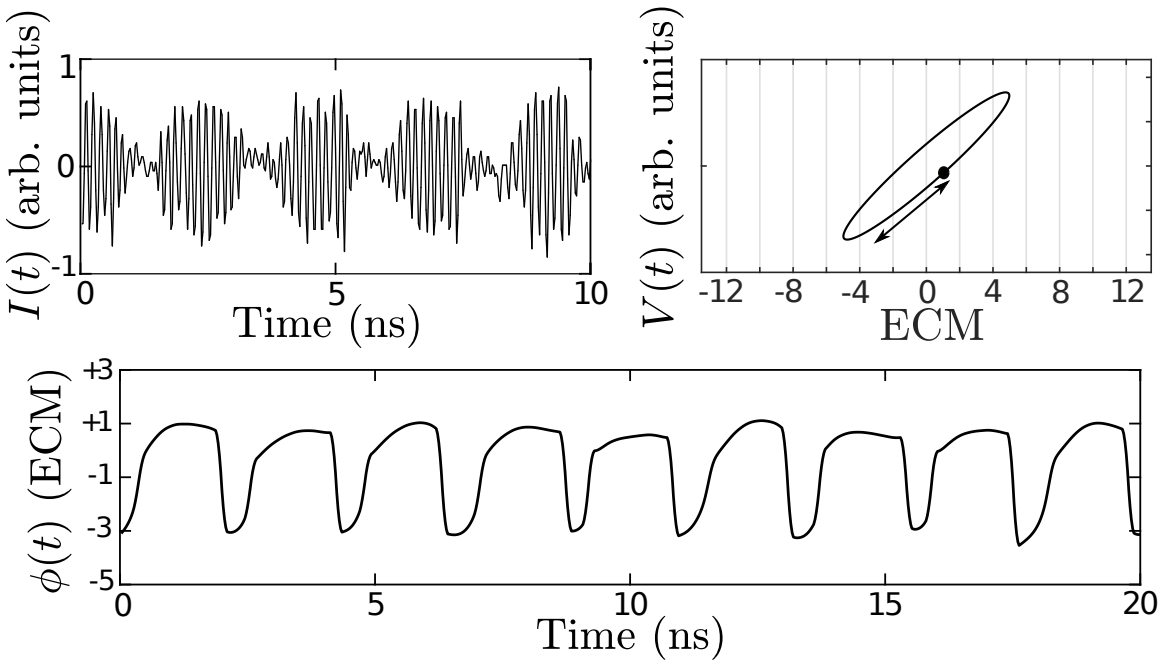

Figure 2.8: The first instability, β, gives rise to a quasi-periodic-like trajectory in $I(t)$ with two distinct frequencies seen in the dynamics. The CW emission in $I(t)$ is around ECM +1, but the fast oscillation portion of $I(t)$ coincides with movement in the optical phase towards the MGM (negative ECMs). As feedback is increased the optical phase moves further and further in phase space towards negative modes (MGM) as the ellipse gets larger (not shown).

of the RF frequency of the last limit cycle. As η is subsequently increased, the trajectory spends less time around $m > 0$ ECMs and more time going between $m > 0$ ECMs and over the bridge. As new MGMs are born, we observe that the active ECMs, involved in the mixed ECM trajectory maintain the separation of 7 ECMs or 3.5 GHz by sliding from positive to negative ECMs following the MGM, *i.e.*, the bridge 0 to -7 becomes a bridge between -1 and -8, etc., confirming the locking to 3.5 GHz of the separation between ECMs. This complex locking of LC and PD dynamics occurs until the ellipse of fixed-point solutions becomes large enough to encompass ECM -11, such that ECMs +3, -4, and -11 are active, from which point the dynamics of $I(t)$ are a stable period-doubled trajectory, ϵ, Fig. 2.11. In the period-doubled regime (Fig. 2.11), $\phi(t)$ switches between modes +3, -4, and -11, each separated by $\sim$ 3.5 GHz, and interestingly the dominant RF frequency of $I(t)$

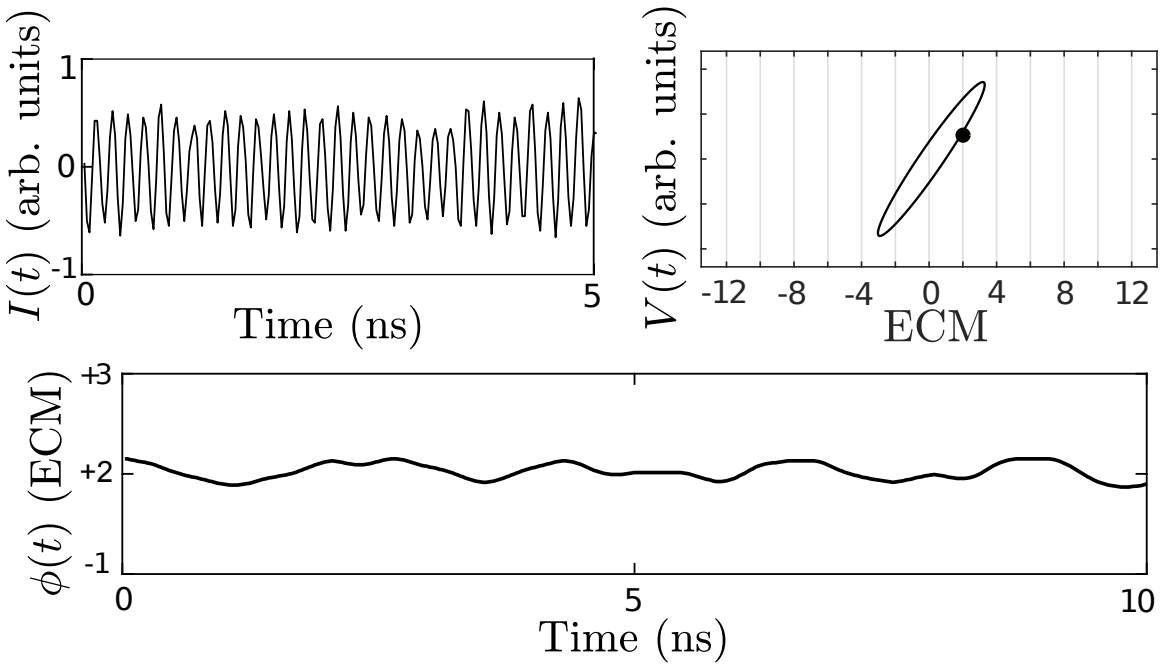

Figure 2.9: An example of a limit cycle trajectory, during γ. We see a sinusoidal oscillation in the optical intensity. The optical frequency is centered around ECM +2.

and $V(t)$ are also $\sim$ 3.5 GHz (Fig. 2.12), or half the oscillation frequency of the last LC around ECM +2 which was 7 GHz $\approx f_{ROF} - 2f_{ECM} = [(+3) - (-11)]f_{ECM}$. We checked that this is consistent for different f_{RO} values, by varying the current and utilizing packaged and unpackaged MQW lasers [22, 39, 40, 12], and we observe the same phenomena. In [28], Pieroux *et al.* predicted similar dynamics, based on the LK model, predicated on the existence of mixed fixed-point solutions, *i.e.*, more than one solution to the model at a time. In that theoretical study, the solutions result in periodic oscillations in, $I(t)$ and thus $V(t)$, with frequency being equal to the separation in $\phi(t)$, as is seen here, providing numerical proof for a bridge in phase space due to locking between the system's frequencies [$I(t)$, $V(t)$, and $\phi(t)$]. Also, we see a rejection after spending time around ECM -11 back to ECM +3, in $\phi(t)$ (Fig. 2.12). We suspect this is a rejection along the unstable manifold of the antimode that is nearby the MGM (ECM -11), similar to what is observed in LFF. This rejection is in fact necessary to maintain the mixed ECM solution since as η increases further the active ECMs stop moving left with the growth in the ellipse because ECM +3

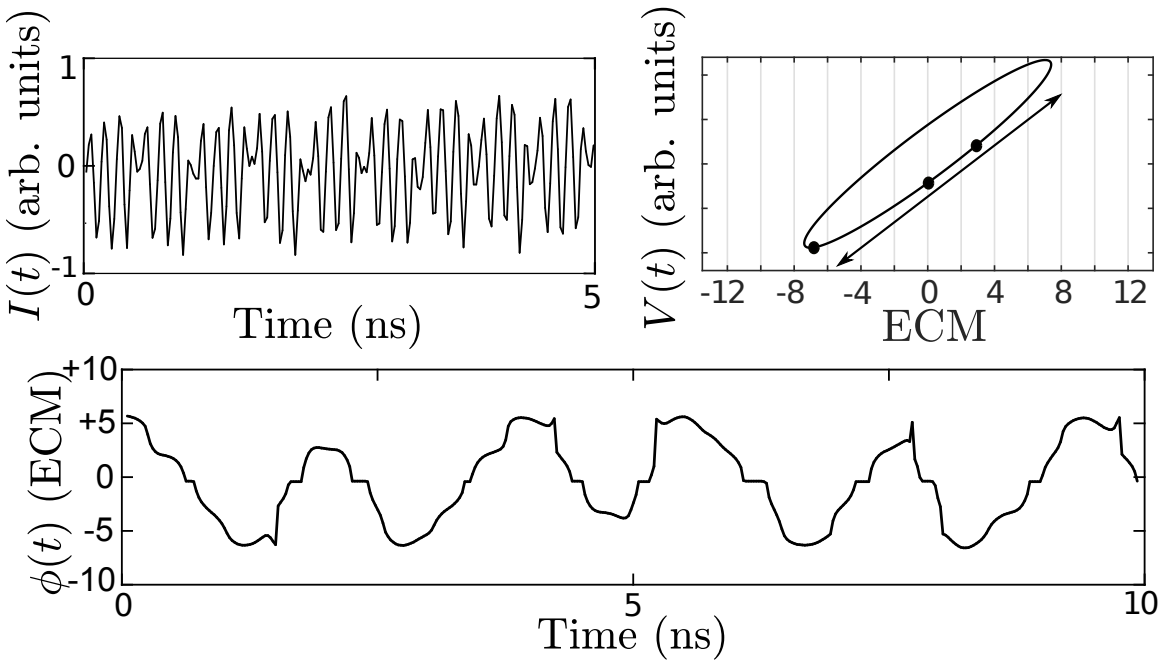

Figure 2.10: An example subharmonic trajectory, during δ, with two periodic oscillations for every one PD oscillation. From the optical phase, we see periodic oscillations around $m > 0$ ECMs and PD oscillations between ECMs 0 and -7.

is the most stable positive ECM. As the feedback level is increased further, the rejections along the manifold become more rare as the antimode moves further from ECM -11 until they no longer occur. At this time, a boundary crisis into chaos is observed.

For the quasi-periodic route to chaos, LK predicts the sequence of dynamics should be a bifurcation in which a LC is born, and subsequently another bifurcation leads to a quasi-periodic oscillation, possibly interrupted by windows of frequency locking, and then chaos [19]. This is remarkably different than what is seen experimentally. We observe CW emission, followed by a pseudo-quasi-periodic trajectory involving multiple ECMs, and a sequence of three stable LCs each with a discretely lower RF frequency. The final LC in the cascade has an RF frequency for intensity and voltage, which equals the separation in optical phase given by the competition of mixed ECM solutions. Finally, when locking occurs on mixed ECM solutions, the system displays PD dynamics, and undergoes a sudden transition to chaotic behavior which we interpret as a boundary crisis born from the inability

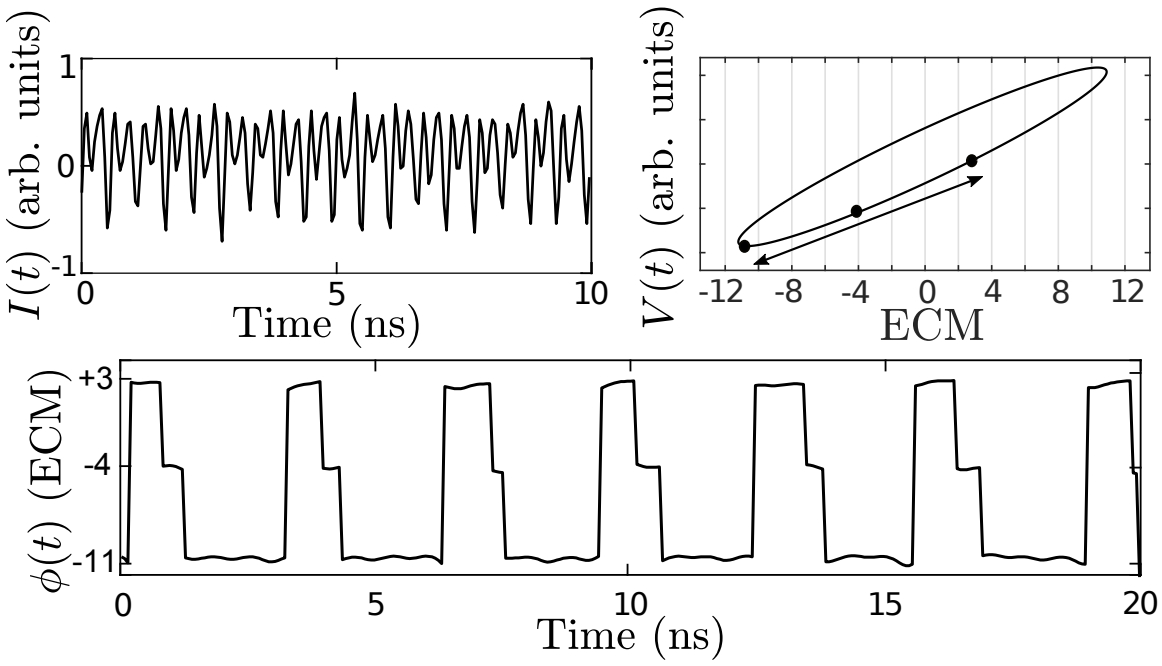

Figure 2.11: Frequency halving of the final LC frequency is observed as a period-doubled trajectory, ϵ, in $I(t)$. The optical phase covers a large portion of phase space (ECMs +3, -4, -11).

to maintain locking all of the system's frequencies without a rejection along an unstable manifold.

On the route to chaos for current relatively large current ($J > 2J_{th}$), with J_{th} being the threshold current, there is a universal route to chaos for multiple-quantum-well lasers subjected to optical self-feedback. After continuous-wave emission, the first instability, if starting from external-cavity mode (ECM) 0 [39, 41], gives rise to a quasi-periodic-like trajectory. As explained in the manuscript, it is an intermittent trajectory involving stable emission around ECM +1 with periodic oscillations when the optical frequency is moving toward the maximum gain mode. After this, a crisis occurs and the laser's optical frequency is in the basin of ECM +2. This is where a progression of three limit cycles occur (Fig. 1). We see a sinusoidal oscillation in the optical intensity at approximately f_{RO}, the relaxation oscillation frequency of the laser. After these limit-cycle trajectories, we move to subharmonic trajectories and finally to a double-periodic trajectory as the system attempts

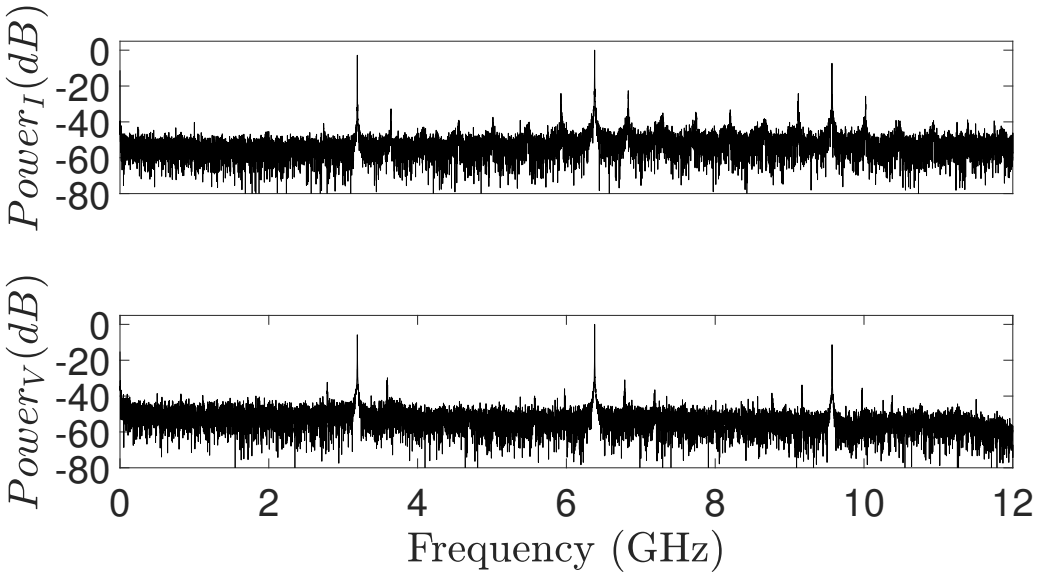

Figure 2.12: An example of the RF locking between the optical intensity (top) and voltage (bottom). Both RF spectra have similar dominant frequencies with main peaks at $\sim$ 3.5 and 7 GHz.

to lock the frequency of all its dynamic variables: optical intensity, carriers, and separation in optical phase, as explained in the manuscript. After the locking occurs, we see a crisis into chaos.

Previous observations of this route for limit ranges of feedback strength were demonstrated, in Fig. 2.13 (a) [19, 29]. In their experiments, the optical intensity, $I(t)$, was not measured directly. Instead, a heterodyne signal was created between a signal generator and $E(t)^2$ from a photodiode. The resulting signal was measured and used to create "phase portraits" between the heterodyne signal and the delayed heterodyne signal $I(t + t_o)$ with $t_o = (4f_{RO})^{-1}$. It turns out that the heterodyning obscures the interpretation. In Fig. 2.13, from the manuscripts [19, 29] -43 dB is described as a "noisy limit cycle". In our experiments, the noisy limit cycle corresponds to the first quasi-periodic instability. The heterodyning removes the modulation from the measured signal. For -34 dB, there was no explanation in the original manuscript, but from observation and comparison to our experiments we see a subharmonic trajectory. The classic smaller loop from double-periodic portions

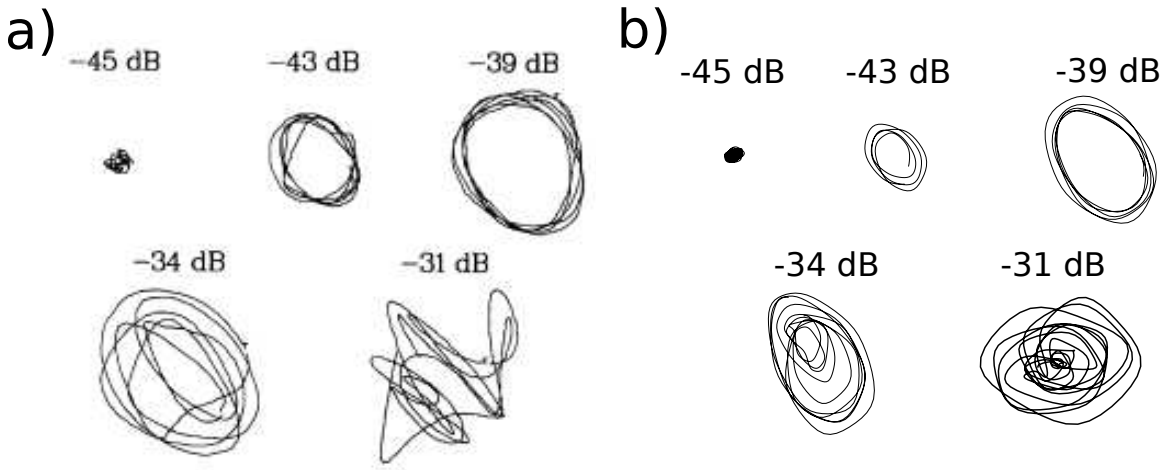

Figure 2.13: The results from [19, 29] are shown on the left (a). Our results can be seen on the right in (b). The curves represent "phase portraits" between a heterodyne signal (optical intensity mixed with a sinusoidal signal) and the heterodyne signal delayed by $(4f_{RO})^{-1}$. These trajectories correspond to continuous-wave, quasi-periodic, limit cycle, subharmonic, and chaos for increasing feedback strength. Of note, the quasi-periodic nature of -43 dB is obscured due to the heterodyne measurement.

of the subharmonic trajectory can be seen in both (a) and (b). We, however, see mainly limit-cycle-like oscillations associated with positive ECMs in the subharmonic regime, as explained in our manuscript. The phase portraits for -31 dB corresponds to a qualitative change in shape and repetition indicating chaotic behavior.

2.5 Conclusion

In conclusion, for larger currents and a long external cavity, we have demonstrated that a universal crisis route to chaos, previously known as the quasi-periodic route, is observed. This crisis route involves locking the system's frequencies (phase, intensity, and carriers) through mixed external-cavity mode solutions. To confirm the generality of our discoveries, we investigated several packaged and unpackaged, MQW lasers operated at various currents giving different relaxation oscillation frequencies and the same bifurcations and crises were observed demonstrating the robustness and generality of the crisis route to chaos for MQW lasers subjected to external optical feedback.

More broadly, the techniques employed here can be utilized to understand and exploit the dynamics for other operating points for these systems such as in the short cavity condition which are interesting for their ability to be integrated easily into systems. Further, it can be utilized to re-analyze and further understand other routes to chaos which were previously identified such as period-doubling and subharmonic routes. The dynamics in these systems may be of interest for applications such as microwave/optical carrier and comb generation.

CHAPTER 3

APPLICATION I: PHOTONIC COMPUTING

Interest has grown recently in developing realizations of brain-inspired computers. Brain-inspired computing in some cases has gone as far as recreating biological neural structures, such as producing a digital reconstruction of a juvenile rat's brain [44]. Also, abstract realizations of brain-inspired computing have been pursued for the potential of an energy efficiency, as well as, computing power that could be improved by several orders of magnitude when compared to current digital computers [45, 46]. In this paper, we exploit the fast, subnanosecond, dynamics of semiconductor lasers to realize a photonic implementation of a reservoir computer (RC), which is a promising type of recurrent neural network (RNN). RNNs are composed of a network of nonlinear, interconnected neurons or nodes that can classify inputs by extracting characteristics from deterministic transients created in response to the network being subjected to an input stream. It has been shown that trained RNNs can be especially efficient in speech and visual object recognition, as illustrated by the recent successes of deep learning-based algorithms [47]. The RNN can be trained to apply the appropriate emphasis (weight) on certain transients over others, but in conventional RNNs, the configuration can be difficult and time-consuming to complete. In such conventional RNNs, a complex, nonlinear training based on recursive adjustments of the weights or connection strength between each pair of nodes is required, which, in addition, only leads to determining local optima. RCs, which are a subset of RNNs, have gained popularity due to the simplicity of training. In RCs, the reservoir itself is untrained, and only a linear, globally optimizable training on the output weights is performed. In practice, this results in fast, verifiable training, which has so far shown state-of-the-art performance in chaotic time-series prediction [45] and spoken-digit recognition [6].

Two concepts have contributed to the rise of interest in RCs: echo-state networks pro-

posed by Jaeger [48] and liquid-state machines by Maass *et al.* [49]. Heuristically, echo-state networks and liquid-state machines are large neural networks that have fixed and randomly connected nodes known as a reservoir. An output layer can be trained to compute a linear combination of the node states to obtain a desired output Fig. 3.1. Maass, Natschlager, and Markram have shown [49] that if two properties, named the separation property (SP) and approximation property (AP) are satisfied, a RC has universal power for computations with fading memory. These two properties describe the RC's ability to distinguish and classify different inputs. Heuristically, SP is such that two saliently different input streams should perturb the system in two different and distinguishable ways (through a projection of the input streams onto high-dimensional transient states) Fig. 3.2, and AP is such that, in the presence of modest noise, an input stream should consistently be mapped to the same target readout by the output layer.

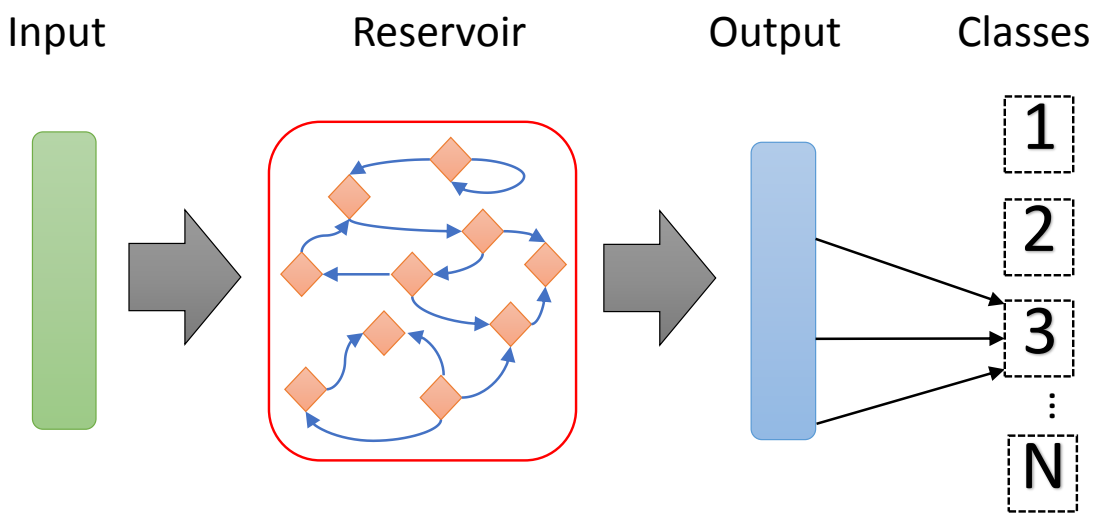

Figure 3.1: A schematic of reservoir computing layers is shown. The input layer is where information is injected into the reservoir. In response to input streams, the reservoir layer creates a rich set of dynamics which are sampled by the output layer. A linear training is applied at the output layer and weights are created which map inputs to classes.

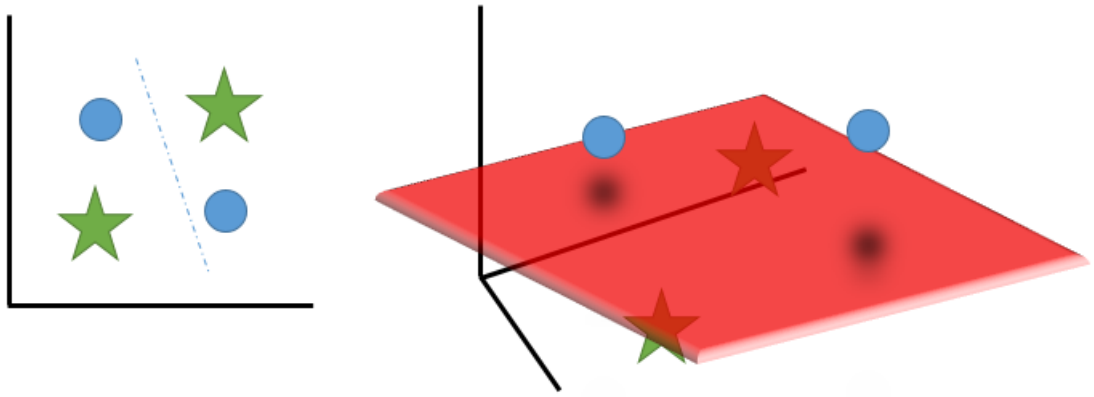

Figure 3.2: A schematic illustration of the separation property is shown. Through a projection of the input streams onto a high-dimensional state space, the circles and stars can be separated in 3D, while in 2D they cannot.

Despite recognition of the importance of SP and AP for RC, there is limited understanding of how they can be *quantitatively* characterized in a realized system, how they affect performance, in what ways they are linked to the characteristics of the dynamical states of the reservoir and to its optimal performance. In this paper, we define a metric and experimental procedure to test directly and characterize the fundamental properties and explain optimal performance in light of these properties. We anticipate that this will assist in establishing a quantitative framework, not only to optimize specific types of RCs, but also to compare RC performance between different types of realizations.

While recent works have shown that optoelectronic based RCs can be successful in performing computationally difficult tasks, there have also been several physical implementations of RCs beyond optoelectronics, including field-programmable gate array based neural nets which have shown promise in performing complex tasks; in these systems digital electronics are used in order to create one or more neurons for computing and training [50]. In Ref. [51], a physical implementation of a liquid-state machine on a field-programmable

gate array that does real-time, spoken-digit recognition was demonstrated. Another more recent implementation using field-programmable gate arrays was shown to not only be able to complete real-time temporal pattern classifications, but also chaotic time-series prediction [52]. Further, it has been demonstrated recently that a single nonlinear Boolean logic element that produces 30 to 300 ns bursts of consistent dynamics can be used to classify short input patterns [53]. In addition, using graphene excitable lasers it was shown that low-level spike processing could be performed, which is necessary for temporal pattern recognition [54]. In Ref. [55], it was proposed that, exploiting the universal computing power of RCs for morphological computing, a robot could be made to control itself.

Another example of a RC using a single nonlinearity and delayed feedback was demonstrated using a physical Mackey-Glass nonlinearity in order to create a single dynamical node. It was shown that by masking the input stream and projecting it onto a high-dimensional state space, spoken-digit recognition could be performed [56]. As mentioned earlier, various optoelectronic implementations using a single nonlinear node and delayed feedback have been shown using various nonlinear elements as the node. In Ref. [57], a laser diode (LD) driving a Mach-Zehnder modulator subjected to delayed optoelectronic feedback was shown to be able to complete spoken-digit recognition [57]. Concurrently, in [58], using a similar system, it was shown that both spoken-digit recognition and nonlinear channel equalization could be done. Later, it was shown that using a single system based on a Mach-Zehnder modulator subjected to delayed feedback, and a switch in the feedback loop, one could switch between two well-known paradigms in machine learning, echo-state networks and extreme learning machines [59]. In [60], it was shown that an entirely optical setup with no electrical components in the reservoir could be used as well. A nonlinearity resulting from the saturation of a semiconductor optical amplifier was utilized and spoken-digit recognition, channel equalization, and a radar-based prediction task were demonstrated. In addition, utilizing the RC based on the nonlinearity of a Mach-Zehnder modulator, a fully analog system was developed such that the input and output layers pro-

cess the input and output streams online instead of using a digital computer for pre- and post-processing [61].

A photonic system, similar to that presented here, with a laser diode (LD) subject to its own optical feedback was demonstrated in [6]. The authors exploited two different modulation schemes, optical and electrical, in order to complete in parallel the identification of spoken digits and the speakers of the digits. Chaotic time-series prediction was also demonstrated. Further, using semiconductor ring lasers subjected to double self-feedback, it was shown numerically in [62] that two independent channel equalization or time-series predictions tasks could be performed simultaneously.

Few publications have focused on ways to improve the RC paradigm. For instance, in [63] online training was completed in real-time allowing for the RC to adapt to the task and to a changing environment. Further, it was demonstrated numerically and experimentally that the machine learning paradigm can be greatly improved by utilizing gradient descent [64]. It was also shown numerically using an approximating model for a specific kind of reservoir exploiting time-delayed feedback, that some of the parameters affecting the optimal reservoir point could be calculated rather than determined through systematic parameter scans [65]. In [66], it was shown for reservoir systems utilizing optical injection as the input mechanism, injection locking between the input and reservoir lasers plays a key role in the performance of the RC. Despite considerable advances in the implementation of RC, the state-of-the-art, as exemplified by the previously cited studies, has left fundamental questions inadequately addressed. The present paper attempts to fill this lacuna.

3.1 Free-Space Reservoir Computing

In this study, we use a free-space laser system based on a LD subjected to external optical feedback from a mirror to create a recurrent loop. The LD is modulated at high data rates through a bias-tee (20 GHz) and a radio-frequency (RF) probe (25 GHz). The output of the system is measured using a 12 GHz photodiode and oscilloscope at 40 GS/s with a

bandwidth of 12 GHz. The experimental setup is represented in Fig. 3.3. This setup is similar in essence to what is presented in [6], with the exceptions that the system used here is implemented in free-space with a significantly shorter delay which allows for faster classification and we are only electrically injecting the input streams.

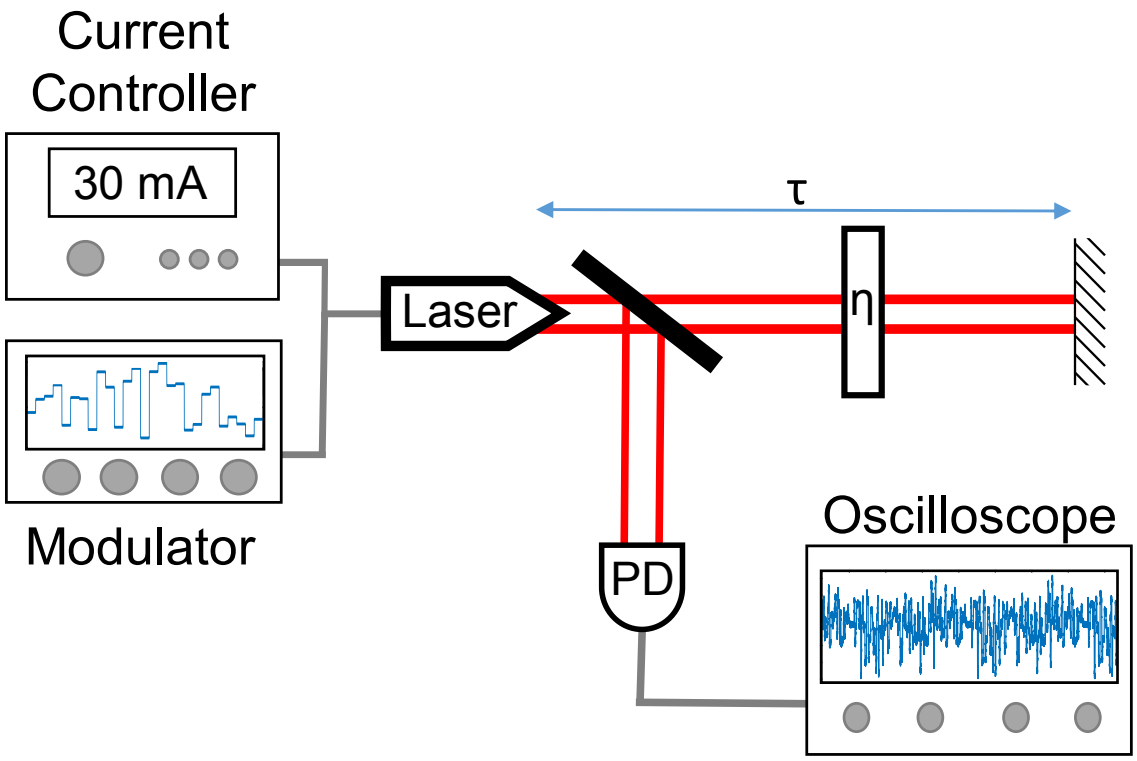

Figure 3.3: A schematic diagram of the setup used in the experiment. The laser diode (LD) is modulated, with a depth of 0.5 V, across the current injection terminals in order to inject the input stream into the reservoir. The level of light being fed back into the LD (η) is controlled by rotating the angle of a quarter-wave plate on a rotation stage with respect to a fixed linear polarizer. A 50/50 beam splitter is placed in the recurrent loop to create an output that is detected using a high-speed photodiode (PD) and an oscilloscope.

A RC operates based on the transient response of a collection of nonlinear nodes. In our realization of a RC, we have a single nonlinear dynamical system (the LD) with optical feedback, but monitor the response within the feedback loop at various time delays

creating *virtual nodes*, Fig. 3.4. It has been shown theoretically [67] that this topology is comparable, in terms of performance, to the originally proposed RC composed of a random network of nonlinear nodes. The relevant transient frequency in our system is the relaxation-oscillation frequency f_{RO}. Relaxation oscillations, damped oscillations between the carrier and the photon populations inside of the LD structure, are excited when the LD's drive current is suddenly perturbed from its present level. Thus, with fast, non-stop current modulation of the LD, we can excite transients that involve relaxation oscillations, which leads to rich, deterministic, and unique dynamics depending on the temporal pattern of the input stream. This underlies the potential of the RC to distinguish between different input streams (current modulation patterns) based on their deterministic output stream (optical intensity within the optical feedback loop as a function of time), in other words, to satisfy the SP.

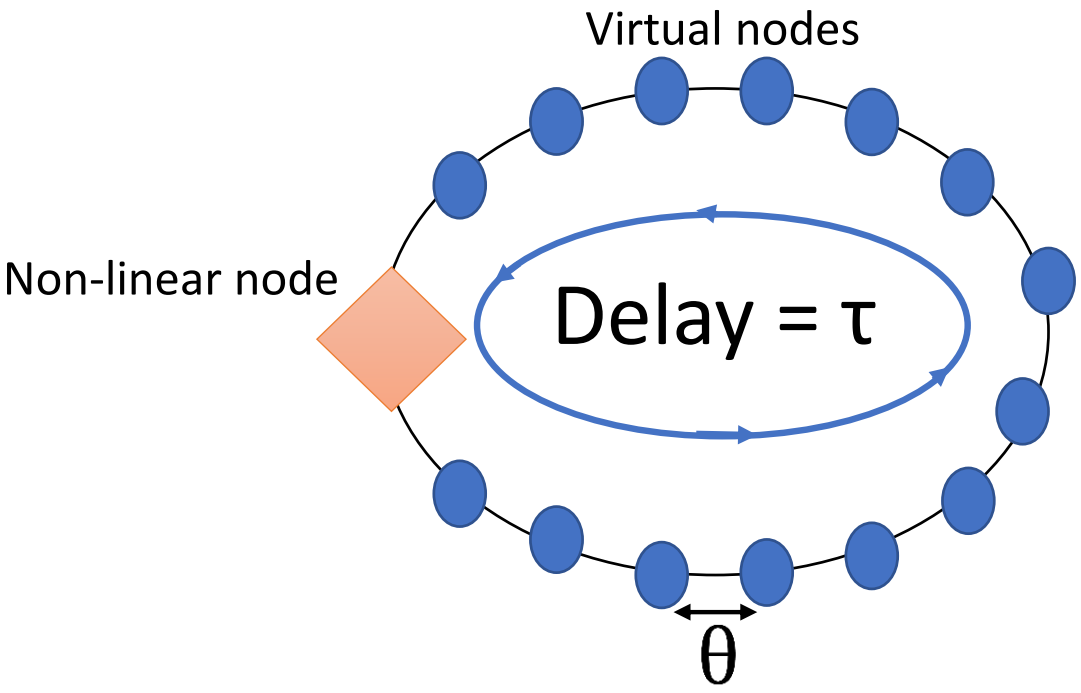

Figure 3.4: A delay line reservoir, with delay τ, is shown. A single non-linear node with feedback is utilized. In our case, this corresponds to a laser subjected to delayed optical feedback from a mirror. The output of the reservoir is composed of temporal sampling of the laser's response with a rate of $1/\theta$.

The free-space RC is demonstrated using a common task in photonic RC: spoken-digit recognition. This classification task, as explained by Lengenstein and Maass [68] is a good test for a dynamical system to serve as a rich reservoir of basis filters and thus for online computing tasks with fading memory. The NIST TI-46 corpus [69] was used; it is a set of spoken digits by five female speakers who speak the ten digits in English ten times for a total of 500 spoken digits. The spoken digit task is based on the NIST TI-46 dataset [69]. It consists of 5 female speakers who utter the 10 digits in English (0-9) ten times each. This gives a total of 500 utterances. The raw audio signal from the dataset is chopped into 130 time slices of equal length which are processed using a cochlear ear model [70]. The way we process the output of the cochlear model for the input layer is described in the following.

The number of virtual nodes is chosen to be equal to the number of channels in the model. Each channel corresponds to a frequency component, thus emulating the cochlear in the ear by performing a Fourier transform of the input signal. After the cochlear ear model, the values of each channel from the time slices are summed into discrete values. Then each discrete value is made a constant value for a duration equal to the inverse of the modulation rate (θ) or the virtual node state (length of a virtual node). The resulting summation is further modified using a binary mask consisting of two values: ± 1. The values of the mask are chosen at random one time and then the same mask is applied to the pre-processed digits. The resulting signal is modulated across the laser as an input stream Fig. 3.5. The 500 digits in the dataset were split into 450 for training and 50 for testing. 20-fold cross-validation was performed for all experiments. Using the outputs from the reservoir and a target function ($\hat{\mathrm{y}}(\mathrm{l})$), k weights (W_l) are calculated by minimizing the mean square error (MSE) between the average output sampled at each virtual node, i.e. the k virtual node states x_l, and the target function. In order to asses the reservoir, the input streams, created from the testing set, are injected into the input layer and the resulting output streams are weighted by the W_k's. The weighted output is then compared to the ideal target function corresponding to the input, thus, allowing us to evaluate if the reservoir was correct.

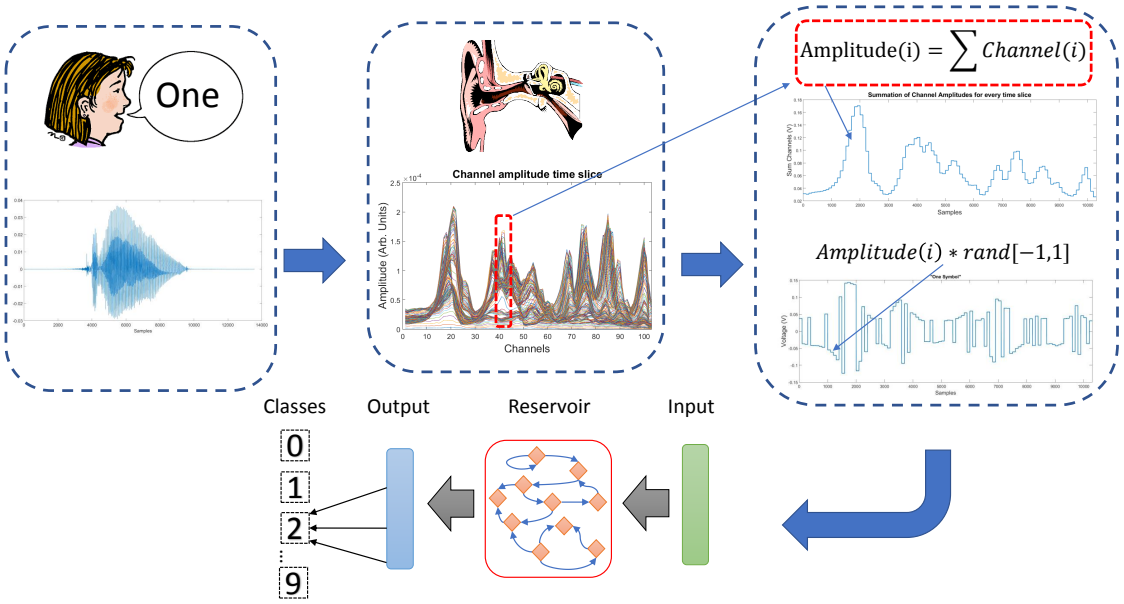

Figure 3.5: A spoken digit from the NIST set is processed using a cochlear ear model. The result of the cochlear ear model is subjected to a random mask which is set one time. Finally, the result is modulated at the input layer causing rich transients in the reservoir which are measured at the output layer.

3.2 Reservoir Properties

The word-error rate (WER) is a practical measure that is typically used to quantify the performance of a RC for spoken digit recognition; however, this measure is not effective to identify the relative roles played by SP and AP. It is a key aim of our work to connect the practical performance of interest to the end user to the physical operation of interest to the designer of the RC. A way to test the SP was previously proposed in Ref. [68]. The method is based on calculating the rank of a matrix composed of node states (reservoir's response) for the different input cases. If the matrix has a full rank this means that all of the inputs create linearly independent responses and can potentially be linearly separated. In practice, we consistently obtain a full rank, but still our output layer exhibits a nonzero WER. Thus,

the method presented in Ref. [68] cannot fully interpret the role played by SP and AP in physically realized RCs, because it relies on a perfectly functioning output layer that is not subject to variations in physical parameters and conditions that occur during experimentation. We therefore propose, and subsequently verify, a metric to describe the quality of the reservoir's ability to separate input streams: the system separation factor (SSF). In other words, the SSF is a quantitative measure of the SP. The SSF is based on several parameters, including, the input and output separation matrices, whose elements D_{ij}^{I} and D_{ij}^{O} describe the Euclidean distance between average inputs and outputs, respectively,

$$\begin{aligned} D_{ij}^{I} &= \left\| S_i^{(I)}(n), S_j^{(I)}(n) \right\| \\ D_{ij}^{O} &= \left\| S_i^{(O)}(n), S_j^{(O)}(n) \right\| \end{aligned} \tag{3.1}$$

with $\|\cdot\|$ the Euclidean distance,

$$\sqrt{\sum_{n=1}^{p} \left(S_i^{(I,O)}(n) - S_j^{(I,O)}(n) \right)^2}, \tag{3.2}$$

where p is the length of an input stream and $S_i^{(I)}(n)$ and $S_i^{(O)}(n)$ are the representative symbols, i.e. the arithmetic averages of the i^{th} input stream I_i and of the i^{th} output stream O_i to and from the reservoir,

$$S_i^{(I)}(n) = (1/N) \sum_{l=1}^{N} I_l(n), \tag{3.3}$$

$$S_i^{(O)}(n) = (1/N) \sum_{l=1}^{N} O_l(n), \tag{3.4}$$

with N the number of input/output streams corresponding to the same symbol, i.e. to the same digit in the case of spoken-digit recognition. For example, D_{35}^{O} describes the

Euclidean distance between the output symbols corresponding to the third and fifth spoken digits. Therefore, by comparing D_{35}^{I} to D_{35}^{O}, we can see the separation caused by the reservoir on the input streams. For m input streams (in our case ten, *i.e.*, one for each spoken digit $[0, 1, 2, ..., 9]$, for a total of $m = 10$), the SSF is defined as

$$\text{SSF} = \frac{1}{m^2 - m} \sum_{j=1}^{m} \sum_{\substack{i=1 \\ i \neq j}}^{m} \frac{D_{ij}^{O}}{D_{ij}^{I}}. \tag{3.5}$$

The SSF is essentially the average ratio of the distance between symbols before and after the reservoir. The SSF is therefore a global measure of the amount of separation between trajectories of internal node states of the system that are caused by two different input streams. We thus consider that the SSF is a quantitative measure associated to the SP. When the SSF decreases, the separation between various output symbols is decreasing, thus leading to symbols that become more alike and are more likely to be misclassified. Therefore, the SSF gives the quality of the reservoir in terms of the SP and is a direct indicator of separability. Notably, the SSF can be generalized in a straightforward manner to higher dimensional input streams, such as images or volumetric data with a suitable measure of distance defined, even where multiple input nodes are present. Nonetheless, even if the SSF is high, the output layer may still incorrectly identify node states from input streams. This can be explained by the AP.

We tested the AP directly by adding Gaussian white noise (δ) to the input stream, measuring the resulting output stream, and checking whether the symbol $S_i^{(O)}(n)$ corresponding to the input and the newly measured output stream was still mapped to the same output by the readout mechanism. Specifically, we tested whether the output, O_i, resulting from the input, $I_i + \delta$, still minimized the Euclidean norm with the i^{th} symbol, $S_i^{(O)}(n)$. If the reservoir's AP is satisfied, then for small noise levels, the reservoir should project the input streams to the same readout as before. In Fig. 3.6, we see that adding noise to the inputs does *not* degrade the performance in terms of WER for low noise levels, but the WER in-

creases rapidly beyond a certain level of noise. This is because when the noise exceeds a sufficiently large level, the input stream is considered by the readout mechanism to be a new, distinct input stream that is mapped to a distinct target output. These results demonstrate that the AP is in fact satisfied in our reservoir, in the absence of additional noise and for small levels of the latter, thus directly and experimentally testing the AP for the first time to the best of our knowledge.

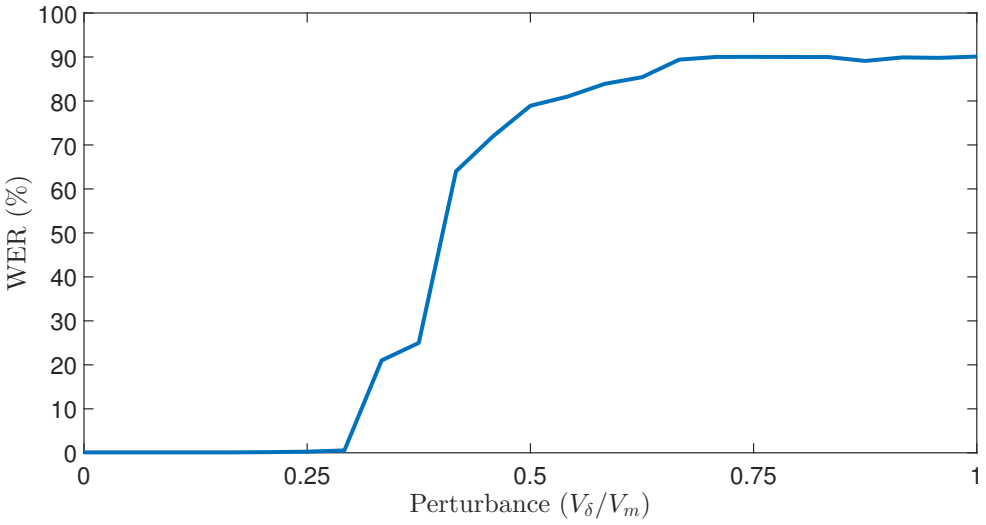

Figure 3.6: Testing the approximation property (AP): Word error rate (WER) as a function of increasing noise level voltage, V_δ, normalized by modulation voltage, V_m. For small noise levels, the RC maps to the same node state as before. For large noise levels, however, it maps the input to new reservoir states.

3.3 Optimal Reservoir Point

Using SSF to see how system parameters affect the reservoir's performance enables us to determine the optimal reservoir point, which is essentially a set of parameters for optimum (minimum-error, in our case WER) performance. The optimal reservoir point includes the following parameters: number of virtual nodes (k), feedback strength (η), injection current

(I), and modulation rate (Φ). All these parameters have a significant effect on the operation of the reservoir as described in [56, 6, 67, 57].

The number of virtual nodes, k, is determined by $\tau = k\theta$, where θ is the duration of a single modulation across the input terminal [56], and τ is the reservoir delay time given by $\tau = 2L/c$, where c is the speed of light and L the physical length of the external cavity. During a single delay time, there are k equidistant segments that correspond each to a virtual node state. The value of k is given by the number of times the laser is modulated during a single delay. The number of virtual nodes, k, (in our case tens of nodes depending on L and θ), gives an indication of the dimension of the system. The cavity length L is directly related to k, and for longer L there are more virtual nodes for a fixed θ. Further, the modulation rate or $\Phi = 1/\theta$ is critical because if the LD is not excited sufficiently fast or with a short enough θ, steady state will be reached and transient behavior lost. If, however, the modulation is too fast, the full dynamics in phase space do not have an opportunity to unfold [6]. Another important parameter is injection current I, because the closer the laser is operated to threshold, the easier it is to excite relaxation oscillations [6], as well as, the larger relative role a modulation of fixed power has on the laser at lower currents versus higher currents. Of most importance in our system, the feedback level (η) gives the strength of the recurrent connection in our RC and dictates the effect of past inputs on future inputs. Also, the amount of light that is re-injected into the LD determines the complexity of the dynamics in the resulting light [56]. As η is increased qualitatively different dynamical regimes in external cavity lasers may be accessed, and even deterministic chaos is possible at sufficiently high feedback levels. The regimes accessed before chaos are characterized, for low feedback levels, by steady continuous-wave emission which, with an increase in feedback, gives rise to a quasi-periodic regime which involves the relaxation oscillation frequency and a second frequency corresponding to the inverse of the delay time, τ. When feedback is increased further, periodic windows are observed and then a regime of intermittency is accessed which is characterized by the switching between periodic regimes, and

finally chaos is reached. We refer the interested reader to a full discussion of the regimes accessed by the laser used in our experiment on its route to chaos in Ref. [40].

For RC, we want rich dynamics for the SP but not a sensitive dependence on initial conditions as seen in broadband chaos, also known as fully-developed coherence collapse [4]. A balance must therefore be found between basic continuous-wave output, which has little connection between past outputs, and fully developed chaotic behavior which displays extreme dependence on past inputs [40, 39, 18, 41].

Chaotic dynamics of a system can be identified by the largest Lyapunov exponent (LLE), which is a measure of how rapidly trajectories diverge in phase space. Therefore, if we know the LLE, we can seek to decrease the rate of convergence of nearby trajectories in phase space; however, care must be taken to ensure that the LLE remains negative to avoid sensitive dependence on initial conditions, which is incompatible with the AP. The LLE was a previously proposed metric for reservoir complexity [71] and studied numerically in [72]. Similarly, a measure of spectral radius or the Jacobian of the connection matrix (a matrix of weight values) between nodes in a neural network has been studied and it was found that the optimal position to operate the system is such that the Jacobian is as close to 1 as possible or at the edge of chaos [68], which in our physical system is given by the range of η just prior to the point when the LLE exceeds zero. We have recently calculated the LLE for the laser used in this work versus η [40], and again for the operating conditions specific to the reservoir in this paper. Since η is positively correlated to the value of the LLE, if we measure the SSF and LLE as a function of η, we can demonstrate that the separation of trajectories given by the LLE leads to better performance in terms of the SP, as well as, whether the optimum is due to an increase in the SP as proposed in the literature.

3.4 Experimental Results

Figure 3.7 shows that the longer the external cavity length L, the better the performance as demonstrated in [71, 67]. The SSF increases with L or k; thus, as expected, the longest

value of L leads to an increase in performance over the shortest L value tested in terms of WER. Thus, as the system dimensionality, k, increases and the number of modulations per delay and length of the input stream increases, the performance of the reservoir improves. In order to determine the effect of modulation rate on performance, we simultaneously increased the modulation rate and decreased the external cavity length such that the number of virtual nodes remained constant. For an increasing modulation rate, Fig. 3.8 shows an improvement in the WER of 0.12 % with an increase in modulation rate of 0.5 GHz. Therefore, faster modulation rates do lead to an increase in performance. We interpret this increase as being due to an increase in dynamic richness by exciting GHz dynamics with a GHz modulation.

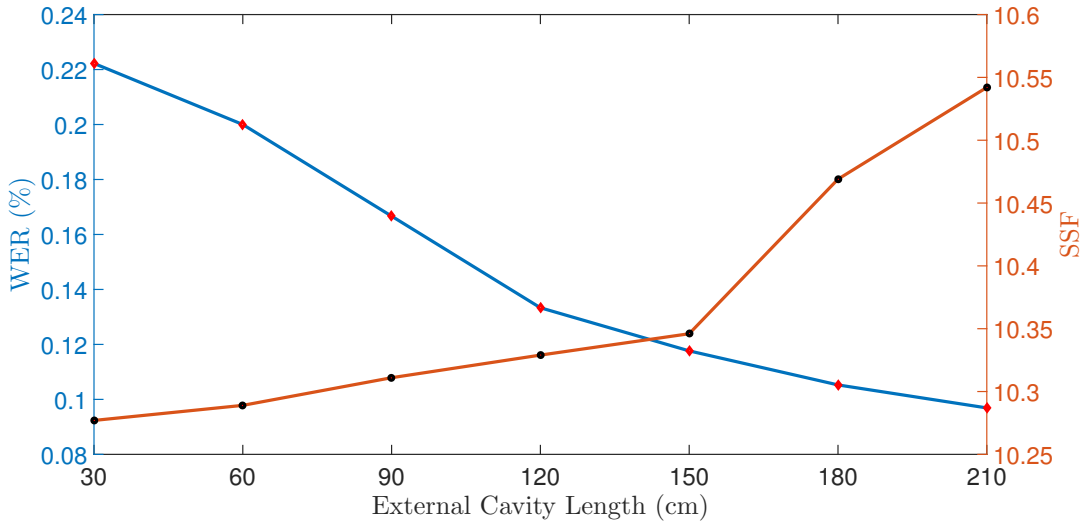

Figure 3.7: External cavity length L: SSF versus L which is proportional to the number of virtual nodes k. As k increases, we see that the SSF increases due to an increase in the dimension of the system. All tests were performed with $I = 30$ mA, $\eta = 16$ %, and $\Phi = 1$ GHz.

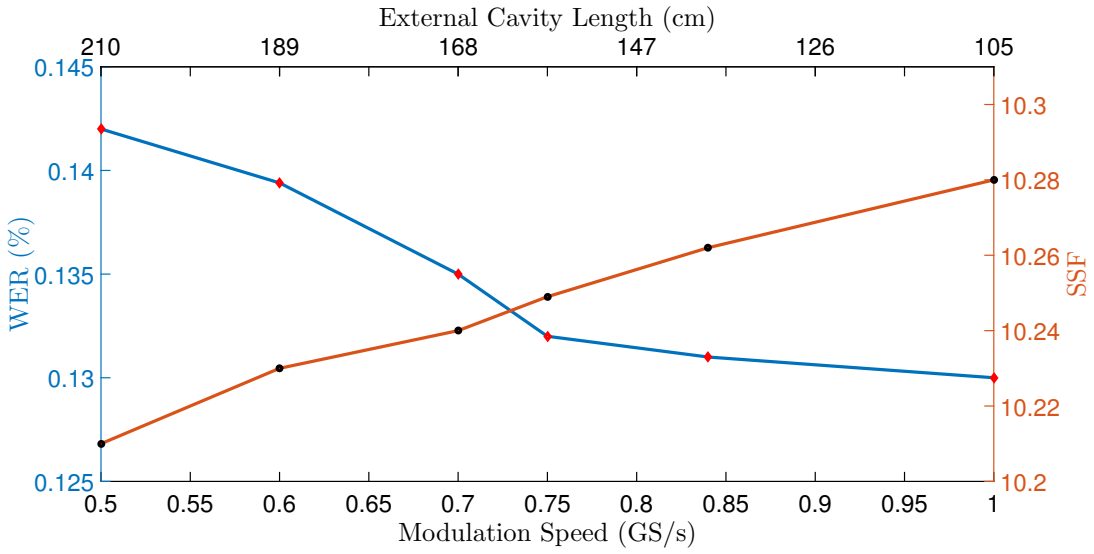

Figure 3.8: Modulation rate Φ: In order to properly excite the dynamics of the system, the laser diode must be modulated fast enough to consistently excite relaxation oscillations. All tests were performed with $I = 30$ mA and $\eta = 16$ %.

The effect of the injection current I is studied in Fig. 3.9 which shows that the SSF is inversely correlated to I. We find an optimum performance at $I = 30$ mA which is at the LD threshold current and maximum SSF. This confirms the experimental results in [6] and the numerical results in [73], which showed that optimum WER was achieved when the laser was operated at threshold and not below, in our case, which gave an increase in the WER. There are several reasons a decrease in the WER is observed at threshold. Modulation close to threshold leads to an increase in dynamic richness because relaxation oscillations are easier to excite close to threshold. Also, the effect of modulation is greater at threshold because the added power of modulation is a larger percentage of the total power (injected power proportional to I plus modulation power) across the LD's terminals. Incidentally, a bias current at threshold leads to the best performance as confirmed by the optimum seen in SSF or the increase in the separation between input streams. This consequently leads to slightly better performance in terms of the WER. Further, because

each digit is encoded over a single delay and a relatively short, free-space reservoir is utilized, we reach a record processing speed of 71 million digits per second for the spoken digit recognition task. Recently, utilizing a different reservoir architecture, a rate of 1 million digits per second was reported [74]. Of note, these speeds neglect the time taken for pre- and post-processing, as is commonly done in the literature [74, 6].

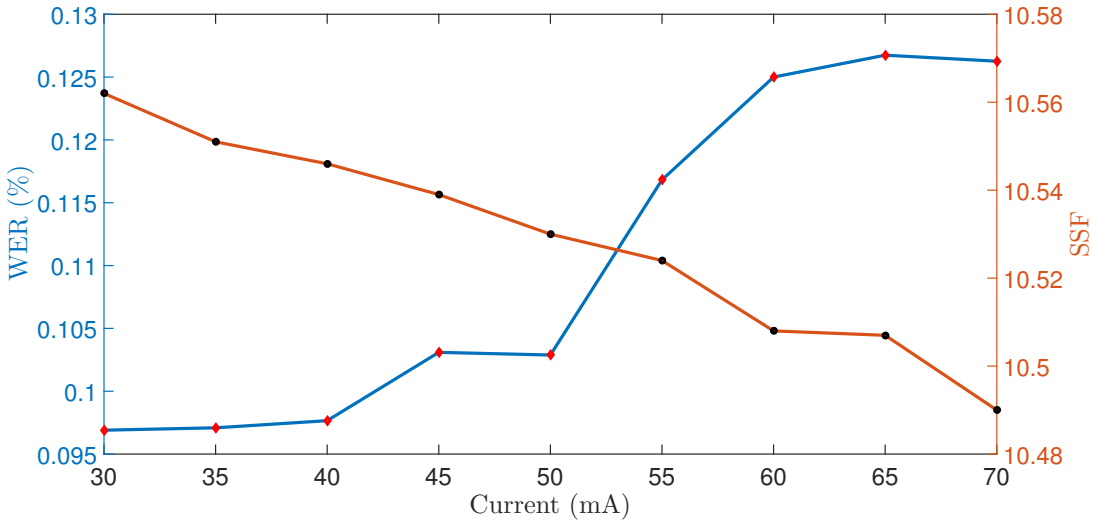

Figure 3.9: Injection current I: Optimum performance is observed at threshold ($I = 30$ mA). The dynamics of the system close to threshold are larger due to relaxation oscillations being easier to excite. All tests were performed with $\Phi = 1$ GHz, $\eta = 16$ %, and $L = 210$ cm.

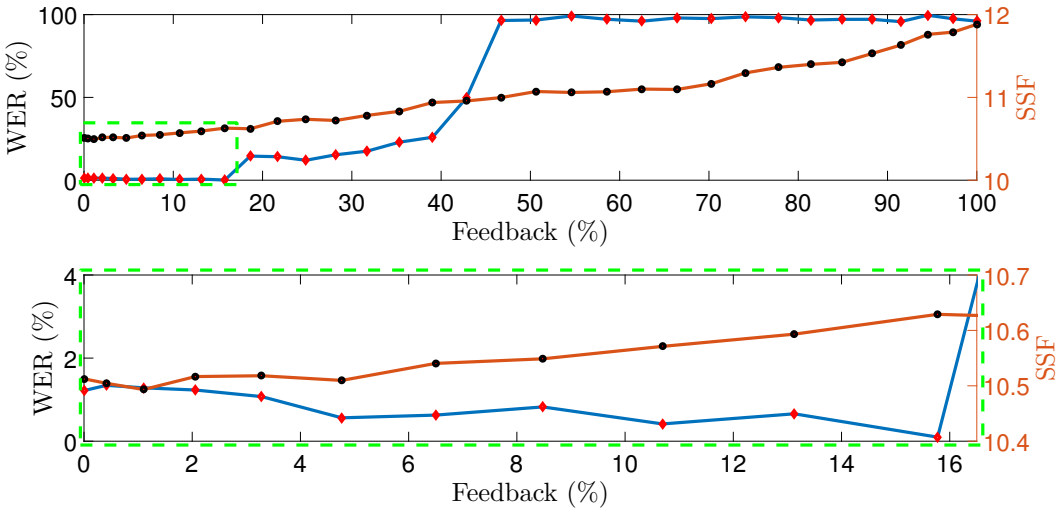

Figure 3.10: Feedback strength η: We find the WER to be minimized at the edge of chaos when $\eta \sim 16$ %. The system's performance improves with η until the point at which the light being re-injected into the laser destabilizes it such that the dynamics are no longer readily repeatable and the reservoir fails. From the zoom-in (b), the performance of the reservoir improves in terms of WER until the optimum of $\sim 16\%$ due to an increasing SSF. After the optimum, an abrupt degradation in the WER is observed due to intermittency being observed in the dynamics and a failure of the AP. Notably, a feedback level of 100 % corresponds to the maximum possible feedback in our system. All tests were performed with $\Phi = 1$ GHz, $I = 20$ mA, and $L = 210$ cm.

In Fig. 3.10, when studying the influence of the feedback level η, we find, as predicted by theory [68], that optimal performance is observed when operating close to the edge of chaos. When operating at low η, the laser is characterized dynamically by stable continuous-wave emission. Under these conditions, we observe high performance in terms of WER. However, when we reach a stable limit cycle at a larger feedback of $\eta \approx 5$ %, we find a further increase in performance due to an increase in SP given by the SSF. The performance continues to improve as the SSF becomes larger until the optimum point of

$\eta = 16$ %. After this point, we see intermittency [39, 40] in the dynamics. Specifically, the laser switches between different periodic and quasi-periodic solutions. Because of the switching in the dynamics associated with intermittency, we train for one set of dynamical behavior from the LD but test on another leading to a degradation in the WER. Thus, optimal performance is seen close to chaos, but with the caveat that intermittency be avoided. This is the idea of consistency which was shown numerically for RC systems [75] and in real neurological systems in rats [76]. As the feedback level is further increased, we see a further degradation in performance to a point where the reservoir does not have the ability to distinguish any input streams when we reach $\eta = 40$ %, which corresponds to the appearance of chaotic dynamics in the reservoir, or 40 % of the power emitted by the LD is fed back onto the LD. We see from Fig. 3.10 that SSF increases consistently with η and Fig. 3.11 shows that the LLE also increases consistently with η. Therefore, the WER improves with SSF for a while until we reach a point where the WER starts to degrade and then finally drastically degrades, i.e. when we reach intermittency and then chaotic behavior. We thus see a degradation in performance even though SSF is improving and thus the ability of the reservoir to separate distinct input streams. This can be explained due to a failure in the AP as illustrated in Fig. 3.12, where different levels of noise have been experimentally added, at different feedback levels. We see that the AP degrades when η moves past the optimal value of 16 %, as the noise level that leads to a given word error rate decreases, for example 30 % (solid red line). Even though SSF is increasing all the way through large η, the dynamics are too rich and the AP fails due to a sensitivity to initial conditions proven by positive LLE, and confirming what was seen theoretically and numerically in [68, 72].

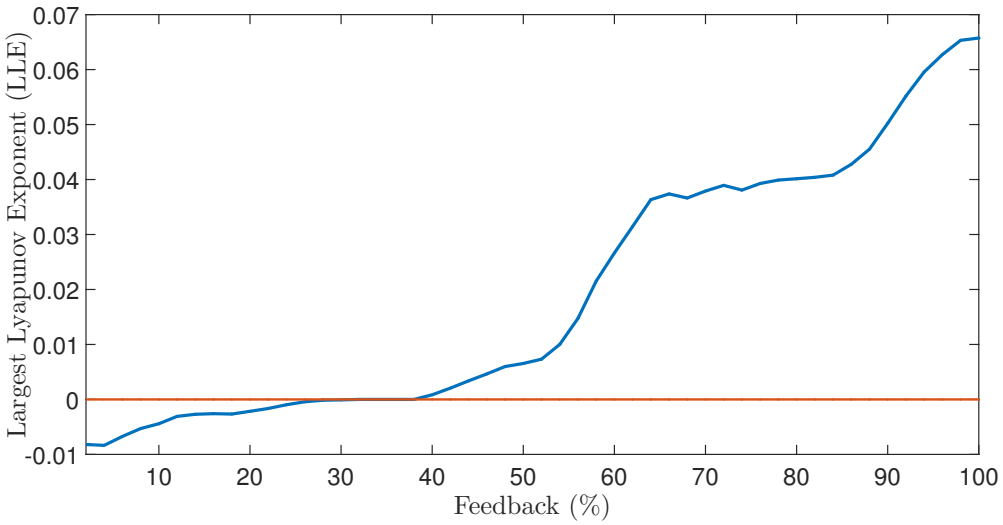

Figure 3.11: The largest Lyapunov exponent (LLE) was calculated as a function of feedback η. When the LLE crosses from negative to positive, we have chaotic behavior.

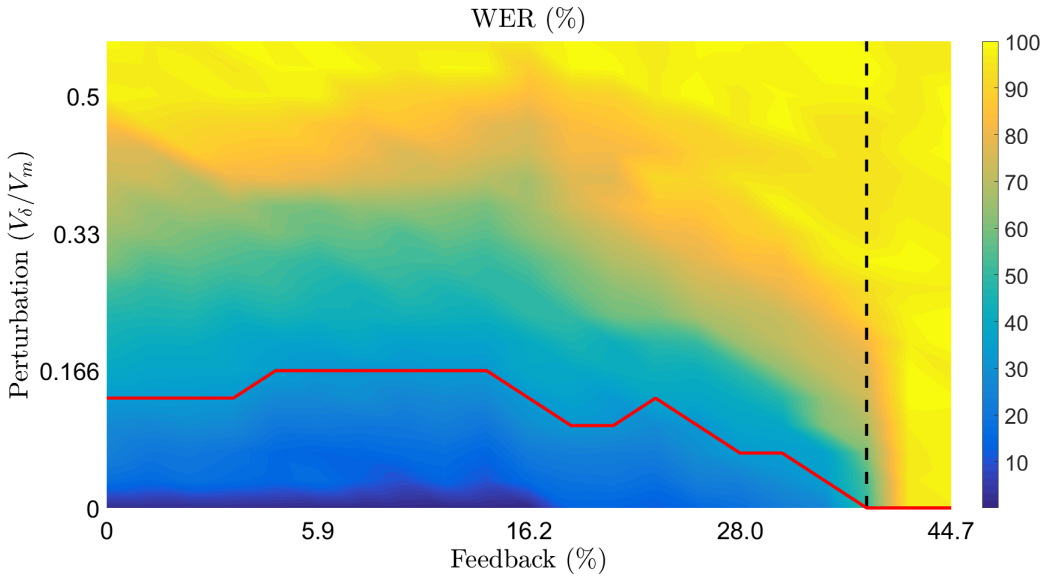

Figure 3.12: Approximation property (AP) as a function of feedback strength η: The vertical dotted black line represents chaos or when the largest Lyapunov exponent exceeds zero $\mathrm{LLE} > 0$. The solid red line represents a $\mathrm{WER} = 30$ %. We see that the AP is satisfied before and up to the optimal point of η. After this point, the AP begins to degrade, during intermittency, up until the point that we see a complete failure when chaos is reached, and the reservoir can no longer perform the task. An η of 100 % corresponds to the maximum achievable feedback for our system, and V_δ and V_m are the peak to peak voltages of the added noise and input modulation stream, respectively.

Under the optimized conditions set by the optimal reservoir point, in our case, ($\Phi = 1$ GHz, $I = 20$ mA, $L = 210$ cm, and $\eta = 16$ %), the RC demonstrated an excellent ability to classify spoken digits. The reservoir, on average, misclassified 1 try out of 1032 during our testing, leading to a word error rate (WER) of 1/1032.

3.5 Conclusion

We have proposed quantitative performance metrics grounded in the dynamics, *viz*. SSF and AP, and have illustrated experimentally how these two reservoir properties are critical for RCs to operate. The metric SSF and the proposed way of testing for AP can be generally applied to classes of problems of any dimension where an RC is used to distinguish among a set of symbols or patterns, such as image recognition. SSF provides a measure of the SP while the ability to distinguish symbols in the presence of noise can be used to characterize the AP. We have developed ways to test both properties, and have shown that the design of a RC should maximize SSF but with the constraint of satisfying the AP. Specifically, we have offered a comprehensive experimental demonstration of where a recurrent photonic reservoir should be operated for optimal performance. Finally, we have studied the influence of the dynamical regime on the SP and AP properties and determined that optimal operation for RC is not reached in the continuous-wave, but rather in the more complex periodic regime, which leads to a greater separation of distinct input streams, while still satisfying the AP. Further, in a broader sense, the SSF metric and the ability to characterize separability and robustness to noise in a dynamic system can be applied to any separation task (of any dimension) based on a dynamical system and not just the task and system employed here.

CHAPTER 4

APPLICATION II: MICROWAVE PHOTONIC GENERATION

Since the first demonstrations of optoelectronic oscillators (OEO) as highly stable radio-frequency (RF) sources [77, 78], they have continually grown in popularity due to their many applications in radar and communications [79, 80], as well as in sensing and measurement [81]. OEOs are part of a broader class of photonic and optoelectronic devices that have been utilized to generate microwave-modulated optical signals. Techniques that involve modulating the injection current or the optical output themselves require microwave sources and as such suffer from noise and tunability issues associated with such sources, and we leave aside discussion of these approaches. One of the simplest purely optoelectronic approach involves beating two optical frequencies separated by the desired microwave frequency [82, 83, 84, 85]. Numerous approaches, however, employ optical or optoelectronic feedback, which is known to enable self-generated oscillations with enhanced stability [86, 87]. In this case, tunability to 10 GHz in the microwave frequency can be achieved by control of various components in the external feedback loop.

OEOs featuring frequency tunability across the X-band (8–12 GHz) are of particularly high importance because this frequency range is associated with several applications in aerospace engineering, such as satellite communications, radar systems, telecomm, and navigation. The classical architectures of OEOs involving km-long fiber delay lines typically provide excellent phase noise performance in this band (below -140 dBc/Hz at 10 kHz offset from the carrier), but generally lack tunability, even though the capability to generate several frequencies in the X-band with the same oscillator appears to be an evident advantage. For this reason, various architectures of tunable OEOs across the X-band have been proposed in recent years. For example, tunability was achieved in the 5.8–11.8 GHz frequency range with a phase noise of -104.6 dBc/Hz at 10 kHz offset in

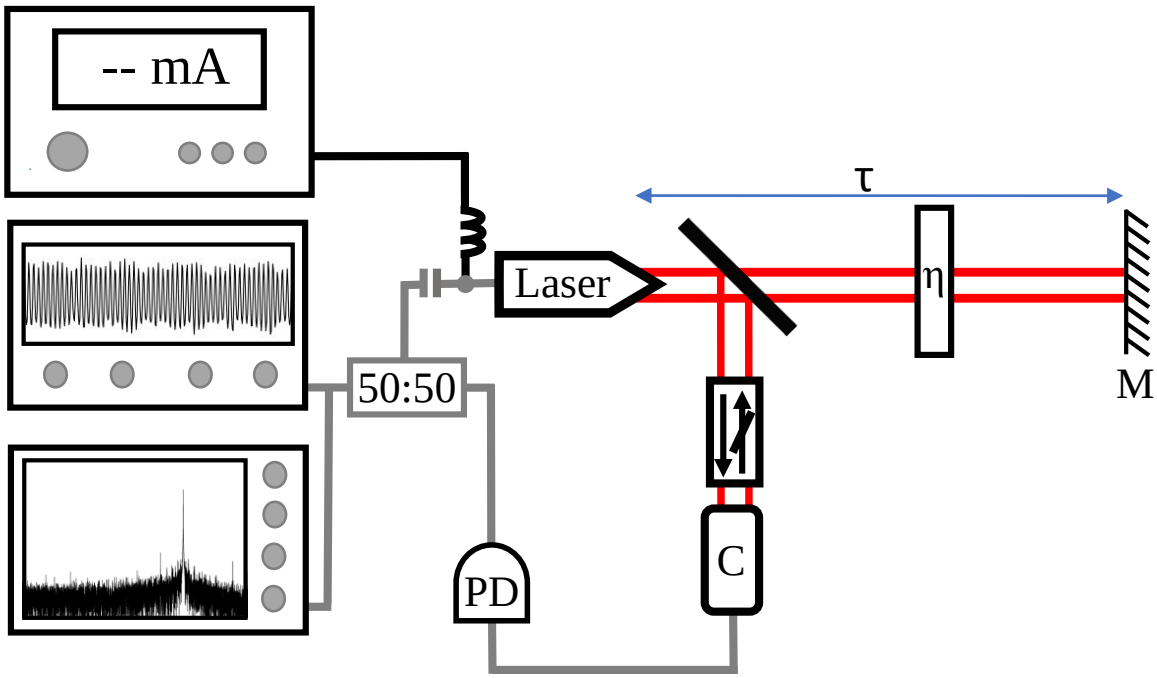

Figure 4.1: Schematic diagram of the free-space OEO. Mirror, M, is an adjustable distance from the laser, which causes the laser's output to be reïnjected after time delay τ. The feedback strength is η, and is set by the angle between a fixed linear polarizer and a quarter-wave plate on a rotational stage. PD, C, and 50:50 stand for photodiode, free-space fiber coupler, and splitter, respectively. A bias-tee is connected to the laser to separate the DC and AC components of the signal. In the optical detection path, an optical isolator and fiber coupler are utilized to limit back reflections and couple the free-space optical intensity into fiber for detection and optoelectronic feedback.

Ref. [88], with an OEO based on a tunable microwave photonic filter consisting of a polarization modulator, a chirped fiber Bragg grating, and a polarization beam splitter. The OEO proposed in Ref. [89] was tunable from 6.9 to 12.8 GHz with -112 dBc/Hz phase at 10 kHz offset, and it used a microwave photonic filter cascading a tunable multi-wavelength laser, a dispersion compensation module and an optical feedback loop. In Ref. [90], the power imbalance between the two ports of a dual-port Mach-Zehnder modulator was combined to frequency-chirping via a fiber Bragg grating to provide 5.8–11 GHz OEO tunability with -107.4 dBc/Hz phase noise at 10 kHz offset. The two-tone OEO demonstrated in Ref. [91] used a dual-polarization modulator, and could output a microwave tunable from

4 to 12 GHz, with a phase noise performance around -105 dBc/Hz at 10 kHz offset.

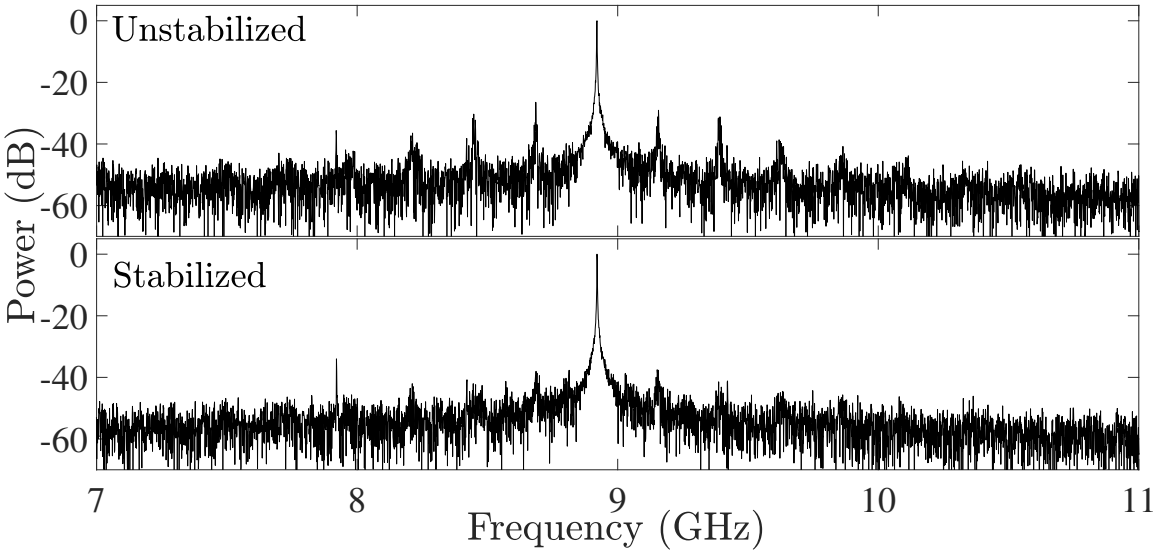

Figure 4.2: Spectra obtained from time-dependent voltage $V(t)$ of a representative OEO operating at 8.9 GHz without (top) and with (bottom) stabilization. A significant reduction in side-band noise is observed in the spectra with stabilization indicating a reduction in jitter and noise. For the spectra shown here $L = 20$ cm and $J = 72$ mA.

There has been recent interest in OEOs that self-generate microwave optical signals without the need for high-frequency electronic sources. In Refs. [92, 93], period-one oscillation in optically injected lasers have been exploited for microwave-photonics applications, but require two separate lasers. In such photonic microwave oscillators, tunability over $\sim$10 GHz has been demonstrated [94, 95, 96, 97, 98, 99, 100]. As we discuss below, we also exploit the intrinsic nonlinear dynamics of lasers to produce microwave-modulated optical signals, but without the need for a separate injection laser.

Recently, a relatively simple X-band tunable OEO was demonstrated that did not require optical-to-electrical conversion (although a microwave-modulated optical signal is produced as a by-product and can be used) by utilizing the high-frequency dynamics of the terminal voltage $V(t)$ from a semiconductor-laser subjected to optical-feedback [12]. Specifically, an OEO tunable from 6.79 to 11.48 GHz was demonstrated, but with substantial jitter and noise of $\sim$ 10 ps and $\sim$ -80 dBc/Hz at 10 kHz offset, respectively.

In external-cavity semiconductor lasers (ECL), there are two major frequencies whose interplay creates rich dynamics. The first is the relaxation-oscillation frequency $f_{\mathrm{RO}} \propto \sqrt{J - J_{\mathrm{th}}}$ where J and J_{th} are the pump and threshold currents, respectively; f_{RO} appears in the dynamics when either the optical intensity or gain-medium carrier density are perturbed from steady-state leading to an exchange between the photon population and inversion in the laser-diode active region. The second frequency $f_\tau = 1/\tau = c/2L$ is the free-spectral range of the delay-induced external-cavity modes, with τ the external-cavity round-trip time, c the speed of light *in vacuo*, and L the external-cavity length (Fig. 4.1) [3]. The OEO is based on the dynamics of several periodic solutions that can be observed for wide ranges of feedback strength η [39, 40, 101], and the frequency of the observed microwave oscillation in the optical intensity $I(t)$ and $V(t)$ is the ECL's f_{RO}, which varies gradually with J [40] and therefore can be utilized as a tuning parameter.

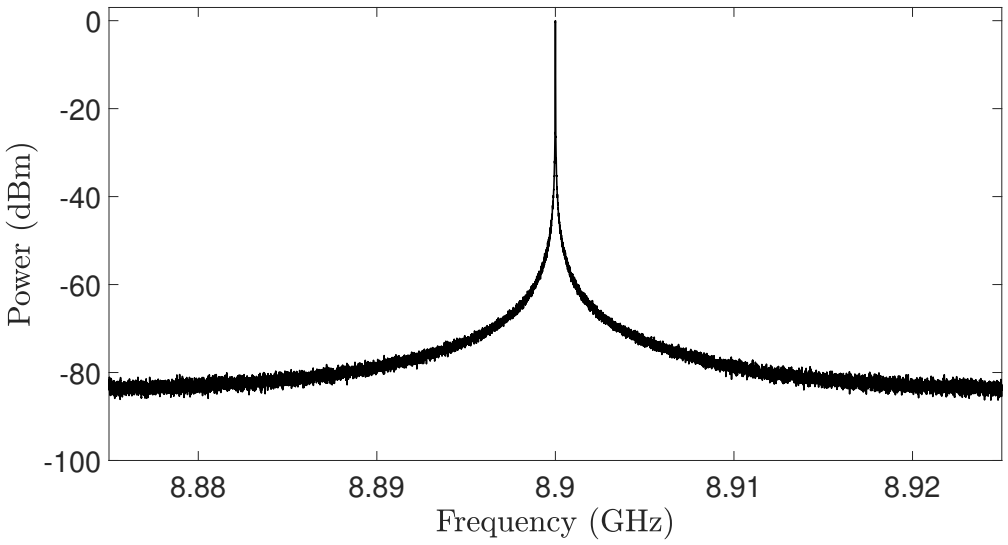

Figure 4.3: Spectrum taken from the electrical spectrum analyzer of a representative OEO operating at 8.9 GHz with stabilization. For the spectra shown here $L = 20$ cm and $J = 72$ mA.

Two features of central importance for most OEO applications are frequency tunability and phase stability. Using the method based on optical feedback, we demonstrate that it is

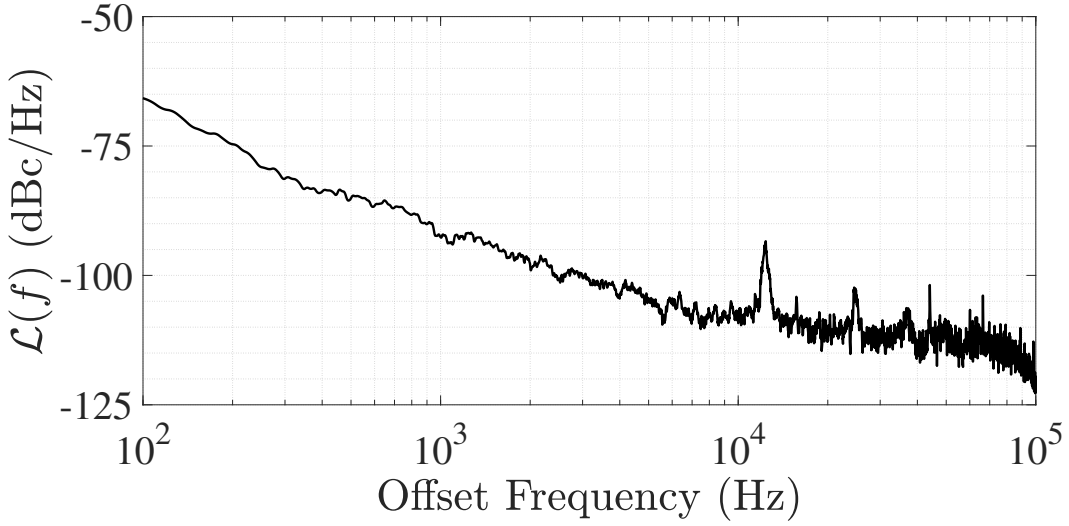

Figure 4.4: Example single side-band phase noise measurement, $\mathcal{L}(f)$, for the stabilized OEO utilizing a spectrum analyzer. The average phase noise for 20 measurements at a 10 kHz offset is -107.3 dBc/Hz.

possible to access the entire X-band with simple adjustment of J. Thus, these systems offer wide tunability but to date lack the phase stability needed for many applications. Here we demonstrate how to stabilize such systems.

4.1 OEO System and Stabilization

The OEO is based on an unpackaged multi-quantum well laser operating at 1550 nm subjected to optical feedback from an external mirror a fixed distance L away [40]. The optical intensity reïnjected into the laser is represented by the feedback strength η in Fig. 4.1; it is controlled by the relative angle of a quarter-wave plate mounted on a rotational stage to a fixed linear polarizer aligned to the natural polarization of the laser [39, 40, 12, 101]. A beam splitter was placed in the optical path in order to obtain a signal for optoelectronic feedback as well as measurement. A photodiode (Newport 1544-B - 12 GHz), oscilloscope (Agilent 80804B - 12 GHz), and spectrum analyzer (Anritsu MS2830A - 26.5 GHz) were utilized to measure the jitter and single side-band phase noise, respectively. A high-frequency RF probe (Cascade Microtech - 40 GHz), bias-T (Mini-circuits - 18 GHz), and

electrical splitter (Mini-circuits 12 GHz) were utilized. Finally, the linewidth was investigated using the built-in linewidth measurement tool of our optical spectrum analyzer (Aragon Photonics - BOSA 400) with a resolution of 10 MHz.

While $I(t)$ and $V(t)$ in an ECL, for the appropriate range of η for given L and J, undergo undamped relaxation oscillations typically in the X-band [12]; without further intervention those oscillations are subject to considerable phase noise. One of the aims of our present contribution is to tame this phase-noise problem. The first stability improvement was based on optoelectronic feedback of the system as shown schematically in Fig. 4.1. Essentially, a beam splitter was placed in the external cavity such that half the optical power could be extracted and converted to electrical signal by a photodiode. Half of the electrical signal was added to the laser's DC nominal injection current J using a bias-T and RF probe. The electrical feedback loop is utilized only for stabilization and *not* for selecting the OEO's frequency. Heuristically, it reinforces the oscillation through a self-modulation of the injection current by the photodetected optical signal. The second improvement was to set f_τ to be close to an integer multiple of f_{RO}. Specifically, f_{RO} was fixed to the desired RF frequency using the DC pump current. Next, τ was adjusted by changing the mirror's position relative to the fixed laser (τ in Fig. 4.1), until $f_{\mathrm{RO}} \approx m f_\tau$ with m an integer. In previous work, it has been shown that a laser diode subjected to optical feedback tends to oscillate at a frequency that is close to a multiple of f_τ [39, 101], even if fro is not itself close to an integer multiple of f_τ. Heuristically, by choosing an integer ratio between the two intrinsic frequencies, we reinforce the tendency of the dynamical system to lock its oscillation frequency to a multiple of f_τ, leading to a more stable oscillation.

4.2 Results and Discussion

In order to characterize the OEO, $V(t)$ was measured and analyzed to extract the jitter and ascertain spectral purity. Figure 4.2 shows the calculated FFT spectra of the unstabilized and stabilized time series $V(t)$. From the spectra, there is an increase in spectral purity

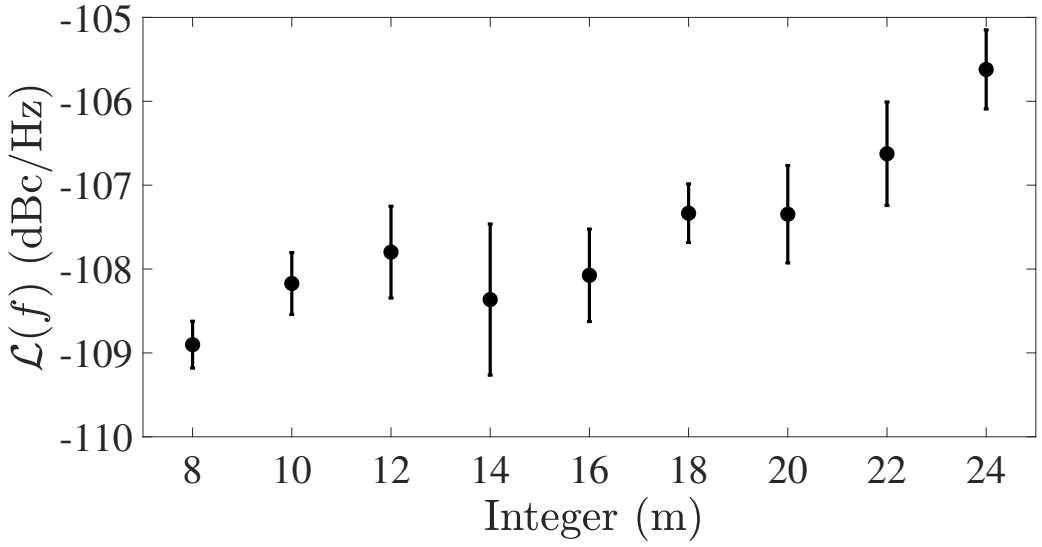

Figure 4.5: Average single side-band phase noise, $\mathcal{L}(f)$, is shown versus the locking integer m. The average phase noise and standard deviation for 10 measurements at a 10 kHz offset are shown. A reduction in the phase noise is observed for decreasing integer values.

and stability given by a reduction in the peak-to-pedestal ratio. To quantify this, jitter was calculated using a demodulation technique [12]. Specifically, it was calculated by assessing the mean time variation in zero crossings between the experimentally measured oscillator and an ideal sinusoid at the carrier frequency. It was possible to ascertain that the jitter was reduced from 10 ps to sub-ps levels, but this method was limited by the oscilloscope's sampling frequency. In consequence, a spectrum analyzer was employed in order to more detailed spectra of the microwave oscillation, Fig. 4.3. Further, a phase-noise measurement was performed using a spectrum analyzer, Fig. 4.4. The phase noise was measured to be ~ -107 dBc/Hz at 10 kHz offset, which is a substantial improvement of ~ 28 dB over the unstabilized OEO [12]. We suggest the strong reduction in noise and jitter are the result of increased coherence created by optolectronic feedback and resonant locking. Subsequently, the influence of the selected integer m on phase noise was investigated. Specifically, ten phase-noise measurements were taken at each integer locking m and the mean and standard deviation are shown in Fig. 4.5. A decrease in phase noise is observed for smaller m, which we attribute to a reduction in environmental factors, as well as, overall system stability

resulting from a shorter free-space delay. Finally, the linewidth of the main peak in the optical spectrum was below the 10 MHz resolution limit of the optical spectrum analyzer. We note that the combination of the two phase-noise-reduction techniques were needed in tandem and that the phase-noise reductions are not additive.

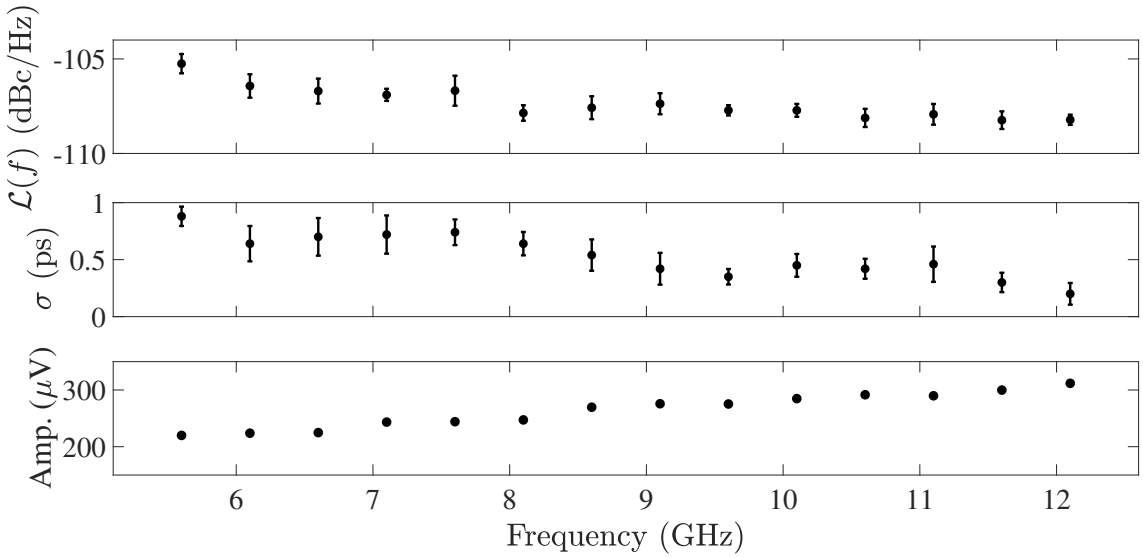

Figure 4.6: Average phase noise ($\mathcal{L}(f)$), jitter (σ), and amplitude are shown as a function of frequency for 10 measurements. A reduction in the phase noise and jitter is observed for increasing frequency because of a relative reduction in the dominance of spontaneous emission noise. Finally, a consistent but increasing amplitude is observed across the tunable range.

While plots of the results for an OEO with output at 8.9 GHz are shown in the figures, by varying J, f_{RO} and hence the OEO frequency can be tuned across the X-band with similar performance. Specifically, we found similar low-phase-noise, jitter, and amplitude characteristics for OEOs from 5.5 GHz to 12.1 GHz with phase noise and jitter less than -105 dBc/Hz and 1 ps, respectively, Fig. 4.6. The amplitude varies by about 35 % across the tuning range ($\sim$200–300 μV) giving a typical output power of 15 μW. Note that in all cases, we employed the same ECL, but had to adjust only η to ensure undamped relaxation oscillations, set L, and vary J to achieve the resonance condition $f_{\mathrm{RO}} = mf_{\tau}$ and desired frequency. Of note, the lower limit of our tuning range originates in the dominance of

spontaneous-emission noise for small J, while the upper limit originates from the cutoff frequency of our oscilloscope.

4.3 Conclusion

A stable optoelectronic oscillator tunable across the X-band is demonstrated using a laser subjected to optical and optoelectronic feedback (ECL). This system utilizes off-the-shelf telecom components and could be made very compact. The stability of the OEO is characterized by sub-ps jitter, a phase noise of -107 dBc/Hz at a 10 kHz offset in the laser-diode terminal voltage $V(t)$. The combination of OEO frequency tunability from ~ 5.5 GHz to ~ 12.1 GHz and low phase noise makes our approach to microwave generation of great potential interest. Our device when compared to the current X-band tunable state-of-the-art discussed in the introduction has competitive or superior phase noise and tunability while offering a more compact and simpler design. Our design is simple by only requiring one laser diode, a mirror, photodiode, attenuator and interconnects. Further, it does not requiring multiple lasers, external modulation source, and/or exotic components such as the case with the current state-of-the-art. Further, let us mention that, it is possible to exploit the microwave-modulated optical signal $I(t)$ for optical clock distribution and RF over fiber. However, our focus in this study is to directly use the microwave electronic signal $V(t)$. In this case, the device is functionally an *electronic* microwave source, even though the physical basis of its operation exploits photonic effects. We note in conclusion that based on the well-established understanding of the nonlinear dynamics of ECLs, we expect that this approach will also enable low-noise OEOs at up to several tens of GHz by choosing lasers with higher f_{RO} (such as VCSELs).

CHAPTER 5

APPLICATION III: RANDOM NUMBER GENERATION

Random bit sequences are commonly utilized in cryptography, machine learning, and simulations. But, due to the need for fast rates and ease of generation most random bit sequences are generated using deterministic algorithms and not truly random entropy sources. Therefore, fast physical random bit generators that can be easily integrated into computers or electronic systems are of interest for these applications. In this paper, we point the way to such a device by utilizing the chaotic terminal voltage of a laser diode. Specifically, laser diodes undergo a profound modification to their dynamical variables, i.e., carrier density, photon number, and optical phase, when subjected to optical self-feedback. It is well-known that these systems can display chaotic dynamics and have been utilized as an archetypical testbed for nonlinear dynamics [3] and for high-speed information processing applications [4]. In the latter context, the use of sampled chaotic optical intensity fluctuations as an entropy source utilized for high-speed random number generation was originally demonstrated by Uchida *et al.* [8]. The generated bit streams were an order of magnitude faster than any other previously utilized physical source. Since then, various realizations and improvements utilizing optical chaos have been demonstrated allowing for faster generation rates up to Tb/s. Various methods based on creating symmetric distributions without bias through post-processing techniques have been proposed, for example, using derivatives [102, 103, 104] and finite differences [105]. To further improve the paradigm, other novel chaotic laser sources and schemes have been demonstrated, such as, through bandwidth enhancement [106], in photonic integrated circuits [107], ring lasers [108, 109], heterodyning [110], terahertz optical asymmetric demultiplexers [111], chaotic solitary vertical-cavity surface-emitting lasers [112], polarization rotated feedback [113], as well as, long on-chip optical feedback [114]. Additionally, fast rates have been demon-

strated utilizing parallel significant bits [115] and parallel-laser schemes [116]. The bit streams in most of the previously cited works are post-processed offline. Interestingly in some cases, real-time implementations have been demonstrated, using delayed feedback lasers [117] and photonic integrated circuits [118]. Recently, an interesting concept, *physical white chaos*, has been proposed and the enhanced chaos leads to random number generation at 320 Gb/s [119]. While there have been many improvements and schemes demonstrated in the field of random number generators based on chaotic lasers, in almost all cases advanced post-processing, complex experimental schemes, optical to electronic conversion, and/or exotic components are required for passing the standard randomness tests and for achieving ultrafast bit rates.

5.1 Voltage Chaos

We demonstrate that the chaotic laser terminal voltage $V(t)$, as a surrogate for carrier density $n(t)$ in the gain medium [38, 120, 16, 40], can be used as a novel, fully electronic, entropy source for random number generation at rates of 40-120 GS/s, where only simple post-processing is required when compared to utilizing the optical intensity $I(t)$. In order to understand the reason behind this improvement, we compare the voltage entropy source with the commonly utilized optical intensity which was measured simultaneously from the same chaotic laser. Specifically, the entropy sources are compared utilizing distributions, delay-correlation, and permutation entropy analysis. It is shown that the simple physical measurement of $V(t)$ is an inherently superior entropy source compared to the optical intensity, $I(t)$. Further, our approach has the benefit of simplicity, while still generating random bit streams at tens to hundreds of Gb/s. Specifically, the system offers a fast electronic entropy source that can be used to generate Gb/s streams without any optical-to-electrical conversion, thus facilitating the use of this entropy source for high-speed computing.

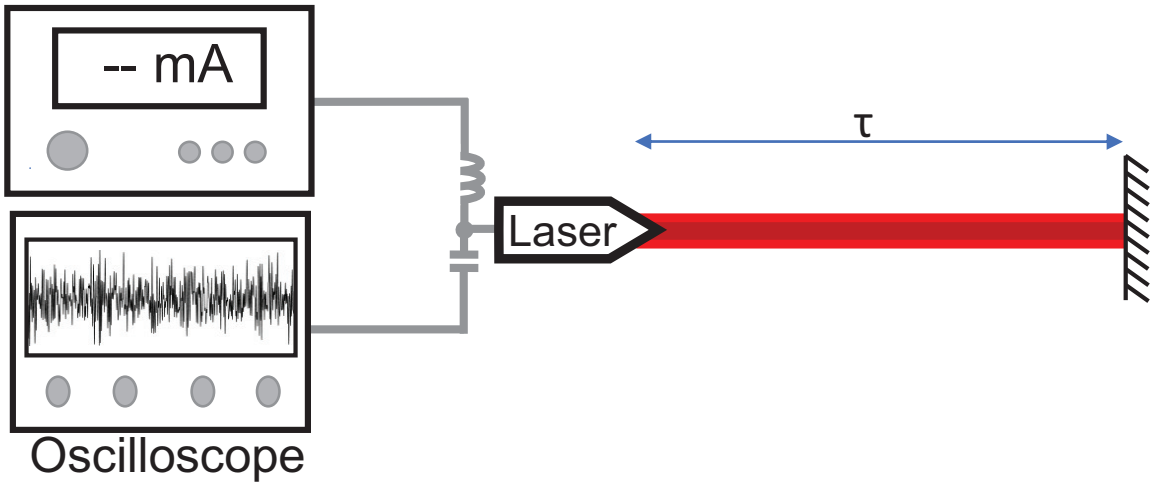

Figure 5.1: The relatively simple experimental setup is shown. An unpackaged, MQW laser is subjected to self-feedback from a mirror, after a time delay, τ, and distance L. The AC component of the terminal voltage is measured using a real-time oscilliscope (40 GS/s and 12 GHz).

5.2 Random Number Generator

In the experiment, an unpackaged multi-quantum well DFB laser was utilized [40, 12] operating at 1550 nm. The laser was subjected to delayed feedback from a mirror placed at a distance L resulting in a delay time of τ. The sub-nanosecond AC component of $V(t)$ was measured using a high-speed oscilloscope (Agilent - 40 GS/s) connected to a RF probe (MB Electronics - 40 GHz), bias-T (Mini-Circuits 18 GHz), and amplifier (Microsemi - 30 GHz / 30 dB), as shown in Fig. 5.1. The resulting voltage time-series $V(t)$ were converted to binary sequences by simply retaining the least significant bit (LSB) from the output of the 8-bit analog-to-DC converter (ADC) at 40 GS/s. The LSB streams were then subjected to the NIST test for randomness [121]. In Table 5.1, we can see that this simple operation can lead to bit streams at 40 GS/s (=1 LSB $\times$ 40 GS/s), that pass the NIST suite. Furthermore, we studied the maximum number of LSBs that could be extracted and

Table 5.1: Results of the NIST test for the terminal voltage measurement using a 1 Gbit stream. For the time series here the cavity length was 30 cm, the injection current was twice threshold, and the feedback strength is chosen such that the laser is operated in coherence collapse [40]. For the tests that produce multiple P-values and proportions the worst case is shown.

STATISTICAL	P-VALUE	PROPORTION	RESULT
Frequency	0.6798	0.992	SUCCESS
Block frequency	0.6392	0.992	SUCCESS
Cumulative sums	0.7095	0.988	SUCCESS
Runs	0.1927	0.993	SUCCESS
Longest run	0.6579	0.986	SUCCESS
Rank	0.4299	0.992	SUCCESS
FFT	0.4578	0.988	SUCCESS
Nonperiodic template	0.0156	0.983	SUCCESS
Overlapping template	0.3994	0.985	SUCCESS
Universal	0.1421	0.990	SUCCESS
Approximate entropy	0.3094	0.988	SUCCESS
Random excursions	0.5070	0.986	SUCCESS
Random variant	0.3917	0.993	SUCCESS
Serial	0.5281	0.994	SUCCESS
Linear complexity	0.4376	0.985	SUCCESS

utilized. We found that the bit sequence generated by extracting 3 LSBs at 40 GS/s from the ADC with a bitwise exclusive-or operation with a delayed version of itself can also pass all the randomness tests in the NIST suite. Specifically, the 3 LSB bit sequence was subjected to the exclusive-or of itself delayed by a time not equal to the delay or a sub-multiple of the delay. This means that this still relatively simple scheme allows for a 120 Gb/s (=3 LSBs $\times$ 40 GS/s) real-time bit stream generation with minimal post-processing. The XOR operation is a typical technique used to remove the bias from bit sequences [122]. Of note, the simultaneously measured $I(t)$ does *not* pass the NIST test with a single LSB with or without the XOR. Further, we wanted to verify that the chaotic dynamics are needed in order to pass the NIST test with 1 LSB. Thus, we tested if amplified spontaneous emission noise in $I(t)$ and $V(t)$ would pass with small feedback (non-chaotic dynamics) or without feedback and they did not. The amplitude of the chaotic voltage is $\sim 2.5\ mV$ which gives a SNR of ≥ 20.

The bit streams are able to pass the NIST test without any complicated post-processing due to the nature of the voltage entropy source. In the following, we use different tests to confirm the superiority of the voltage as an entropy source. As shown in our previous work [123, 105], the distribution of $I(t)$ is known to be exponential and skewed which leads to bias. This bias can be removed using post-processing techniques and through complex experimental schemes, as demonstrated by the state-of-the-art. But, as we will show, the terminal voltage dynamics have an inherently broader distribution. In order to plot the histograms (Fig. 5.2), the DC component was removed from the time-series and normalized by the maximum. From Fig. 5.2, it is clear that the distribution given by $V(t)$ is broader than the exponential distribution of $I(t)$ which leads to significantly less bias in the voltage measurement. It is well known that $n(t)$ follows the optical intensity in the laser cavity as a result of the oscillations between photon and electron populations. This leads to the expectation that the same distribution would be obtained from both measurements. In fact, neither the magnitude of the optical field nor $n(t)$ are measured directly. Instead, we measure $I(t) = |E(t)|^2$ and $V(t) \propto \ln[n(t)]$, as shown in [120], with $E(t)$ the complex electric field. An explanation for the difference in the distributions can be explained through a change of variable extension of the best fit exponential distribution of $I(t)$ and a natural log relationship of $n(t)$ to the measured $V(t)$. Specifically, if we let $I(t)$ be a continuous random variable with probability density function $f_I(I)$, and let $V(t) = u(I)$ be an invertible function of I with inverse function $I = g(V)$, then the probability distribution of V is $f_V(V) = f_I[g(V)]|g'(V)|$. If $f_I(I)$ is exponential [123]

$$f_I(I) = \frac{1}{b} \exp\left(-\frac{|x-\mu|}{b}\right) \tag{5.1}$$

then through change of variable we obtain

$$f_V(V) = \frac{1}{b} \exp\left(-\frac{|\exp[kV(t)] - \mu|}{b}\right) \exp[kV(t)] \tag{5.2}$$

with μ the mean, and k and b distribution fitting parameters.

5.3 Voltage Chaos Characterization

Figure 5.2(b), shows the experimental fit to $f_I(I)$, and Fig. 5.2(a) demonstrates that Eq. 4.2 is a good fit of the experimental distribution from the voltage, $V(t)$. The goodness of fit was checked using the Kolmogorov-Smirnov test and underlying distributions matched Eqs. 4.1 and 4.2 with a 2% and 6% confidence, respectively. This observation confirms that the shape of the observed distribution of $v(t)$ is due to the inherent, physical, log relation between the carrier density and the voltage. Small deviations in the fit of $v(t)$ might arise from experimental error, noise in the amplifier, as well as, propagating error in the original fit of $I(t)$. Nonetheless, the measured $V(t)$ leads to a distribution that has an order of magnitude larger variance and is broader resulting from the natural log relationship between $V(t)$ and $n(t)$. The increased symmetry leads to a decrease in bias of the bit sequence [122], thus explaining the possiblility for the LSB of $v(t)$ to pass the NIST test without an additional XOR operation. The increased dispersion or variance means that the distribution is closer to an uniform distribution, leading to a better randomness source. Therefore, the exponential relationship between $n(t)$ and $v(t)$ can be considered as an inherent, physical post-processing that makes the voltage time series more amenable to RNG when compared to $I(t)$.

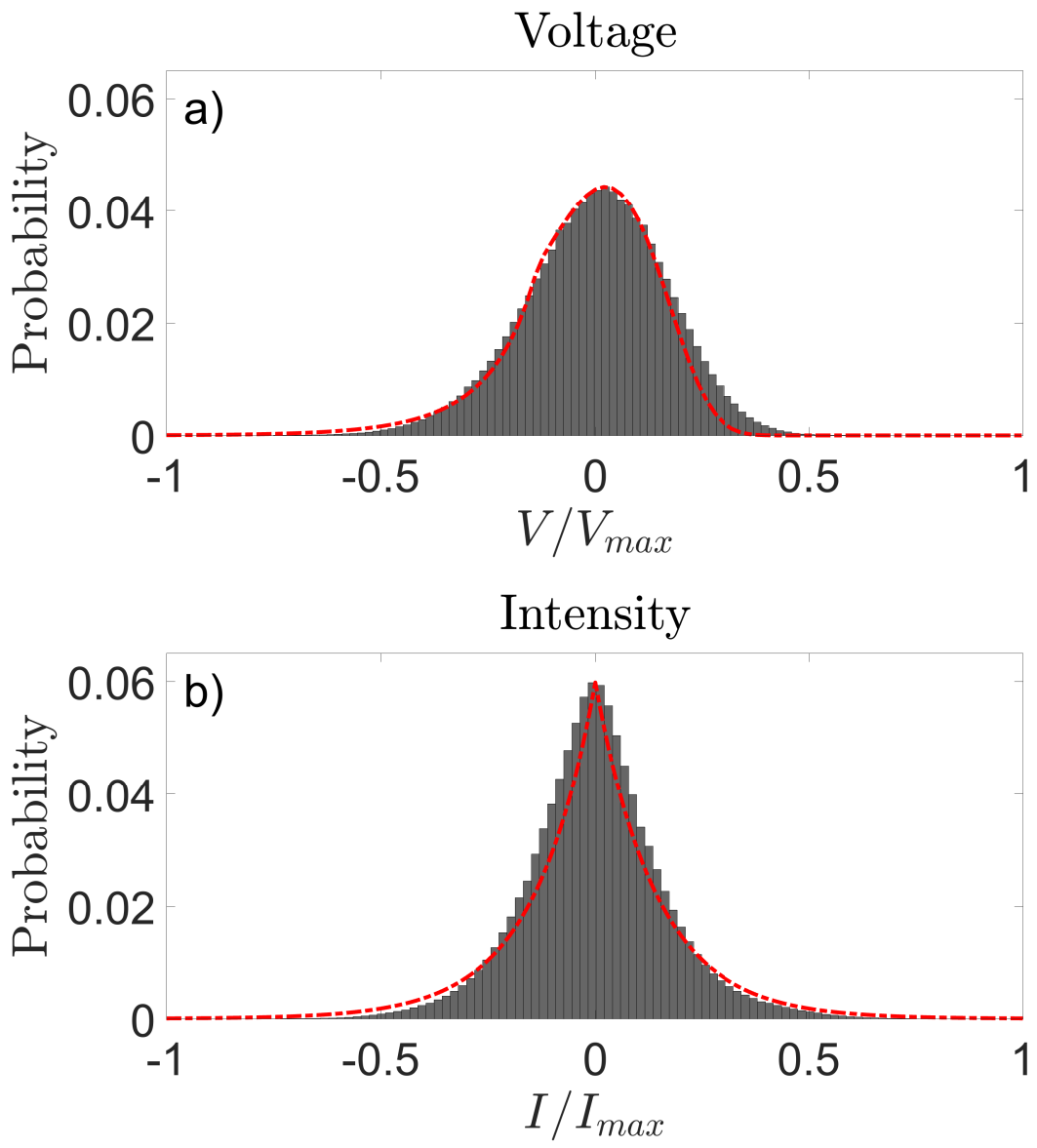

Figure 5.2: Comparison of $V(t)$ and $I(t)$ distributions from experimental data. The intensity is fit with the exponential distribution [123] and the voltage is fit with the distribution from Eq. 4.2. Both distributions were checked using the Kolmogorov-Smirnov test, and were found to match the underlying distributions with a confidence of 6% (a) and 2% (b), respectively. The voltage is broader in nature, thus, it is better suited for generating bit streams. The spreading of the distribution results from the fact the voltage is measured, which is the natural log of the carriers [120].

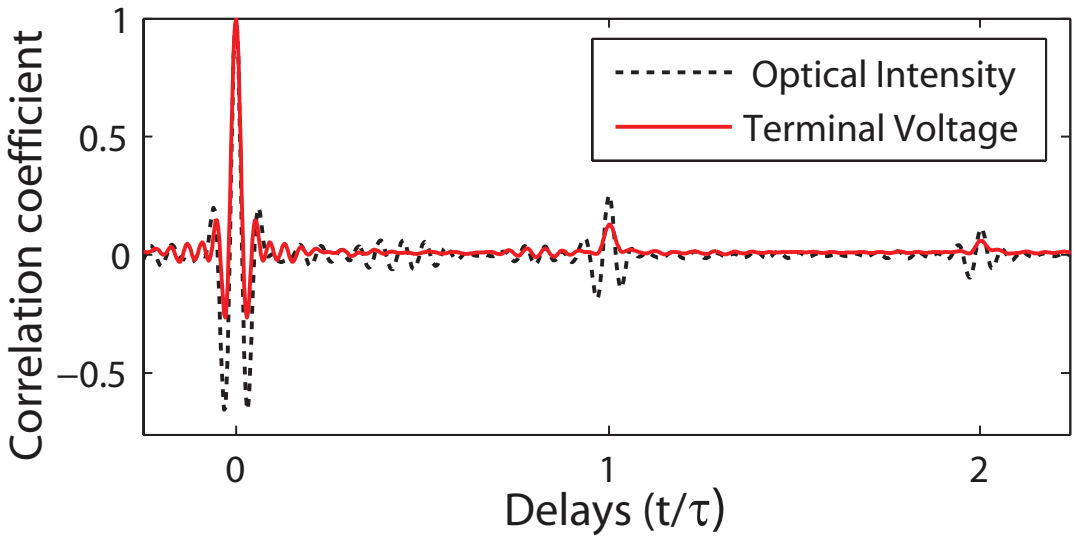

Figure 5.3: Comparison of time-delay signature in $I(t)$ and $V(t)$ chaos. There is a reduction in correlation at the delay for $V(t)$. Dashed line: $I(t)$; solid line: $V(t)$.

The second-order statistics of the randomness source also plays a role in its effectiveness. Specifically, reduction of time-delay signatures in the autocorrelation is of importance for generating effective random bit streams. The time-delay signature results from the external-cavity free-spectral range $(1/\tau)$ or the boundary condition imposed on the system by the external mirror, as shown in Fig. 5.1. Figure 5.3 represents the measured auto-covariance function. The result depicted in this Figure demonstrates that there is less correlation ($\sim$ 75%) in $V(t)$ than in $I(t)$ at τ, which further illustrates that the voltage entropy source is better suited for generating streams. More broadly, any application that requires the strong suppression or even absence of time-delay signatures [124], for example, chaos-based physical-layer secure communication [9] and chaotic lidar [125], would likely benefit from this chaotic source.

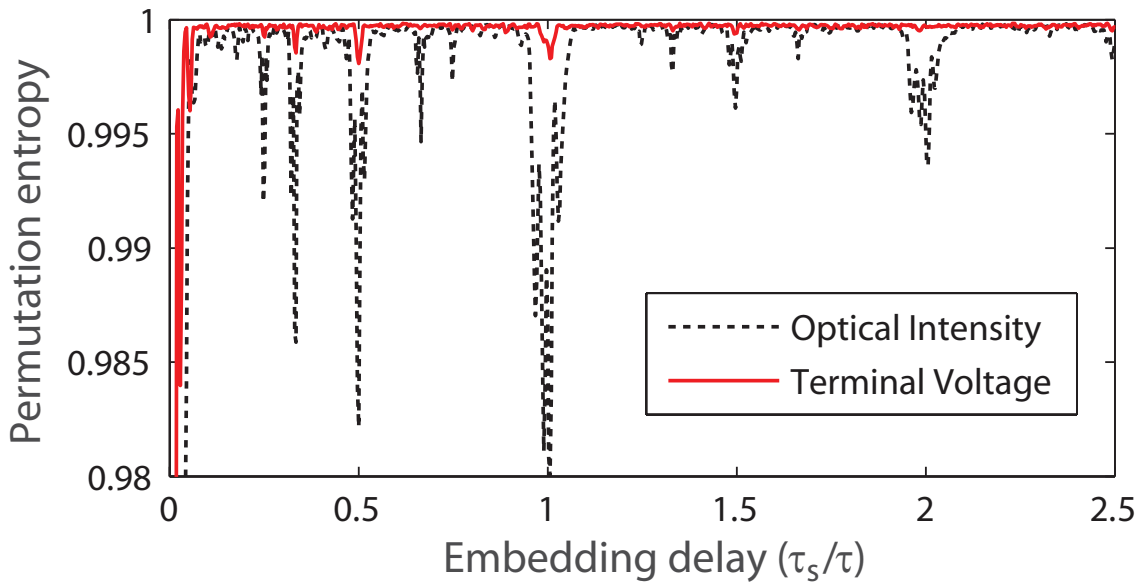

Figure 5.4: Permutation entropy estimated with an ordinal pattern length $D = 5$ as a function of the embedding delay τ_s/τ. $V(t)$. Dashed line: $I(t)$; solid line: $V(t)$

.

The entropy rate is a crucial parameter that determines the potential and the limits of a chaotic process for RNG [118, 126, 127]. To gain more insight into the advantages of using $V(t)$ over the commonly used $I(t)$, we carry out a permutation-entropy analysis. This analysis is relatively simple to compute and provides convincing information on the complexity even when computed on experimental data [114, 128, 129, 130, 131]. It has been widely used for quantifying dynamical complexity in chaotic systems since the seminal work of Bandt and Pompe [131]. In particular, it has been shown that permutation entropy evaluated at specific timescales for external-cavity lasers can recover important features characterized by Kolmogorov-Sinai entropy rate, and is consistent with the notion of weak and strong chaos [128, 129]. Here we compare the results of permutation entropy estimated from the two physical entropy sources, *i.e.*, $I(t)$ and $V(t)$ in chaotic lasers. Of importance, the entropy calculations were performed on the raw data extracted by the ADC without

any post-processing, as suggested in [126]. Therefore, the physical entropy rate from the two different sources is compared, and deterministic post-processing is removed from the entropy calculation [126].

For the computation of permutation entropy, we use the ordinal pattern length $D = 5$ and assume the embedding delay τ_s as the control parameter, in order to obtain a measure of the dynamical complexity over multiple timescales. The results are shown in Fig. 5.4, clearly indicating that $V(t)$ has larger values of permutation entropy than $I(t)$ computed at the embedding delay τ_s matching harmonics and subharmonics of delay time τ. Accordingly, the entropy estimation in conjunction with results in Figs. 5.2 and 5.3 further confirm that the proposed terminal voltage $V(t)$ is a promising physical entropy source for fast random number generation, and thus providing a physical explanation of the main results in this work.

5.4 Conclusion

The results are robust to experimental conditions if the dynamics are chaotic (coherence collapse). Specifically, L was varied from 30-60 cm, the injection current from 1.5-2.5 times threshold, and the feedback within 10 % and the bit streams generated from the measured chaotic voltage time series passed the NIST test. Contrarily, those extracted from the simultaneously measured chaotic optical intensity and spontaneous emission noise time series did not pass the NIST test with the same post-processing.

We have demonstrated that the simple terminal voltage measurement of a laser subjected to optical feedback from a mirror can be utilized to generate random bit streams at 40-120 Gb/s thus circumventing the need for optical-to-electrical conversion. Such an electronic entropy source is therefore envisaged to be more easily integrated with high-speed computers. Our results demonstrate that the chaotic terminal voltage is a superior entropy source when compared to optical chaos, benefiting from a broader distribution, a smaller delay signature, and a larger permutation entropy at the delay. More importantly,

the scheme demonstrated here is significantly simpler to implement by only requiring a laser, mirror, ADC, and minimal or no post-processing; depending on the speed of the ADC, it is possible to generate random numbers at tens of Gb/s while remaining robust to variations in various experimental parameters. Also, it represents a direct electronic source of chaos that is being utilized for generating these bit streams without optical to electrical conversion. Thus, the system could be implemented as a discrete package into an electronic application that directly needs random number streams at very fast rates. Moreover, any application which requires a reduction in time-delay signature and larger entropy, such as chaos-based secure communications and chaotic lidar, could also benefit from these voltage dynamics.

CHAPTER 6
THE LASER AS A PHOTODIODE

6.1 Laser Sensing

Optical feedback into a LD can induce profound modification to its light-emission properties, and has thus attracted considerable attention over the past four decades starting with applications in velocimeters and position sensors [132, 133]. These devices exploit the beating within the cavity at the Doppler frequency of returned light with the light emitted by the LD. The output intensity modulated at the Doppler frequency is measured by a PD. But other properties may also be modified by the feedback. In Ref. [134], a change in self-modulation frequency in a periodic regime was detected via the frequency of the LD terminal voltage V. Also, the voltage V can be used to probe the carrier dynamics in the active region of a LD [38, 120, 40].

We now focus on direct antecedents of our work. Seko *et al.* [135] demonstrated "self quenching" of a LD in front of which a mirror is placed or is absent, *i.e.*, they observed a change in the intensity emitted at the back facet of the LD. They further demonstrated a primitive optical data reader based on a rotating disc with cutouts placed in the external cavity [136]. Ukita *et al.* fabricated a laser device based on an extremely short strong-feedback external cavity laser that can be used for optical disk read out. The system uses self-mixing properties, and measures the change in light properties using an integrated PD [137], quite distinct from our approach which entirely dispenses with the PD. In Ref. [135] it was shown that the change in feedback can be sensed via the LD terminal voltage V under constant-current J operation. While it was suggested in [135] to monitor V as the optical-data readout parameter, the experiment does not appear to have been carried out.

Here we show V can be used to measure the change in reflectivity of an object because

when light is re-injected into a LD, a drop in the previously stationary DC voltage occurs, as demonstrated in [38, 120]. Thus, we can scan an object with a LD and measure the change in the DC terminal voltage V. Previously, two-dimensional optical scanning and imaging based on the measurement of the voltage change induced by optical feedback was shown in Ref. [138]. The physical origin of this effect is the enhancement in stimulated emission, which results in a reduction of inversion because the voltage is proportional to the changes in the quasi-Fermi-level difference [120]. Essentially, the DC level observed is proportional to the bias current from the current controller. Therefore, the DC level is defined as the measured voltage averaged over a timescale that is short compared with the duration of an optical bit, but long compared to any intrinsic dynamics of the laser diode with constant optical feedback. The DC level only varies (without a spinning CD) with the fluctuations associated with the current controller. These factors together are on the order of μVs. Thus, large changes in the level of the DC voltage ($\sim 60\ mV$) are due to the effect we are exploiting.

Specifically, we make the following claims. (1) We read bits from a CD-ROM under realistic dynamical conditions via changes in the LD terminal voltage due to changes in the feedback optical intensity upon reflection from the CD-ROM. (2) The signals produced are compatible with the practical application of this effect in the context we focus on. (3) The feedback mechanism is temporally incoherent, thus making the approach robust against mechanical vibrations, deflections, or small misalignments. Since the effect is temporally incoherent, it is distinct from that exploited for conventional self-mixing interferometry.

A LD package from a commercial CD-ROM drive was used in order to show the ability to read optical media and the simplicity of the approach. CD-ROM drives use a LD that emits light ($\lambda = 780$ nm) that strikes the medium and is reflected or not depending on where the light strikes the CD-ROM (see below). The beam is then, if reflected, sent back into the laser package where there is typically a beam splitter (BS) that routes the light to a PD external to the laser. In our experiment, the BS was removed in order to route the

reflected light back onto the LD (Fig. 6.1). This allowed for the imaging of the optical disk using as the contrast mechanism the variations in reflectivity of the optical disk or the encoded bits. To emphasize, we monitor *only* the DC component of the voltage across the LD and *not* dynamic components of the voltage.

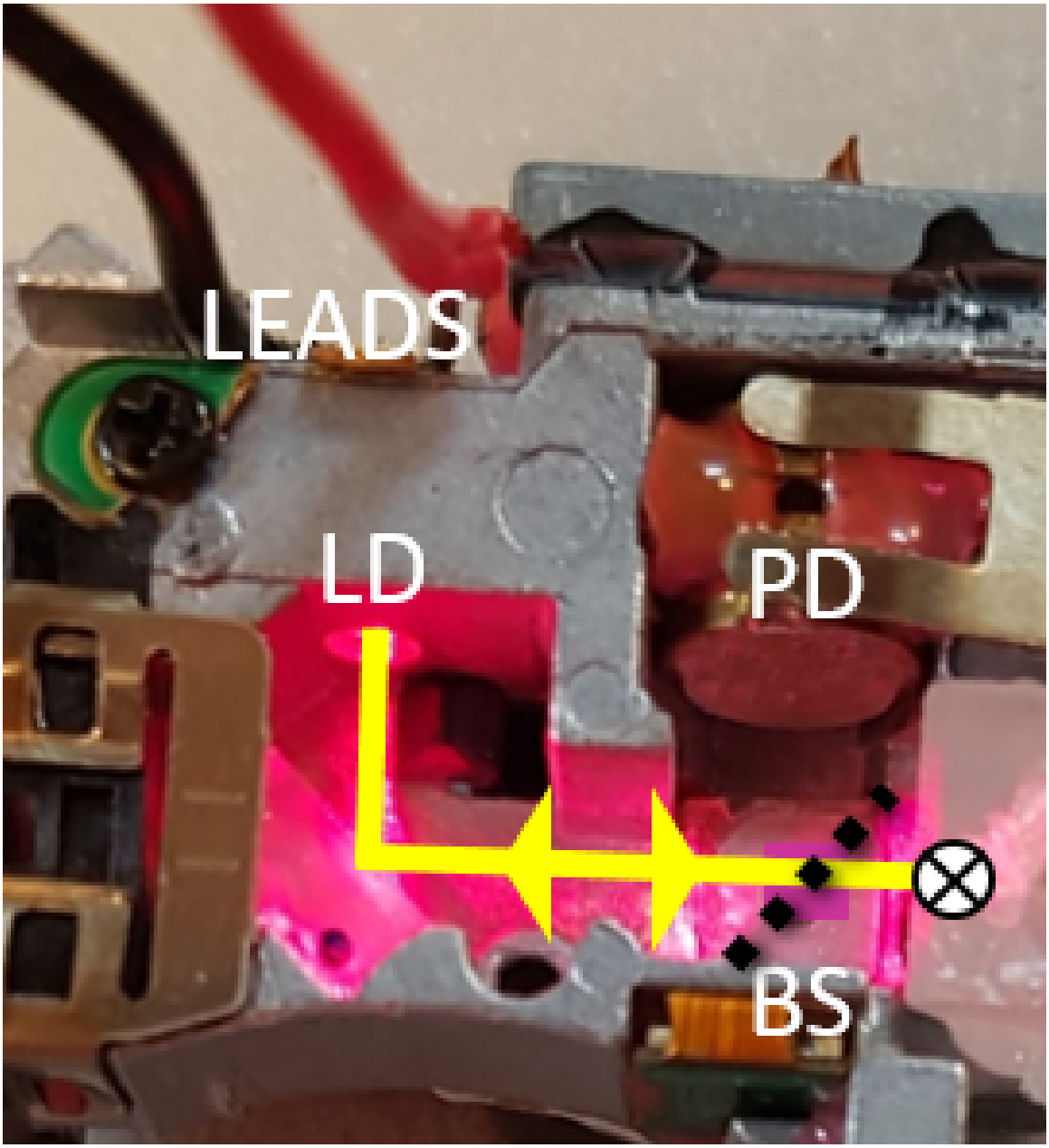

Figure 6.1: A close-up of the LD package. BS and the dashed line represent the removed beam splitter. LD and PD stand for laser diode and photodiode respectively. The shown beam path leaves the LD and strikes a mirror at a 45 degree angle and goes to another mirror which directs the beam through the page (marked by the symbol x) and onto the CD-ROM. The shown leads are soldered onto the LD in order to provide power and a means for measuring V.

6.2 Laser Imaging and Detection

To demonstrate the basic principal first, a high-reflectivity mirror (Newport 10Z40DM.8) and digital multimeter were used to send the light back onto the LD and measure V, respectively. Next, a blazed diffraction grating with a gold coating designed for the near-infrared with a blaze angle, θ = 28, and a grating pitch, $\Lambda = 1.6$ μm was scanned using the LD from the CD-ROM drive (Samsung SM-308). Specifically, the LD package was rastered across the grating using an electric nano-positioning actuator (Newport NanoPZ) while simultaneously measuring the value of V with a digital multimeter. This experimental setup can be seen in Fig. 6.2.

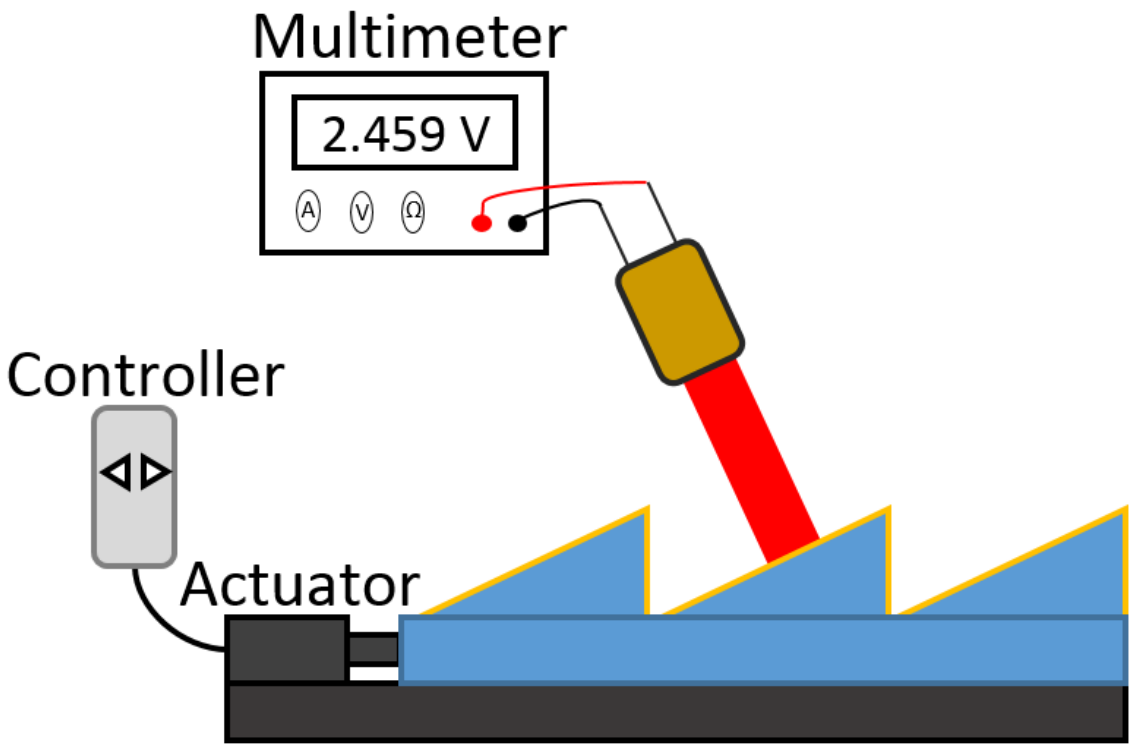

Figure 6.2: The laser is incident on a gold coated blazed diffraction grating with pitch $\Lambda = 1.6$ μm. A nanopositioning actuator is used to accurately raster the grating under the LD while a digital multimeter measures V.

Bits were then read from the CD-ROM by placing the modified LD package seen in Fig. 6.1 back into the CD-ROM drive, and placing a CD-ROM into the tray. A DC motor was used to spin the disc using a voltage source to control the rotational speed of the motor, as seen in Fig. 6.3. The rotational speed was measured by placing a line on the disk and using a fast video camera that films at 240 fps. By counting the number of frames it takes for the disk to rotate one time the linear relationship between voltage and RPMs was plotted. While the CD was spinning, V was measured using an oscilloscope (Agilent DS080804B) with a bandwidth of 12 GHz.

We estimated the coherence length in order to determine whether the feedback was temporally coherent or not. A measurement using an optical spectrum analyzer showed a coherence length of around 8 mm as confirmed by [139]. Since the round-trip length of the external cavity is 3 cm, the feedback is incoherent when it returns to the LD. It has been shown experimentally and numerically that incoherent feedback in systems has a direct affect on the carrier number and thus the terminal voltage [140, 141]. As we discuss below, our approach therefore is distinct from self-mixing interferometry and thus is expected to exhibit superior mechanical stability.

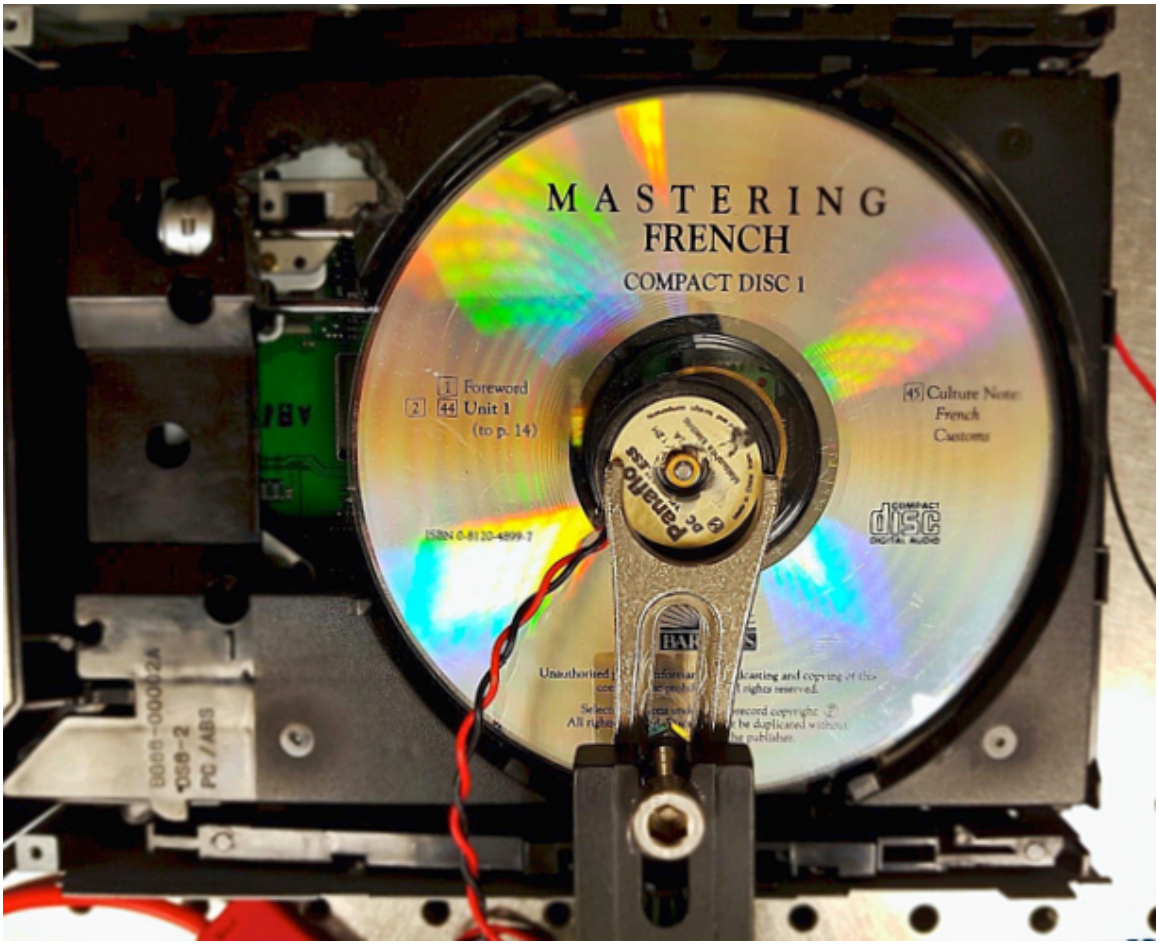

Figure 6.3: A CD-ROM in the modified CD drive. The motor and holder are both visible, and the motor is controlled by a voltage source. The leads from the LD can be seen on the right side and go to an oscilloscope.

When the mirror was aligned, a reduction in V of 0.078 V was observed (Table I). The drop in V suggests that amplification would not be needed and established that feedback could be achieved. The diffraction grating was scanned using the LD, which was positioned such that maximum reflectivity was obtained from the diffraction grating and with an incidence angle equal to the blaze angle. As seen in Table I, the measured value of the voltage reduction for the diffraction grating was smaller than that of the mirror but still sufficiently large to be measured without amplification. We changed the position of the

diffraction grating in steps of 200 nm and the resulting value of V as a function of position is shown in Fig. 6.4, as reported in [142].

Table 6.1: V in the presence or absence of two reflective objects, a mirror and a diffraction grating. The value corresponding to feedback for the diffraction grating is when the laser spot is centered over a blazed surface giving maximum feedback.

	Feedback	No feedback
Mirror	2.401 V	2.479 V
Diffraction Grating	2.459 V	2.479 V

The periodicity in Fig. 6.4 is due to the periodic nature of blazed gratings. When the light is incident perpendicular to a blaze, as seen in Figure 6.5, feedback is achieved and a drop in the voltage is seen. When the light is at the drop off from one blaze to the next there is scattering and interference. The destructive interference occurs due to a phase shift for small values of θ where the phase difference is $\phi = 4\pi\Lambda\theta/\lambda$. For our experiment, the phase difference is $\phi \approx 5\pi$, which leads to nearly perfect destructive interference. We also note that we are able to see changes on an even smaller scale than 1.6 μm. Indeed, Fig. 6.4 shows that we are able to see variations in V on a scale as small as 0.2 μm, which is significantly smaller than any distance one would need to detect on an optical disk.

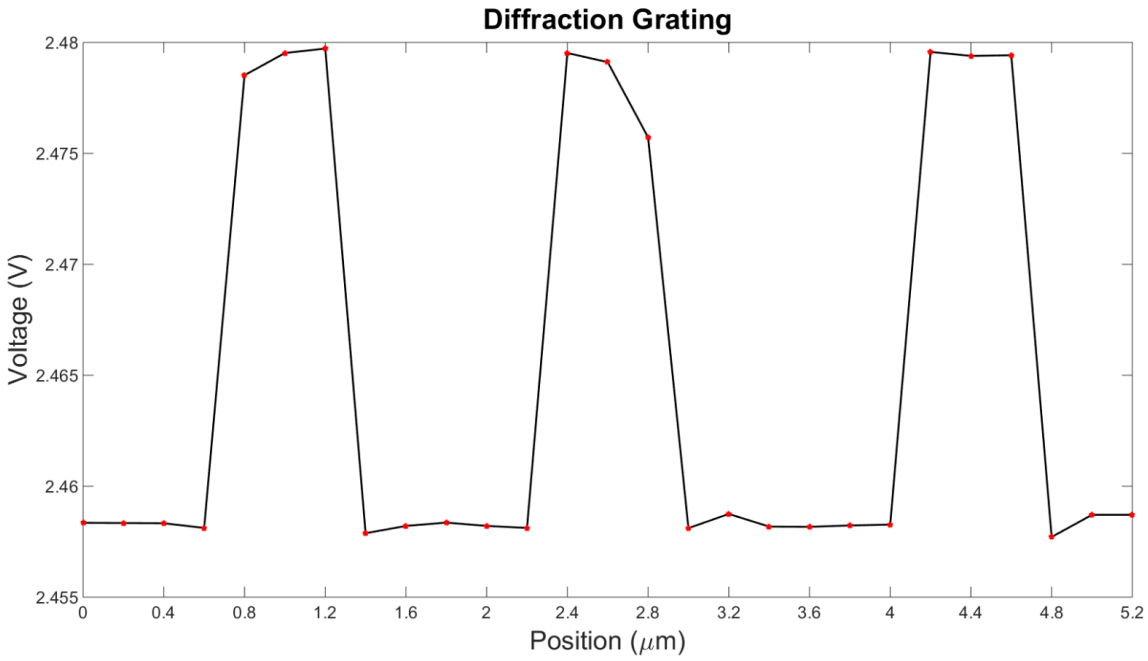

Figure 6.4: V changes periodically with the same period as the grating, 1.6 μm.

We next detected bits on a spinning CD-ROM. As can be seen in Fig. 6.6, bit changes are seen by monitoring V. Changes in the value of V occur due to the modulation in reflectivity given by the CD-ROM as it spins. When light is incident on the change between a land to a pit or *vice versa*, there is near perfect destructive interference leading to negligible feedback on the laser and an increase in V, as illustrated in Fig.6.7.

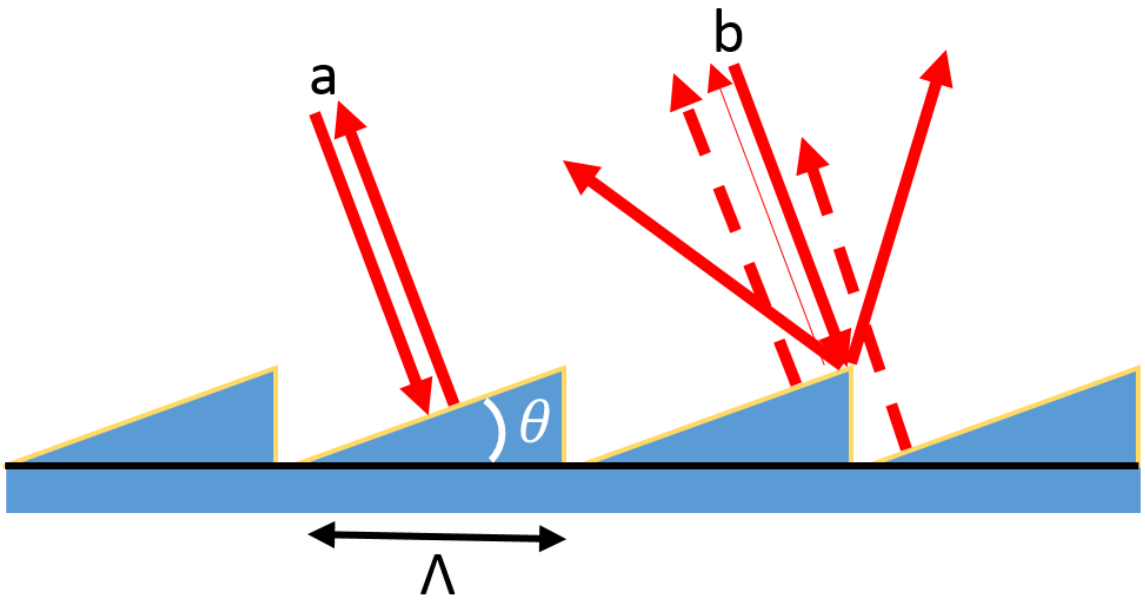

Figure 6.5: Schematic cross section of the blazed grating, which has a blaze angle, $\theta = 28$ degrees, and grating pitch, $\Lambda = 1.6$ μm. For the rays incident at point a, there is a strong reflection leading to substantial feedback on the LD. Which is detected as a decrease in V. However, for light incident at point b the reflection is weak due to scattering (solid) and destructive interference (dashed), leading to a smaller optical feedback and an increase in V.

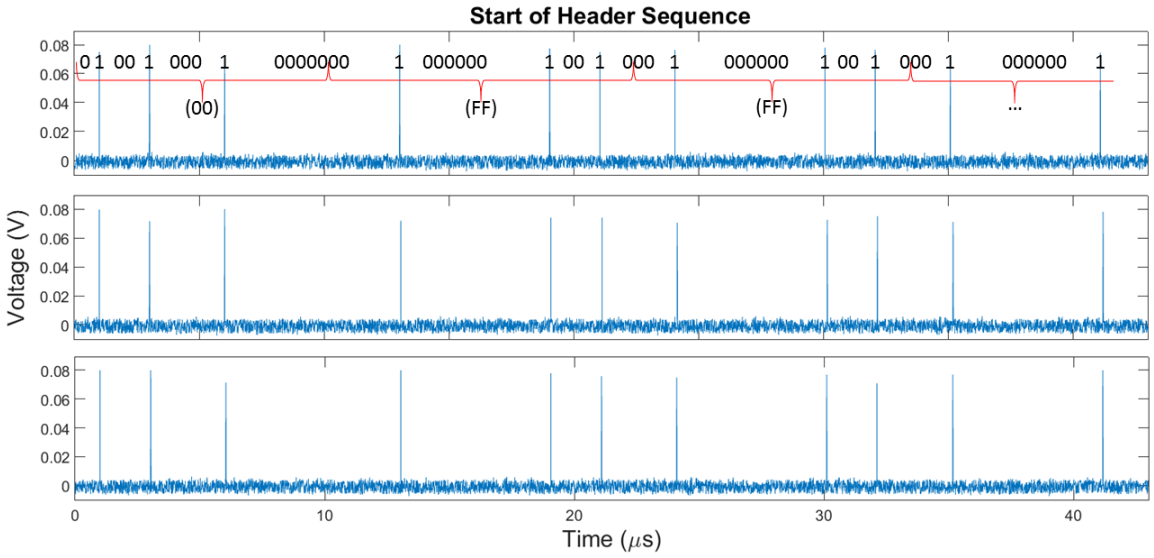

Figure 6.6: V as a function of time with a spinning CD-ROM (3 different readings). The beginning portion of a header is shown. The total header consists of 12 bytes (00 FF FF FF FF FF FF FF FF FF FF 00). After the 8 to 14 bit conversion, 00 becomes (01001000100000) and FF becomes (00100000010010) [143]. A one is encoded as a change in height on the disc.

To further confirm that actual bits were seen it was necessary to read and interpret them. CD-ROMs use an 8 to 14 bit channel conversion and have a sync header sequence consisting of 12 bytes (96 bits) every 2352 bytes [143]. Also, the 8 to 14 bit channel conversion is setup such that no other data sequence is possible that would have the same bit sequence as a header. It is known that every 1.51 cm of rotational distance on the disk a sync header should be found. The raw data from the oscilloscope was searched for headers, and it was experimentally determined that a header was occurring every $\sim 1.59 \pm 0.1$ cm of rotational distance. The error in the estimation is due to the imperfect knowledge of the rotational speed of the disk and is within the estimating range. The measurement of the bits was repeated 10 times for verification with consistent results. A statistical analysis of the chance

of this header sequence occurring randomly one time reveals it is a $1/10^{28}$ chance. Experimentally the correction header sequence was observed two times and was separated by approximately the same distance as theoretically calculated. Further, the separations between ones are exactly proportional to the number of zeros within the error of the sampling rate. The previous observations confirm unambiguously our ability to detect the bits on a CD-ROM. Also of note, using the DC motor we were able to achieve speeds at the level of an actual CD-ROM drive.

We have determined the SNR for our system to be ~ 9 dB. In comparison, the SNR for the PD is known to be poor without additional pre-processing including a current amplifier, a filter, and a transimpedance amplifier. After the complex circuitry, the PD has a SNR of ~ 47 dB [144]. Although the PD may have a better SNR after circuitry, in a binary system if the value of a one is significantly different than a zero, the system will work. A qualitative analysis of the waveforms in Fig. 6.6 shows that we are able to distinguish between binary 0's and 1's with a simple thresholding and without any added circuitry.

A second consideration is power. The difference in electrical power delivered by the terminal voltage probes is given by the product of the voltage difference between 0 and 1 (~ 0.08 V from our measurements suggesting that this could be implemented in applications without amplification) and the drive current 50 mA. The resulting power is ~ 4 mW. This power level is larger than that produced by the PD in a conventional CD-ROM drive with a change in power of $\sim 10 - 100$ μW.

We also comment on the temporal coherence of the feedback due to the relatively long external-cavity round-trip time and the relatively short coherence time of the LD. (We emphasize that the *spatial* coherence across the laser beam is high and important as this provides the contrast mechanism.) The temporal incoherence implies that the population principle is insensitive to variations in the external-cavity length on the order of the optical wavelength. The same is *not* the case for a coherent system, which is susceptible to vibration. Indeed, in our demonstration, no additional mechanical stabilization or alignment,

beyond the stock CD-ROM drive housing, was provided.

In traditional CD-ROM technology, an array of photodiodes is used. There are different topologies between varying manufacturers, but in all of the configurations that we are aware, one or more PDs are utilized for measuring the light being fed back by the CD for data, and other PDs are used for tracking and focusing [144]. Thus, a new array would need to be fabricated with one LD and PDs on each side of the laser. These PDs would be utilized for tracking and focusing just as is currently done in CD systems. But, nonetheless the sensing portion would still be greatly simplified and improved by utilizing the approach in this article.

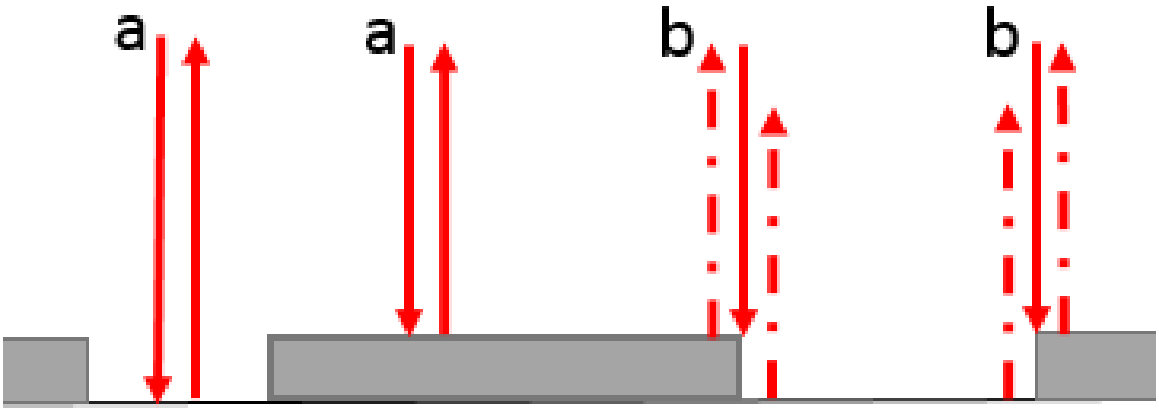

Figure 6.7: Schematic cross section of a CD-ROM disc. When the light is incident at a surface other than an edge the light is reflected back into the LD leading to feedback and a drop in V (rays labeled a). When light is incident on a transition from a land to a pit the light interferes destructively, because the distance between the land and pit is $\lambda/4$ corresponding to a phase shift equal to π, as seen by the rays labeled b.

6.3 Conclusion

We have shown that we are able to image variations in the surface of reflective objects by monitoring the DC value of the laser voltage V. This has allowed us to read the bits on a

CD-ROM simply using a laser diode and without a photodiode. The significant variation in between ones and zeros seen in our waveforms imply this can be integrated in a system without amplification. Our approach also simplifies system architecture by eliminating the beam splitter, photodiode, and the circuitry associated with the photodiode. In addition to optical-disc reading, applications where the PD is difficult to accommodate due to geometrical constraints or in other portions of the spectrum where the detector is expensive, such as in the terahertz range, may benefit from the approach developed here.

CHAPTER 7
CONCLUSION

In this thesis, we have reëvaluated previous experiments and identified a universal route to chaos in external cavity lasers by utilizing comprehensive, state-of-the-art experiments which probe all three dynamic variables in real-time, for the first time after 50 years of study. Further, the techniques and analysis employed here can be utilized to reëvaluate these systems for other cavity length and pump conditions in order to further understand these systems and exploit them for applications.

Understanding the route to chaos is important because these systems have been exploited for many applications in information science. Therefore by utilizing the newfound knowledge about the dynamic regimes and how the transition between the different regimes occur on the route to chaos, we have been able to optimize and re-define three different applications. For neuromorphic computing, we have been able to identify the optimal operating point and have demonstrated record speeds of 71 million digits per second with an accuracy of 99.99%.

For random number generation, we have identified and characterized a novel entropy source (chaotic terminal voltage dynamics) which is simpler to implement and is an inherently superior entropy source when compared to the current state-of-the-art. This entropy source allows for the generation of 40-120 GS/s random bit streams with zero or minimal post-processing. Further, it obviates the need for optical-to-electrical conversion by utilizing an electronic entropy source directly.

A simple, stable, X-band tunable microwave oscillator has been demonstrated. The oscillator, which is stabilized utilizing self-feedback and careful locking of the system's dynamic frequencies, is tuned with simple adjustment of the current. Further, the oscillator stability is characterized by sub-ps jitter and is competitive in terms of stability and tunable

to the current state-of-the-art while being relatively simple. Our design is only requires a single laser diode, mirror, photodiode, attenuator and interconnects. Further, it does not require multiple lasers, external modulation sources, and/or exotic components such as the case with the current state-of-the-art.

Finally, a laser diode was demonstrated to be able to act as its own photodiode. This was demonstrated using CD-ROM technology,specifically, a CD-ROM was spun and the bits were read and interpreted by detecting changes in the terminal voltage as a function of time caused by changes in optical feedback (variations in reflectivity on the surface of the disc). Such technology is of interest for reduce manufacturing costs by simplifying designs, as well as, in regions where photodiodes are unattainable due to cost or lack of commercial availability.

REFERENCES

[1] S. H. Strogatz, *Nonlinear dynamics and chaos: with applications to physics, biology, chemistry, and engineering*. Westview press, 2014.

[2] K. T. Alligood, T. D. Sauer, and J. A. Yorke, *Chaos*. Springer, 1996.

[3] J. Ohtsubo, *Semiconductor lasers: stability, instability and chaos*. Springer, 2012, vol. 111.

[4] M. C. Soriano, J. García-Ojalvo, C. R. Mirasso, and I. Fischer, "Complex photonics: Dynamics and applications of delay-coupled semiconductors lasers," *Reviews of Modern Physics*, vol. 85, no. 1, p. 421, 2013.

[5] A Bogatov, P Eliseev, L Ivanov, A Logginov, M Manko, and K Senatorov, "Study of the single-mode injection laser," *IEEE J. Quantum. Electron.*, vol. 9, no. 2, pp. 392–394, 1973.

[6] D. Brunner, M. C. Soriano, C. R. Mirasso, and I. Fischer, "Parallel photonic information processing at gigabyte per second data rates using transient states," *Nat Commun*, vol. 4, p. 1364, 2013.

[7] D Rontani, D Choi, C.-Y. Chang, A Locquet, and D.S. Citrin, "Compressive sensing with optical chaos," *Sci. Rep.*, vol. 6, p. 35 206, 2016.

[8] A. Uchida, K. Amano, M. Inoue, K. Hirano, S. Naito, H. Someya, I. Oowada, T. Kurashige, M. Shiki, S. Yoshimori, *et al.*, "Fast physical random bit generation with chaotic semiconductor lasers," *Nat. Photonics*, vol. 2, no. 12, pp. 728–732, 2008.

[9] A. Argyris, D. Syvridis, L. Larger, V. Annovazzi-Lodi, P. Colet, I. Fischer, J. Garcia-Ojalvo, C. R. Mirasso, L. Pesquera, and K. A. Shore, "Chaos-based communications at high bit rates using commercial fibre-optic links," *Nature*, vol. 438, no. 7066, pp. 343–346, 2005.

[10] D. Rontani, A. Locquet, M. Sciamanna, D.S. Citrin, and S. Ortin, "Time-delay identification in a chaotic semiconductor laser with optical feedback: A dynamical point of view," *IEEE J. Quantum. Electron.*, vol. 45, no. 7, pp. 879–1891, 2009.

[11] A Locquet, C Masoller, and C. Mirasso, "Synchronization regimes of optical-feedback-induced chaos in unidirectionally coupled semiconductor lasers," *Physical Review E*, vol. 65, no. 5, p. 056 205, 2002.

[12] C.-Y. Chang, M. J. Wishon, D. Choi, J. Dong, K. Merghem, A. Ramdane, F. Lelarge, A. Martinez, A. Locquet, and D.S. Citrin, "Tunable x-band optoelectronic oscillators based on external-cavity semiconductor lasers," *IEEE J. Quantum. Electron.*, vol. 53, no. 3, pp. 1–6, 2017.

[13] R Tkach and A. Chraplyvy, "Regimes of feedback effects in 1.5-um distributed feedback lasers," *J Lightwave Technol*, vol. 4, no. 11, pp. 1655–1661, 1986.

[14] I Fischer, G. Van Tartwijk, A. Levine, W Elsässer, E Göbel, and D Lenstra, "Fast pulsing and chaotic itinerancy with a drift in the coherence collapse of semiconductor lasers," *Phys Rev Lett*, vol. 76, no. 2, p. 220, 1996.

[15] G. Van Tartwijk, A. Levine, and D Lenstra, "Sisyphus effect in semiconductor lasers with optical feedback," *IEEE J. Sel. Topics in Quantum Electron.*, vol. 1, no. 2, pp. 466–472, 1995.

[16] D. Brunner, M. C. Soriano, X. Porte, and I. Fischer, "Experimental phase-space tomography of semiconductor laser dynamics," *Phys Rev Lett*, vol. 115, no. 5, p. 053 901, 2015.

[17] X. Porte, M. C. Soriano, and I. Fischer, "Similarity properties in the dynamics of delayed-feedback semiconductor lasers," *Physical Review A*, vol. 89, no. 2, p. 023 822, 2014.

[18] R. Lang and K. Kobayashi, "External optical feedback effects on semiconductor injection laser properties," *IEEE J Quantum Electron*, vol. 16, no. 3, pp. 347–355, 1980.

[19] J Mørk, J Mark, and B Tromborg, "Route to chaos and competition between relaxation oscillations for a semiconductor laser with optical feedback," *Phys Rev Lett*, vol. 65, no. 16, p. 1999, 1990.

[20] J. Ye, H. Li, and J. G. McInerney, "Period-doubling route to chaos in a semiconductor laser with weak optical feedback," *Phys. Rev. A*, vol. 47, no. 3, p. 2249, 1993.

[21] A. Hohl and A. Gavrielides, "Bifurcation cascade in a semiconductor laser subject to optical feedback," *Phys Rev Lett*, vol. 82, no. 6, p. 1148, 1999.

[22] B. Kim, N. Li, A Locquet, and D.S. Citrin, "Experimental bifurcation-cascade diagram of an external-cavity semiconductor laser," *Opt. Express*, vol. 22, no. 3, pp. 2348–2357, 2014.

[23] B. Kim, A. Locquet, N. Li, D. Choi, and D. Citrin, "Bifurcation-cascade diagrams of an external-cavity semiconductor laser: Experiment and theory," *IEEE Journal of Quantum Electronics*, vol. 50, no. 12, pp. 965–972, 2014.

[24] T. Mukai and K. Otsuka, "New route to optical chaos: Successive-subharmonic-oscil-lation cascade in a semiconductor laser coupled to an external cavity," *Phys Rev Lett*, vol. 55, no. 17, p. 1711, 1985.

[25] G. C. Dente, P. S. Durkin, K. A. Wilson, and C. E. Moeller, "Chaos in the coherence collapse of semiconductor lasers," *IEEE J Quantum Electron*, vol. 24, no. 12, pp. 2441–2447, 1988.

[26] D.-S. Seo, J.-D. Park, J. G. Mcinerney, and M. Osinski, "Multiple feedback effects in asymmetric external cavity semiconductor lasers," *IEEE J. Quantum. Electron.*, vol. 25, no. 11, pp. 2229–2238, 1989.

[27] J.-D. Park, D.-S. Seo, and J. G. McInerney, "Self-pulsations in strongly coupled asymmetric external cavity semiconductor lasers," *IEEE J. Quantum. Electron.*, vol. 26, no. 8, pp. 1353–1362, 1990.

[28] D. Pieroux, T. Erneux, B. Haegeman, K. Engelborghs, and D. Roose, "Bridges of periodic solutions and tori in semiconductor lasers subject to delay," *Phys. Rev. Lett.*, vol. 87, no. 19, p. 193 901, 2001.

[29] J. Mork, B. Tromborg, and J. Mark, "Chaos in semiconductor lasers with optical feedback: Theory and experiment," *IEEE J. Quantum. Electron.*, vol. 28, no. 1, pp. 93–108, 1992.

[30] C Henry and R Kazarinov, "Instability of semiconductor lasers due to optical feedback from distant reflectors," *IEEE J. Quantum. Electron.*, vol. 22, no. 2, pp. 294–301, 1986.

[31] N. Schunk and K. Petermann, "Numerical analysis of the feedback regimes for a single-mode semiconductor laser with external feedback," *IEEE J. Quantum. Electron.*, vol. 24, no. 7, pp. 1242–1247, 1988.

[32] A. Ritter and H. Haug, "Theory of laser diodes with weak optical feedback. i. small-signal analysis and side-mode spectra," *J. Opt. Soc. Am.*, vol. 10, no. 1, pp. 130–144, 1993.

[33] C Masoller and N. Abraham, "Stability and dynamical properties of the coexisting attractors of an external-cavity semiconductor laser," *Phys. Rev. A*, vol. 57, no. 2, p. 1313, 1998.

[34] G Acket, D. Lenstra, A Den Boef, and B Verbeek, "The influence of feedback intensity on longitudinal mode properties and optical noise in index-guided semiconductor lasers," *IEEE J. Quantum. Electron.*, vol. 20, no. 10, pp. 1163–1169, 1984.

[35] T. Sano, "Antimode dynamics and chaotic itinerancy in the coherence collapse of semiconductor lasers with optical feedback," *Phys. Rev. A*, vol. 50, no. 3, p. 2719, 1994.

[36] A. Levine, G. Van Tartwijk, D. Lenstra, and T. Erneux, "Diode lasers with optical feedback: Stability of the maximum gain mode," *Phys. Rev. A*, vol. 52, no. 5, R3436, 1995.

[37] D. Brunner, X. Porte, M. C. Soriano, and I. Fischer, "Real-time frequency dynamics and high-resolution spectra of a semiconductor laser with delayed feedback," *Sci Rep*, vol. 2, p. 732, 2012.

[38] R. Kazarinov and R. Suris, "Heterodyne reception of light by an injection laser," *Zhurnal Eksperimental'noi i Teoreticheskoi Fiziki*, vol. 66, pp. 1067–1078, 1974.

[39] B. Kim, A. Locquet, D. Choi, and D.S. Citrin, "Experimental route to chaos of an external-cavity semiconductor laser," *Phys. Rev. A*, vol. 91, no. 6, p. 061 802, 2015.

[40] C.-Y. Chang, D. Choi, A Locquet, M. J. Wishon, K Merghem, A. Ramdane, F. Lelarge, A Martinez, and D. Citrin, "A multi-ghz chaotic optoelectronic oscillator based on laser terminal voltage," *Applied Physics Letters*, vol. 108, no. 19, p. 191 109, 2016.

[41] A Locquet, B. Kim, D. Choi, N. Li, and D.S. Citrin, "Initial-state dependence of the route to chaos of an external-cavity laser," *Phys. Rev. A*, vol. 95, no. 2, p. 023 801, 2017.

[42] P. Alsing, V. Kovanis, A. Gavrielides, and T. Erneux, "Lang and kobayashi phase equation," *Phys. Rev. A*, vol. 53, no. 6, p. 4429, 1996.

[43] B. Tykalewicz, D. Goulding, S. P. Hegarty, G. Huyet, T. Erneux, B. Kelleher, and E. A. Viktorov, "Emergence of resonant mode-locking via delayed feedback in quantum dot semiconductor lasers," *Opt. Express*, vol. 24, no. 4, pp. 4239–4246, 2016.

[44] H. Markram, E. Muller, S. Ramaswamy, M. W. Reimann, M. Abdellah, C. A. Sanchez, A. Ailamaki, L. Alonso-Nanclares, N. Antille, S. Arsever, *et al.*, "Reconstruction and simulation of neocortical microcircuitry," *Cell*, vol. 163, no. 2, pp. 456–492, 2015.

[45] H. Jaeger and H. Haas, "Harnessing nonlinearity: Predicting chaotic systems and saving energy in wireless communication," *Science*, vol. 304, no. 5667, pp. 78–80, 2004.

[46] J. Hasler and H. B. Marr, "Finding a roadmap to achieve large neuromorphic hardware systems," *Frontiers in neuroscience*, vol. 7, p. 118, 2013.

[47] Y. LeCun, Y. Bengio, and G. Hinton, "Deep learning," *Nature*, vol. 521, no. 7553, pp. 436–444, 2015.

[48] H. Jaeger, "The "echo state" approach to analysing and training recurrent neural networks-with an erratum note," *Bonn, Germany: German National Research Center for Information Technology GMD Technical Report*, vol. 148, p. 34, 2001.

[49] W. Maass, T. Natschläger, and H. Markram, "Real-time computing without stable states: A new framework for neural computation based on perturbations," *Neural computation*, vol. 14, no. 11, pp. 2531–2560, 2002.

[50] A. R. Omondi and J. C. Rajapakse, *FPGA implementations of neural networks*. Springer, 2006, vol. 365.

[51] B. Schrauwen, M. D'Haene Maene, D. Verstraeten, and J. Van Campenhout, "Compact hardware liquid state machines on fpga for real-time speech recognition," *Neural Networks*, vol. 21, no. 2, pp. 511–523, 2008.

[52] M. L. Alomar, M. C. Soriano, M. Escalona-Morán, V. Canals, I. Fischer, C. R. Mirasso, and J. L. Rosselló, "Digital implementation of a single dynamical node reservoir computer," *IEEE Transactions on Circuits and Systems II: Express Briefs*, vol. 62, no. 10, pp. 977–981, 2015.

[53] N. D. Haynes, M. C. Soriano, D. P. Rosin, I. Fischer, and D. J. Gauthier, "Reservoir computing with a single time-delay autonomous boolean node," *Physical Review E*, vol. 91, no. 2, p. 020 801, 2015.

[54] B. J. Shastri, M. A. Nahmias, A. N. Tait, A. W. Rodriguez, B. Wu, and P. R. Prucnal, "Spike processing with a graphene excitable laser," *Scientific reports*, vol. 6, 2016.

[55] K. Caluwaerts, M. D'Haene, D. Verstraeten, and B. Schrauwen, "Locomotion without a brain: Physical reservoir computing in tensegrity structures," *Artificial life*, vol. 19, no. 1, pp. 35–66, 2013.

[56] L. Appeltant, M. C. Soriano, G. Van der Sande, J. Danckaert, S. Massar, J. Dambre, B. Schrauwen, C. R. Mirasso, and I. Fischer, "Information processing using a single dynamical node as complex system," *Nature communications*, vol. 2, p. 468, 2011.

[57] L. Larger, M. C. Soriano, D. Brunner, L. Appeltant, J. M. Gutiérrez, L. Pesquera, C. R. Mirasso, and I. Fischer, "Photonic information processing beyond turing: An optoelectronic implementation of reservoir computing," *Optics express*, vol. 20, no. 3, pp. 3241–3249, 2012.

[58] Y. Paquot, F. Duport, A. Smerieri, J. Dambre, B. Schrauwen, M. Haelterman, and S. Massar, "Optoelectronic reservoir computing," *Scientific reports*, vol. 2, 2012.

[59] S Ortín, M. C. Soriano, L. Pesquera, D. Brunner, D San-Martín, I. Fischer, C. R. Mirasso, and J. M. Gutiérrez, "A unified framework for reservoir computing and extreme learning machines based on a single time-delayed neuron," *Scientific reports*, vol. 5, 2015.

[60] F. Duport, B. Schneider, A. Smerieri, M. Haelterman, and S. Massar, "All-optical reservoir computing," *Optics express*, vol. 20, no. 20, pp. 22 783–22 795, 2012.

[61] F. Duport, A. Smerieri, A. Akrout, M. Haelterman, and S. Massar, "Fully analogue photonic reservoir computer," *Scientific reports*, vol. 6, p. 22 381, 2016.

[62] R. M. Nguimdo, G. Verschaffelt, J. Danckaert, and G. Van der Sande, "Simultaneous computation of two independent tasks using reservoir computing based on a single photonic nonlinear node with optical feedback," *IEEE transactions on neural networks and learning systems*, vol. 26, no. 12, pp. 3301–3307, 2015.

[63] P. Antonik, F. Duport, M. Hermans, A. Smerieri, M. Haelterman, and S. Massar, "Online training of an opto-electronic reservoir computer applied to real-time channel equalization.," *IEEE transactions on neural networks and learning systems*, 2016.

[64] M. Hermans, M. C. Soriano, J. Dambre, P. Bienstman, and I. Fischer, "Photonic delay systems as machine learning implementations.," *Journal of Machine Learning Research*, vol. 16, pp. 2081–2097, 2015.

[65] L. Grigoryeva, J. Henriques, L. Larger, and J.-P. Ortega, "Optimal nonlinear information processing capacity in delay-based reservoir computers," *Scientific reports*, vol. 5, 2015.

[66] J. Bueno, D. Brunner, M. C. Soriano, and I. Fischer, "Conditions for reservoir computing performance using semiconductor lasers with delayed optical feedback," *Optics Express*, vol. 25, no. 3, pp. 2401–2412, 2017.

[67] A. Rodan and P. Tiňo, "Minimum complexity echo state network," *Neural Networks, IEEE Transactions on*, vol. 22, no. 1, pp. 131–144, 2011.

[68] R. Legenstein and W. Maass, "Edge of chaos and prediction of computational performance for neural circuit models," *Neural Networks*, vol. 20, no. 3, pp. 323–334, 2007.

[69] T. Instruments, "Ti 46-word speaker-dependent isolated word corpus (cd-rom)," *Gaithersburg: NIST*, 1991.

[70] R. F. Lyon, "A computational model of filtering, detection, and compression in the cochlea," in *Acoustics, Speech, and Signal Processing, IEEE International Conference on ICASSP'82.*, IEEE, vol. 7, 1982, pp. 1282–1285.

[71] D. Verstraeten, B. Schrauwen, M. d?Haene, and D. Stroobandt, "An experimental unification of reservoir computing methods," *Neural Networks*, vol. 20, no. 3, pp. 391–403, 2007.

[72] L. Büsing, B. Schrauwen, and R. Legenstein, "Connectivity, dynamics, and memory in reservoir computing with binary and analog neurons," *Neural computation*, vol. 22, no. 5, pp. 1272–1311, 2010.

[73] K. Hicke, M. A. Escalona-Morán, D. Brunner, M. C. Soriano, I. Fischer, and C. R. Mirasso, "Information processing using transient dynamics of semiconductor lasers subject to delayed feedback," *IEEE Journal of Selected Topics in Quantum Electronics*, vol. 19, no. 4, pp. 1 501 610–1 501 610, 2013.

[74] L. Larger, A. Baylón-Fuentes, R. Martinenghi, V. S. Udaltsov, Y. K. Chembo, and M. Jacquot, "High-speed photonic reservoir computing using a time-delay-based architecture: Million words per second classification," *Physical Review X*, vol. 7, no. 1, p. 011 015, 2017.

[75] J. Nakayama, K. Kanno, and A. Uchida, "Laser dynamical reservoir computing with consistency: An approach of a chaos mask signal," *Optics express*, vol. 24, no. 8, pp. 8679–8692, 2016.

[76] Z. F. Mainen and T. J. Sejnowski, "Reliability of spike timing in neocortical neurons," *Science*, vol. 268, no. 5216, p. 1503, 1995.

[77] X. S. Yao and L. Maleki, "High frequency optical subcarrier generator," *Electronics Letters*, vol. 30, no. 18, pp. 1525–1526, 1994.

[78] ——, "Optoelectronic microwave oscillator," *JOSA B*, vol. 13, no. 8, pp. 1725–1735, 1996.

[79] L. Maleki, "Sources: The optoelectronic oscillator," *Nature Photonics*, vol. 5, no. 12, p. 728, 2011.

[80] P. Devgan, "A review of optoelectronic oscillators for high speed signal processing applications," *ISRN Electronics*, vol. 2013, 2013.

[81] X. Zou, X. Liu, W. Li, P. Li, W. Pan, L. Yan, and L. Shao, "Optoelectronic oscillators (oeos) to sensing, measurement, and detection," *IEEE Journal of Quantum Electronics*, vol. 52, no. 1, pp. 1–16, 2016.

[82] M. Zanola, M. J. Strain, G. Giuliani, and M. Sorel, "Monolithically integrated dfb lasers for tunable and narrow linewidth millimeter-wave generation," *IEEE Journal of Selected Topics in Quantum Electronics*, vol. 19, no. 4, pp. 1 500 406–1 500 406, 2013.

[83] Y.-N. Tan, L. Jin, L. Cheng, Z. Quan, M. Li, and B.-O. Guan, "Multi-octave tunable rf signal generation based on a dual-polarization fiber grating laser," *Optics express*, vol. 20, no. 7, pp. 6961–6967, 2012.

[84] G. Carpintero, E. Rouvalis, K. Ławniczuk, M. Fice, C. C. Renaud, X. J. Leijtens, E. A. Bente, M. Chitoui, F. Van Dijk, and A. J. Seeds, "95 ghz millimeter wave signal generation using an arrayed waveguide grating dual wavelength semiconductor laser," *Optics letters*, vol. 37, no. 17, pp. 3657–3659, 2012.

[85] M. A. Al-Mumin and G. Li, "Self-consistent simulation of self-pulsating two-section gain-coupled dfb lasers," *IEEE journal of quantum electronics*, vol. 41, no. 4, pp. 525–531, 2005.

[86] S. Pan, Z. Tang, D. Zhu, D. Ben, and J. Yao, "Injection-locked fiber laser for tunable millimeter-wave generation," *Optics letters*, vol. 36, no. 24, pp. 4722–4724, 2011.

[87] B. Romeira, J. Javaloyes, J. M. Figueiredo, C. N. Ironside, H. I. Cantú, and A. E. Kelly, "Delayed feedback dynamics of lienard-type resonant tunneling-photo-detector optoelectronic oscillators," *IEEE Journal of Quantum Electronics*, vol. 49, no. 1, pp. 31–42, 2013.

[88] Z. Tang, S. Pan, D. Zhu, R. Guo, Y. Zhao, M. Pan, D. Ben, and J. Yao, "Tunable optoelectronic oscillator based on a polarization modulator and a chirped fbg," *IEEE Photon. Technol. Lett.*, vol. 24, pp. 1487–1489, 2012.

[89] F. Jiang, J. H. Wong, H. Q. Lam, J. Zhou, S. Aditya, P. H. Lim, K. E. K. Lee, P. P. Shum, and X. Zhang, "An optically tunable wideband optoelectronic oscillator based on a bandpass microwave photonic filter.," *Opt. Express*, vol. 21, pp. 16 381–9, 2013.

[90] Z. Wei, R. Wang, T. Pu, G. Sun, T. Fang, and J. Zheng, "A tunable optoelectronic oscillator based on a tunable microwave attenuator," *Opt. Fiber Technol.*, vol. 19, pp. 383–386, 2013.

[91] B. Gao, F. Zhang, P. Zhou, and S. Pan, "A Frequency-tunable Two-tone RF Signal Generator by Polarization Multiplexed Optoelectronic Oscillator," *IEEE Microw. Wireless Comp. Lett.*, vol. 27, pp. 192–194, 2017.

[92] T. B. Simpson, J.-M. Liu, M. AlMulla, N. G. Usechak, and V. Kovanis, "Linewidth sharpening via polarization-rotated feedback in optically injected semiconductor laser oscillators," *IEEE Journal of Selected Topics in Quantum Electronics*, vol. 19, no. 4, pp. 1 500 807–1 500 807, 2013.

[93] A. Hurtado, R. Raghunathan, I. D. Henning, M. J. Adams, and L. F. Lester, "Simultaneous microwave-and millimeter-wave signal generation with a 1310-nm quantum-dot-distributed feedback laser," *IEEE Journal of Selected Topics in Quantum Electronics*, vol. 21, no. 6, pp. 568–574, 2015.

[94] P. Pérez, A. Quirce, A. Valle, A. Consoli, I. Noriega, L. Pesquera, and I. Esquivias, "Photonic generation of microwave signals using a single-mode vcsel subject to dual-beam orthogonal optical injection," *IEEE Photonics Journal*, vol. 7, no. 1, pp. 1–14, 2015.

[95] M. C. Pochet, N. A. Naderi, V. Kovanis, and L. F. Lester, "Modeling the dynamic response of an optically-injected nanostructure diode laser," *IEEE Journal of Quantum Electronics*, vol. 47, no. 6, pp. 827–833, 2011.

[96] Y.-H. Liao and F.-Y. Lin, "Dynamical characteristics and their applications of semiconductor lasers subject to both optical injection and optical feedback," *Optics express*, vol. 21, no. 20, pp. 23 568–23 578, 2013.

[97] Y.-H. Hung and S.-K. Hwang, "Photonic microwave stabilization for period-one nonlinear dynamics of semiconductor lasers using optical modulation sideband injection locking," *Optics express*, vol. 23, no. 5, pp. 6520–6532, 2015.

[98] J. S. Suelzer, T. B. Simpson, P. Devgan, and N. G. Usechak, "Tunable, low-phase-noise microwave signals from an optically injected semiconductor laser with optoelectronic feedback," *Optics letters*, vol. 42, no. 16, pp. 3181–3184, 2017.

[99] S.-C. Chan, S.-K. Hwang, and J.-M. Liu, "Period-one oscillation for photonic microwave transmission using an optically injected semiconductor laser," *Optics Express*, vol. 15, no. 22, pp. 14 921–14 935, 2007.

[100] C. Cui, X. Fu, and S.-C. Chan, "Double-locked semiconductor laser for radio-over-fiber uplink transmission," *Optics letters*, vol. 34, no. 24, pp. 3821–3823, 2009.

[101] M. J. Wishon, A. Locquet, C. Chang, D Choi, and D. Citrin, "Crisis route to chaos in semiconductor lasers subjected to external optical feedback," *Physical Review A*, vol. 97, no. 3, p. 033 849, 2018.

[102] I Reidler, Y. Aviad, M Rosenbluh, and I. Kanter, "Ultrahigh-speed random number generation based on a chaotic semiconductor laser," *Phys. Rev. Lett.*, vol. 103, no. 2, p. 024 102, 2009.

[103] I. Kanter, Y. Aviad, I. Reidler, E. Cohen, and M. Rosenbluh, "An optical ultrafast random bit generator," *Nat. Photonics*, vol. 4, no. 1, pp. 58–61, 2010.

[104] J. Zhang, Y. Wang, M. Liu, L. Xue, P. Li, A. Wang, and M. Zhang, "A robust random number generator based on differential comparison of chaotic laser signals," *Opt. Express*, vol. 20, no. 7, pp. 7496–7506, 2012.

[105] N. Li, B. Kim, V. Chizhevsky, A Locquet, M Bloch, D.S. Citrin, and W. Pan, "Two approaches for ultrafast random bit generation based on the chaotic dynamics of a semiconductor laser," *Opt Express*, vol. 22, no. 6, pp. 6634–6646, 2014.

[106] K. Hirano, T. Yamazaki, S. Morikatsu, H. Okumura, H. Aida, A. Uchida, S. Yoshimori, K. Yoshimura, T. Harayama, and P. Davis, "Fast random bit generation with bandwidth-enhanced chaos in semiconductor lasers," *Opt. Express*, vol. 18, no. 6, pp. 5512–5524, 2010.

[107] A. Argyris, S. Deligiannidis, E. Pikasis, A. Bogris, and D. Syvridis, "Implementation of 140 gb/s true random bit generator based on a chaotic photonic integrated circuit," *Opt. Express*, vol. 18, no. 18, pp. 18 763–18 768, 2010.

[108] R. M. Nguimdo, G. Verschaffelt, J. Danckaert, X. Leijtens, J. Bolk, and G. Van der Sande, "Fast random bits generation based on a single chaotic semiconductor ring laser," *Opt. Express*, vol. 20, no. 27, pp. 28 603–28 613, 2012.

[109] T Butler, C Durkan, D Goulding, S Slepneva, B Kelleher, S. Hegarty, and G Huyet, "Optical ultrafast random number generation at 1 tb/s using a turbulent semiconductor ring cavity laser," *Opt. Lett.*, vol. 41, no. 2, pp. 388–391, 2016.

[110] X.-Z. Li and S.-C. Chan, "Heterodyne random bit generation using an optically injected semiconductor laser in chaos," *IEEE J. Quantum. Electron.*, vol. 49, no. 10, pp. 829–838, 2013.

[111] P. Li, Y. Sun, X. Liu, X. Yi, J. Zhang, X. Guo, Y. Guo, and Y. Wang, "Fully photonics-based physical random bit generator," *Opt. Lett.*, vol. 41, no. 14, pp. 3347–3350, 2016.

[112] M. Virte, E. Mercier, H. Thienpont, K. Panajotov, and M. Sciamanna, "Physical random bit generation from chaotic solitary laser diode," *Opt. Express*, vol. 22, no. 14, pp. 17 271–17 280, 2014.

[113] N. Oliver, M. C. Soriano, D. W. Sukow, and I. Fischer, "Fast random bit generation using a chaotic laser: Approaching the information theoretic limit," *IEEE J. Quantum. Electron.*, vol. 49, no. 11, pp. 910–918, 2013.

[114] G. Verschaffelt, M. Khoder, and G. Van der Sande, "Random number generator based on an integrated laser with on-chip optical feedback," *Chaos: An Interdisciplinary Journal of Nonlinear Science*, vol. 27, no. 11, p. 114 310, 2017.

[115] Y. Akizawa, T. Yamazaki, A. Uchida, T. Harayama, S. Sunada, K. Arai, K. Yoshimura, and P. Davis, "Fast random number generation with bandwidth-enhanced chaotic semiconductor lasers at 8 x 50 gb/s," *IEEE Photonics Technol. Lett.*, vol. 24, no. 12, pp. 1042–1044, 2012.

[116] J. Wu, X Tang, Z. Wu, G. Xia, and G. Feng, "Parallel generation of 10 gbits/s physical random number streams using chaotic semiconductor lasers," *Laser Phys.*, pp. 1–5, 2012.

[117] A. Wang, P. Li, J. Zhang, J. Zhang, L. Li, and Y. Wang, "4.5 gbps high-speed real-time physical random bit generator," *Opt. Express*, vol. 21, no. 17, pp. 20 452–20 462, 2013.

[118] K. Ugajin, Y. Terashima, K. Iwakawa, A. Uchida, T. Harayama, K. Yoshimura, and M. Inubushi, "Real-time fast physical random number generator with a photonic integrated circuit," *Opt. Express*, vol. 25, no. 6, pp. 6511–6523, 2017.

[119] A. Wang, L. Wang, P. Li, and Y. Wang, "Minimal-post-processing 320-gbps true random bit generation using physical white chaos," *Opt. Express*, vol. 25, no. 4, pp. 3153–3164, 2017.

[120] A. Sahai, B Kim, D Choi, A Locquet, and D. Citrin, "Mapping the nonlinear dynamics of a laser diode via its terminal voltage," *Opt. Lett.*, vol. 39, no. 19, pp. 5630–5633, 2014.

[121] A. Rukhin, J. Soto, J. Nechvatal, M. Smid, and E. Barker, Booz-Allen and Hamilton Inc Mclean Va, Tech. Rep., 2001.

[122] A. Uchida, "Random number generation with chaotic lasers," *Optical Communication with Chaotic Lasers: Applications of Nonlinear Dynamics and Synchronization*, pp. 445–509,

[123] N. Li, B. Kim, A Locquet, D. Choi, W. Pan, and D. Citrin, "Statistics of the optical intensity of a chaotic external-cavity dfb laser," *Opt. Lett.*, vol. 39, no. 20, pp. 5949–5952, 2014.

[124] D. Rontani, A. Locquet, M. Sciamanna, and D. Citrin, "Loss of time-delay signature in the chaotic output of a semiconductor laser with optical feedback," *Opt. Lett.*, vol. 32, no. 20, pp. 2960–2962, 2007.

[125] F.-Y. Lin and J.-M. Liu, "Chaotic lidar," *IEEE journal of selected topics in quantum electronics*, vol. 10, no. 5, pp. 991–997, 2004.

[126] J. D. Hart, Y. Terashima, A. Uchida, G. B. Baumgartner, T. E. Murphy, and R. Roy, "Recommendations and illustrations for the evaluation of photonic random number generators," *APL Photonics*, vol. 2, no. 9, p. 090 901, 2017.

[127] X.-Z. Li, J.-P. Zhuang, S.-S. Li, J.-B. Gao, and S.-C. Chan, "Randomness evaluation for an optically injected chaotic semiconductor laser by attractor reconstruction," *Physical Review E*, vol. 94, no. 4, p. 042 214, 2016.

[128] L. Zunino, O. A. Rosso, and M. C. Soriano, "Characterizing the hyperchaotic dynamics of a semiconductor laser subject to optical feedback via permutation entropy," *IEEE J. Sel. Topics in Quantum Electron.*, vol. 17, no. 5, pp. 1250–1257, 2011.

[129] J. Toomey and D. Kane, "Mapping the dynamic complexity of a semiconductor laser with optical feedback using permutation entropy," *Opt. Express*, vol. 22, no. 2, pp. 1713–1725, 2014.

[130] N. Li, L. Zunino, A. Locquet, B. Kim, D. Choi, W. Pan, and D. S. Citrin, "Multiscale ordinal symbolic analysis of the lang-kobayashi model for external-cavity semiconductor lasers: A test of theory," *IEEE J. Quantum. Electron.*, vol. 51, no. 8, pp. 1–6, 2015.

[131] C. Bandt and B. Pompe, "Permutation entropy: A natural complexity measure for time series," *Phys. Rev. Lett.*, vol. 88, no. 17, p. 174 102, 2002.

[132] M. Rudd, "A laser doppler velocimeter employing the laser as a mixer-oscillator," *Journal of Physics E: Scientific Instruments*, vol. 1, no. 7, p. 723, 1968.

[133] S. Donati, G. Giuliani, and S. Merlo, "Laser diode feedback interferometer for measurement of displacements without ambiguity," *IEEE Journal of Quantum Electronics*, vol. 31, no. 1, pp. 113–119, 1995.

[134] T. Morikawa, Y Mitsuhashi, J Shimada, and Y Kojima, "Return-beam-induced oscillations in self-coupled semiconductor lasers," *Electronics Letters*, vol. 12, no. 17, pp. 435–436, 1976.

[135] Y Mitsuhashi, T Morikawa, K Sakurai, A Seko, and J Shimada, "Self-coupled optical pickup," *Optics Communications*, vol. 17, no. 1, pp. 95–97, 1976.

[136] A Seko, Y Mitsuhashi, T Morikawa, J Shimada, and K Sakurai, "Self-quenching in semiconductor lasers and its applications in optical memory readout," *Applied Physics Letters*, vol. 27, no. 3, pp. 140–141, 1975.

[137] H. Ukita, Y. Uenishi, and Y. Katagiri, "Applications of an extremely short strong-feedback configuration of an external-cavity laser diode system fabricated with gaas-based integration technology," *Applied optics*, vol. 33, no. 24, pp. 5557–5563, 1994.

[138] D. Heinis, C. Gorecki, S. Bargiel, and B. Cretin, "Feedback-induced voltage change of avertical-cavity surface-emitting laser as an active detection system for miniature optical scanning probe microscopes," *Optics Express*, vol. 14, no. 8, pp. 3396–3405, 2006.

[139] K. T. Grattan and B. T. Meggitt, *Optical fiber sensor technology*. Springer, 1995, vol. 1.

[140] F. Rogister, A. Locquet, D. Pieroux, M. Sciamanna, O. Deparis, P. Mégret, and M. Blondel, "Secure communication scheme using chaotic laser diodes subject to incoherent optical feedback and incoherent optical injection," *Optics Letters*, vol. 26, no. 19, pp. 1486–1488, 2001.

[141] C. Chang, D. Choi, A Locquet, M. J. Wishon, K Merghem, A. Ramdane, F. Lelarge, A Martinez, and D.S. Citrin, "A multi-ghz chaotic optoelectronic oscillator based on laser terminal voltage," *Appl. Phys. Lett.*, vol. 108, no. 19, p. 191 109, 2016.

[142] M. J. Wishon, G Mourozeau, K Ng, A. Sahai, A. Locquet, and D. Citrin, "Reading a cd-rom without a photodiode," in *Semiconductor Lasers and Laser Dynamics VII*, International Society for Optics and Photonics, vol. 9892, 2016, 98921Z.

[143] *Data interchange on read-only 120 mm optical data disks (cd-rom),(european computer manufacturers association, 1996)*.

[144] S. G. Stan, *The CD-ROM drive: A brief system description*. Springer Science & Business Media, 2013.